Development and Validation of a New Eddy Dissipation Concept (EDC) Model for MILD Combustion

Hesheng Bao

TUDelft
Delft
University of
Technology

Challenge the future

DEVELOPMENT AND VALIDATION OF A NEW EDDY DISSIPATION CONCEPT (EDC) MODEL FOR MILD COMBUSTION

by

Hesheng Bao

in partial fulfillment of the requirements for the degree of

Master of Science

in Mechanical Engineering

at the Delft University of Technology,
to be defended publicly on Monday January 23, 2017 at 13:30 AM.

Supervisor:	Prof. Dr. D.J.E.M. Roekaerts
	M.Sc. X. Huang
Thesis committee:	Dr. Ir. M. J. Tummers
	Dr. D. J. P. Lahaye

An electronic version of this thesis is available at http://repository.tudelft.nl/.

TUDelft
Delft
University of
Technology

ABSTRACT

Moderate and Intense Low-oxygen Dilution (MILD) combustion is established to achieve high thermal efficiency and low pollutant emissions, including both NO_x and soot. The Eddy Dissipation Concept (EDC) is the most widely used combustion model in the existing numerical studies of turbulent MILD combustion. It is easy to implement and has acceptable computational cost. EDC is a turbulence–chemistry coupling model which assumes that the reaction zone can be modelled as a well-stirred chemical reactor, exchanging mass with the environment at a rate determined by turbulence. However, the low Damköhler number found within the homogeneous reaction zone brings a challenge. The standard EDC model is found to predict too early ignition. A simple solution is to modify the model constant parameters C_τ and C_γ to a different value using the experimental data, which is not effective since the method is case dependent. Recently, Parente et al. proposed an extension of EDC model which qualitatively calculates the model constants locally, depending on the local turbulent Reynolds number and Damköhler number. The new extended EDC model used in this work is a further development of Parente et al.'s model. We improved the model by assuming the chemical time scale is the time needed to traverse the fine structures ($\tau_c^* = L^*/S_L$) for both C_τ and C_γ. In this way, the model is able to quantitatively define C_τ and C_γ locally without any tuning. Besides, C_γ is found to be proportional to $Da^{*3/4}$ rather than $Da^{*1/2}$ in Parente's model. The new model is validated through the Delft-jet-in-hot-coflow (DJHC) burner database and further applied in a laboratory-scale MILD furnace in order to give theoretical insight. For the DJHC burner case, the RSM turbulence model is proved to give better agreement compared to the widely used modified standard $k-\epsilon$ model. The new extended EDC model is validated in terms of temperature, flow, and OH-concentration-based liftoff height. The temperature peak is captured better. A study of influencing factors, including the jet velocity, fuel temperature, and temperature and oxygen concentration of coflow, is undertaken. The influences of these issues on flame volume, liftoff height and peak temperatures are analysed. For the furnace case, the prediction of the new extended EDC model is compared with the EDC model with modified constant parameters. The new model can provide a comparable prediction compared to the widely used model. The analyse of NO_x shows the maximum NO concentration is lower than approximately 10 ppmv in the furnace. The thermal NO_x formation process is not dominant in the furnace studied.

ACKNOWLEDGEMENT

"Too young, too simple, sometimes naive."

— *Zemin Jiang*

CONTENTS

LIST OF FIGURES

LIST OF TABLES

NOMENCLATURE

English notations:

Symbol	Units	Description
a	[m/s]	speed of sound
$a_{p,k}$	[1/(m·Pa)]	Planck mean absorption coefficient of species k
A_{fj}	[1/s]	pre-exponential constant
C	[-]	constant
C_{pk}	[(J/kg·K)]	specific heat of species k
C_γ	[-]	volume fraction (fine structure) EDC model constant
C_μ	[-]	model constant for turbulent viscosity
C_τ	[-]	residence time EDC model constant
D	[m^2/s]	the diffusion coefficient between any two species
D_k	[m^2/s]	the diffusion coefficient of species k into the rest of the mixture
$D_{j,k}$	[m^2/s]	the binary diffusion constant
D_{st}	[m^2/s]	turbulent thermal diffusivity
D_{th}	[m^2/s]	laminar thermal diffusivity
Da	[-]	Damköhler number
Da_k	[-]	Damköhler number of Kolmogorov scale
Dtr	[-]	the ratio of laminar diffusion over turbulent diffusion
E_{aj}	[cal/(mol·K)]	activation energy
f	[-]	any property at sufficiently high Reynolds number
h_k	[J/kg]	total enthalpy of species k
$h^o_{f,k}$	[J/kg]	chemical enthalpy of species k at reference temperature
h_{sk}	[J/kg]	sensible enthalpy of species k
k	[m^2/s^2]	turbulence kinetic energy
K_{fj}	[-]	rate constant
L	[m]	turbulent length scale
Le_k	[-]	Lewis number of species k
$\dot{m}^*$	[kg/(m^3·s)]	the mass exchange rate with unit 1/s and the surroundings
M_{ij}	[kg/(m·s^3)]	production by system rotation
M_k	[kg/mol]	molecular weights of species k
$\mathbf{M}_k$	[-]	species k in a chemical reaction
M_t	[-]	turbulent Mach number
p	[Pa]	static pressure

P_{ij}	[kg/(m·s^3)]	shear stress generation
P_k	[kg/(m·s^3)]	the generation of turbulence kinetic energy
$\dot{Q}$	[J/(m^3·s)]	heat source term
Pr_{st}	[-]	turbulent Prandtl number
q	[J/(kg·s)]	heat generated at a cascade level
$\mathscr{Q}_j$	[mol/(m^3·s)]	rate of progress of reaction j
R	[J/(K·mol)]	universal gas constant
	[cal/(K·mol)]	
R_{CO}	[-]	the local CO molar fraction divided by the maximum value over the whole computation domain
R_{ij}	[kg/(m·s^2)]	turbulent Reynolds stresses
Re	[-]	Reynolds number
Re_T	[-]	turbulent Reynolds number
S_H	[J/(m^3·s)]	source term in enthalpy equation
S_{ij}	[1/s]	strain tensor
$S_{M,i}$	[kg/(m^2·s^2)]	volumetric source term in momentum equation
S_L	[m/s]	laminar flame speed
S_T	[m/s]	turbulent flame speed
Sc_{kt}	[-]	turbulent Schmidt number for species k
T	[K]	temperature
u	[m/s]	turbulent velocity scale
u_i	[m/s]	fluid velocity component
$V_{k,i}$	[m/s]	i-component of the diffusion velocity for species k
w	[m^2/s^3]	strain rate at a cascade level
X_j	[-]	mole fraction
Y_k	[-]	mass fraction of species k

Greek notations:

Symbol	Units	Description
α	[-]	inverse Prandtl number
γ^*	[-]	the volume fraction occupied by fine structures
γ_λ	[-]	the fine structure volume fraction (ratio by length)
δ_{ij}	[-]	Kronecker symbol
ϵ	[J/(kg·s)]	turbulence dissipation rate
μ	[Pa·s]	dynamic viscosity
μ_{eff}	[Pa·s]	effective dynamic viscosity in RNG k-ϵ model
μ_t	[Pa·s]	turbulent dynamic viscosity
ν	[m^2/s]	kinematic viscosity
ν_{kj}	[-]	molar stoichiometric coefficients of species k in reaction j
ν_T	[m^2/s]	turbulent kinematic viscosity
ρ	[kg/m^3]	density (refers to gas only)
σ	[W/(m^2·K^4)]	Stefan-Boltzmann constant

σ_k	[-]	turbulent Prandtl number for turbulence kinetic energy
σ_ϵ	[-]	turbulent Prandtl number for turbulence dissipation rate
τ_c	[s]	chemical time scale
τ_c^*	[s]	chemical time scale of fine structures
τ_{ij}	[kg/(m·s^2)]	viscous stress tensor
τ^*	[s]	the residence time of reactants inside fine structures
ϕ	[J/(m^3·s)]	viscous dissipation term in energy equation
χ	[-]	the fraction of the active fine structures
ω	[1/s]	eddy frequency at a cascade level
ω_{ij}	[1/s]	rotation tensor
$\bar{\omega}_i$	[kg/(m^3·s)]	mean chemical reaction rate calculated by EDC model
$\dot{\omega}_k$	[kg/(m^3·s)]	chemical reaction rate for species k
$\dot{\omega}_T$	[J/(m^3·s)]	combustion caused heat release rate

Subscripts:

Symbol	Description
$D1$	EDC model constant
$D2$	EDC model constant
i	i-th component
j	j-th component
k	species k
m	m-th component
max	maximum value of a quantity
n	n-th cascade level

Superscripts:

Symbol	Description
$*$	fine structures
$-$	Reynolds decomposition mean value
$\sim$	Favre averages mean value
$'$	Reynolds decomposition fluctuation
$''$	Favre averages decomposition fluctuation
$\cdot$	rate of a quantity

Abbreviations:

Symbol	Description
BML	Bray Moss Libby
CARS	Coherent anti-Stokes-Raman spectroscopy
CD	Coalescence Dispersion mixing model

CFD	Computational Fluid Dynamics
CMC	Conditional Momentum Closure
CSE	Conditional Source-term Estimation
DJHC	Delft jet-in hot coflow
DNG	Dutch natural gas
DNS	Direct Numerical Simulations
DO	Discrete Ordinates
EBU	Eddy Break Up
EDC	Eddy Dissipation Concept
EMST	Euclidean Minimum Spanning Tree mixing model
EPBD	Electrically preheated diffusion
FPV	three-stream flamelet/progress variable
IEA	International Energy Agency
IEM	Interaction-by-Exchange-with-the-Mean mixing model
IPCC	Intergovernmental Panel on Climate Change
ISAT	In Situ Adaptive Tabulation
JHC	Jet-in-hot-coflow
LDA	Laser Doppler Anemometry
LES	Large Eddy Simulations
LJHC	Laminar jet-in hot coflow
LPDF	Lagrangian PDF
LPG	liquefied petroleum gas
MILD	Moderate and Intense Low-oxygen Dilution
MEPDF	Multi-environment PDF
NG	natural gas
ppmv	parts per million volume
PDF	Probability Density Function
PFR	Plug Flow Reactor
PLIF	Planar Laser Induced Fluorescence
PPDF	Presumed PDF
PSR	Perfectly Stirred Reactor
SPRF	Stagnation Point Reverse Flow
RANS	Reynolds Averaged Navier Stokes
RSM	Reynolds Stress Model
WSGGM	weighted-sum-of-gray-gases model
WSR	well-stirred-reactor

1

INTRODUCTION

"Energy, which has a bearing on both economic and national security, is of importance and a major constraining factor to the economic and social development of the world."[1] The world's population is predicted to increase to nearly 8.8 billion people by 2035, the increment is over 20% compared to 2014[2], which means more energy is required. According to BP's annually forecast[3], the energy consumption by 2035 increases by 34%. Although alternative energy has been a hot topic, the era of fossil fuels will not end in the foreseeable future. This is due to the technology limitations of unconventional energy and the abundant cheap fossil resources we have[4]. According to the latest outlook released by BP, by 2035, fossil fuels still account for 80% of the world's energy supply. Similarly, OPEC believes that the fossil fuels will need to supply at least three-quarters of the energy mix by 2040[5]. The most optimistic prediction by International Energy Agency (IEA) reported that the share of fossil fuels in the world energy mix can decline to around 75% in 2030 with the help of national pledges[6].

The harm of carbon and nitrogen oxide emissions caused by the conventional combustion of fossil fuels is a well-known issue. According to the research by IPCC[7], scientists are more than 95% certain that global warming is caused by anthropogenic activities, which is likely to have caused a temperature rise of 0.13 ± 0.03 °C per decade during the past 50 years[8]. The increase of temperature not only caused the sea level rise, but also led to more climate extremes. This threatens the food security and thus strongly challenges the survival of mankind. Meanwhile, the noxious emissions also do harm to our living environment. The acid rain is one of the most widely known problems caused by the high temperature during combustion process. The governments have raised great concern about the pollutants issue. The Paris Agreement[9] is a milestone to strengthen the global response through "nationally determined contributions". Both the developed and developing coun-

tries pay efforts. EU promised to reduce emissions by at least 40% by 2030 on 1990 levels, the US aimed to cut by 28% compared with 2005, while China ratified to reach its peak of carbon emissions before 2030 by reducing the emission 60-65% per unit of GDP.

As fossil fuels can not be phased out overnight, an essential part of the solution is to use the energy more efficiently and lower the emissions, such as replacing coal with gas and developing new combustion technologies.

1.1. MILD COMBUSTION

MILD combustion, which is short for "Moderate and Intense Low-oxygen Dilution", is an exciting innovation that realizes both low carbon and nitrogen emissions while the energy efficiency is increased. This combustion technique was first proposed by Wünning and Wünning[10] or Katsuki and Hasegawa [11] in the end of 1990s. They found that NO_x emissions could be reduced to ultra low levels by mixing a reactant mixture with hot combustion products. The Japanese researchers Katsuki et al. used "HiTAC (High Temperature Air Combustion)" to describe this new technique, since the process requires that the inlet temperature of reactants is higher than autoignition temperature of the mixture[12]. Differently, the new combustion was named as "Flameless Oxidation (FLOX)" by Wünning because during their experiment the flame was invisible and inaudible[10]. Since then, plenty of investigations have been done, the "flameless" characteristic has been found to be too limited. MILD flame could be either totally flameless or blue. In some rare cases, greenish flame could also be observed[13]. Recently, the luminosity of MILD combustion has been a much studied topic, the changing from yellow to blue, green, and bluish green has been investigated empirically by many researchers[14–16]. According to Cavaliere and de Joannon[17], the term "MILD" may be a better choice. It can show the contrast characteristic of this new technique with all the other combustion processes (a wider temperature range) and the term also describes one of the most typical conditions for which the process can be achieved. In this thesis, MILD combustion is adopted.

Different definitions have been proposed to identify the MILD condition. Wünning[10] defined a recirculation rate K_v (the ratio between the mass flow rate of recirculated exhaust gases over the total mass flow) and found that MILD combustion is only stable when $K_v > 3$ and the furnace temperature is larger than 800 °C for his methane combustion case. The condition can be different according to the fuel used. Kumar et al.[18] quantitatively used the temperature variation to define the MILD combustion. They pointed out that the combustion process should have a normalized spatial temperature variation of around 15%. Milani[19] defined MILD as a combustion mode in which the flame front is suppressed and the NO_x and CO emission are abated to very small residual values. According to Cavaliere and de Joannon[17], a process is named "MILD" when the inlet temperature of the

oxidizer is higher than the self-ignition temperature of the reactants mixture while the maximum temperature increase with respect to the inlet is lower than the mixture self-ignition temperature.

Due to the distinct benefits of MILD combustion, so far, it has been attempted to apply it in steel industry, ceramic industry, glass industry, combined heat and power and power generation[20].

1.2. OBJECTIVES

This thesis aims to develop and validate efficient and accurate models for MILD combustion through the Computational Fluid Dynamics (CFD) approach. The combustion simulation is based on an Eddy Dissipation Concept (EDC) model, as it has relatively good accuracy at acceptable computational cost compared to other models. However, Cabra[21] found that EDC model shows a trend of under-prediction of the liftoff height. Generally, it is a common agreement that EDC model tends to over-predict the temperature, the reasons are explained in detail in the following chapters. The more specific objective of this work is to improve the EDC model for MILD combustion cases.

1.3. STRUCTURE

Chapter 2 presents the relevant theory of this thesis and introduces the new extended EDC model.

Chapter 3 presents a study of a MILD burner. The extended EDC model is validated, different turbulence models are compared. The influencing factors are studied through the new model.

Chapter 4 presents simulation of an ongoing experiment of a MILD furnace to which the new extended EDC model is applied.

Chapter 5 summarizes the conclusions and gives recommendations for future work.

2

THEORY OF TURBULENT COMBUSTION

In this chapter, some theories relevant to this research are presented. Generally, the simulation of turbulent combustion through Computational Fluid Dynamics (CFD) is undertaken by three approaches:

1. Reynolds Averaged Navier Stokes (RANS) is the first possible CFD method which solves the mean values of all quantities. It needs averaged balance equations to calculate averaged quantities. The averaged equations require closure rules, both turbulence model and turbulent combustion model are needed to describe flow dynamics, species conversion and heat release.

2. Large Eddy Simulations (LES). Only large turbulent scales are explicitly calculated while the smaller ones are modelled through subgrid closure rules. The balance equations are gained by filtering the instantaneous balance equations, but the closure of terms that describe the subgrid scale effects is needed. The LES method is always transient 3-dimensional simulation and requires finer grids compared to RANS, which enlarges the computational cost.

3. Direct Numerical Simulations (DNS) is the most accurate but most expensive method which solves the full instantaneous Navier-Stokes equations directly without any extra model for turbulence, all turbulence scales are explicitly described.

In a word, DNS could only be done in 3-D and the grid should be very precise which depends on necessity to resolve Kolmogorov scale and flame thickness. DNS is thus the most computational demanding method and is limited to relatively low Reynolds numbers and simple geometries. LES could use coarser grids compared to LES but also needs to be done

in 3-D, the method is also computational costly because at least 80 % of the turbulence kinetic energy are computed directly, while the subgrids are needed and influence the computational time and accuracy a lot. Both DNS and LES method were developed due to the improvement of high performance computers. RANS is more widely used due to the possibility of being applied into 2-D cases and the grid could be more coarse which only depends on gradient of mean quantities, but the accuracy is limited by the closure models[22]. RANS is chosen in this thesis.

2.1. GOVERNING EQUATIONS

The conservation equations used for reacting flows are different from the usual non-reacting Navier-Stokes equations. More equations are required due to mixture compositions and chemical reactions. The theory used here is mainly from Refs.[23–25]. Mass, momentum, species and energy balance should be taken into account, and also thermodynamic equation of state.

2.1.1. MASS CONSERVATION

The conservation of mass law applied to a fluid passing through an fixed infinitesimal control volume, it is also called continuity equation, which is shown below:

$$\frac{\partial \rho}{\partial t} + \frac{\partial \rho u_i}{\partial x_i} = 0 \tag{2.1}$$

where ρ denotes the fluid density, which refers to only gas in this thesis, based on ideal gas law (Eq. (2.2)) and u_i is the fluid velocity component (i=1 to 3).

$$\rho = \frac{p}{RT \sum_{i=1}^{N} (Y_k / M_k)} \tag{2.2}$$

where p refers to static pressure while Y_k and M_k represent mass fraction and molecular weights of species k in a N-species mixture, respectively. The universal gas constant $R = 8.314 J/(K \cdot mol)$ and T is temperature.

2.1.2. MOMENTUM CONSERVATION

Momentum conservation, also well known as Navier-Stokes equation, is the govering equation of the viscous fluid substances' motion. The conservation is derived by applying Newton's Second Law to a fluid passing through an infinitesimal control volume, thus it describes the changes of the flow momentum in space and time. In order to express momentum conservation ((Eq. 2.4)), the viscous stress tensor should be modified. For a Newtonian

fluid, the viscous stress tensor τ_{ij} is defined by:

$$\tau_{ij} = -\frac{2}{3}\mu\frac{\partial u_k}{\partial x_k}\delta_{ij} + \mu(\frac{\partial u_i}{\partial x_j} + \frac{\partial u_j}{\partial x_i}) \tag{2.3}$$

where μ is the dynamic viscosity (kinematic viscosity $\nu = \mu/\rho$), while δ_{ij} is the Kronecker symbol ($\delta_{ij} = 1$ if $i = j$ and 0 elsewise).

$$\frac{\partial \rho u_j}{\partial t} + \frac{\partial}{\partial x_i}(\rho u_i u_j) = -\frac{\partial p}{\partial x_j} + \frac{\partial \tau_{ij}}{\partial x_i} + S_{M,i} \tag{2.4}$$

The left hand side shows the inertial effects. The first term represents the time dependent effects (rate of momentum change per unit volume in control volume), while the second term illustrates the convective effects (momentum variation by convection through the control surface per unit volume in this case). For right hand side, the first two terms show the internal influence (surface forces per unit volume) of the fluid. The last term denotes the volumetric source term, as body force.

2.1.3. SPECIES CONSERVATION

Conservation of mass conservation of a species k, is expressed as:

$$\frac{\partial \rho Y_k}{\partial t} + \frac{\partial}{\partial x_i}[\rho(u_i + V_{k,i})Y_k] = \dot{\omega}_k \tag{2.5}$$

where $V_{k,i}$ is the i-component of the diffusion velocity V_k for species k, and the reaction rate is indicated by $\dot{\omega}_k$. The species transportation can be rewritten in the following way:

$$\frac{\partial \rho Y_k}{\partial t} + \frac{\partial}{\partial x_i}(\rho u_i Y_k) = -\frac{\partial}{\partial x_i}(\rho V_{k,i} Y_k) + \dot{\omega}_k \tag{2.6}$$

In this way, the left hand side also consists of time derivative term and convective term, similar to the momentum transportation equation. The first term of right hand side is thus convection with the molecular diffusion velocity, which is different from the mixture velocity convection that is put in the left hand side.

The molecular diffusion term $V_{k,i} Y_k$ could be approximated by Fick's law under the hypothesis of ignoring the pressure gradients and volume forces, assume all binary diffusion coefficients are equal, thus the diffusion coefficient between any two species is equal to D, the diffusion of species k could be expressed by:

$$V_{k,i} Y_k = -D\frac{\partial Y_k}{\partial x_i} \tag{2.7}$$

A more detailed method, Hirschfelder and Curtiss approximation[26], could also be used for multispecies gas.

$$V_{k,i} Y_k = -D_k \frac{\partial Y_k}{\partial x_i} \tag{2.8}$$

where D_k is a diffusion coefficient of species k into the rest of the mixture:

$$D_k = \frac{1 - Y_k}{\sum_{j \neq k} X_j / D_{jk}} \tag{2.9}$$

where X_j denotes mole fraction and D_{jk} is the binary diffusion constant.

2.1.4. ENERGY CONSERVATION

Both total enthalpy and sensible enthalpy could be applied in the energy conservation. The relation of them is shown below:

$$h_k = \int_{T_0}^{T} C_{pk} dT + \Delta h_{f,k}^o \tag{2.10}$$

where h_k is total enthalpy, the first term on the right hand side is sensible enthalpy (h_{sk}) and the second term $h_{f,k}^o$ is chemical enthalpy, which is the enthalpy of species k at reference temperature T_0, and C_{pk} is the specific heat of the kth species. All quantities are expressed per unit of mass.

Energy conservation is expressed by applying the First Law of thermodynamics to a fluid passing an infinitesimal control volume. The enthalpy used here refers to sensible enthalpy.

$$\frac{\partial \rho h_s}{\partial t} + \frac{\partial}{\partial x_i}(\rho u_i h_s) = \frac{Dp}{Dt} - \frac{\partial q_i}{\partial x_i} + \tau_{ij} \frac{\partial u_i}{\partial x_j} + \dot{\omega}_T + \dot{Q} + S_H \tag{2.11}$$

where the third term on the right hand side $\phi = \tau_{ij} \partial u_i / \partial x_j$ is the viscous dissipation term, the last term is body force. $\dot{Q}$ is the heat source term, such as radiation or laser effect. The energy flux term $\partial q_i / \partial x_i$ includes a heat diffusion term (Fourier's Law) and a species diffusion related enthalpy term, which is in detail:

$$q_i = -\lambda \frac{\partial T}{\partial x_i} + \rho \sum_{k=1}^{N} h_{s,k} Y_k V_{k,i} \tag{2.12}$$

The combustion caused heat release $\dot{\omega}_T$ is related to the chemical enthalpy $\Delta h_{f,k}^o$ and chemical reaction rate ω_k:

$$\dot{\omega}_T = -\sum_{k=1}^{N} \Delta h_{f,k}^o \dot{\omega}_k \tag{2.13}$$

2.2. Reynolds Averaged Navier-Stokes Equations

2.2.1. Reynolds and Favre Averaging

Turbulence can be characterized by fluctuations of all local properties at sufficiently high Reynolds number. Any property f can be split into two parts by Reynolds decomposition:

$$f = \overline{f} + f' \tag{2.14}$$

$\overline{f}$ is the mean value, which is a time average over a long period t in the case of steady flow field, while f' is the fluctuation:

$$\overline{f} = \frac{1}{t}\int_0^t f(t')\,dt' \tag{2.15}$$

The previous description is sufficient for constant density flow, for other cases, a mass-weighted average method (Favre averages[27]) is more widely used:

$$\widetilde{f} = \frac{\int_0^t \rho(t')f(t')\,dt'}{\int_0^t \rho(t')\,dt'} = \frac{\overline{\rho f}}{\overline{\rho}} \tag{2.16}$$

Thus, any variable could be split into mean value and fluctuation through the equation below:

$$f = \widetilde{f} + f'' \tag{2.17}$$

2.2.2. Reynolds Averaged Navier-Stokes Equations

Reynolds Averaged Navier-Stokes (RANS) balance equations are obtained by averaging the instantaneous governing balance equations mentioned before through Favre averaging, and are written as:

Mass

$$\frac{\partial \overline{\rho}}{\partial t} + \frac{\partial}{\partial x_i}(\overline{\rho}\,\widetilde{u}_i) = 0 \tag{2.18}$$

Momentum

$$\frac{\partial \overline{\rho}\,\widetilde{u}_i}{\partial t} + \frac{\partial}{\partial x_i}(\overline{\rho}\,\widetilde{u}_i\,\widetilde{u}_j) = -\frac{\partial \overline{p}}{\partial x_j} + \frac{\partial}{\partial x_i}(\overline{\tau}_{ij} - \overline{\rho\widetilde{u_i''u_j''}}) + \overline{S}_{M,i} \tag{2.19}$$

Species

$$\frac{\partial \overline{\rho}\,\widetilde{Y}_k}{\partial t} + \frac{\partial}{\partial x_i}(\overline{\rho}\,\widetilde{u}_i\,\widetilde{Y}_k) = -\frac{\partial}{\partial x_i}(\overline{V_{k,i}Y_k} + \overline{\rho\widetilde{u_i''Y_k''}}) + \overline{\dot{\omega}}_k \tag{2.20}$$

Energy

$$\frac{\partial \overline{\rho}\,\widetilde{h}_s}{\partial t} + \frac{\partial}{\partial x_i}(\overline{\rho}\,\widetilde{u}_i\,\widetilde{h}_s) = \frac{\overline{DP}}{Dt} - \frac{\partial}{\partial x_i}(\overline{q_i} + \overline{\rho u_i''h_s''}) + \overline{\tau_{ij}\frac{\partial u_i}{\partial x_j}} + \overline{\dot{\omega}}_T + \overline{\dot{Q}} + \overline{S}_H \tag{2.21}$$

The objective of turbulent modelling is to achieve closures for all unknown terms in a set of RANS equations. In Eqs. (2.18) to (2.21), the following terms remained unclosed:

1. Reynolds stresses $\overline{\rho}\widetilde{u_i'' u_j''}$

2. Turbulent fluxes of species $\overline{\rho}\widetilde{u_i'' Y_k''}$ and energy $\overline{\rho}\widetilde{u_i'' h_s''}$

3. Laminar fluxes of species $\overline{V_{k,i} Y_k}$ and energy $-\overline{\lambda \frac{\partial T}{\partial x_i}}$

4. Chemical reaction rate $\overline{\dot{\omega}}_k$ and combustion caused heat release $\overline{\dot{\omega}}_T$

5. Other source terms $\overline{S}_{M,i}$, $\overline{S}_H$, and $\overline{\dot{Q}}$

Different models are used to identify these unknown terms, models for Reynolds stresses and chemical reaction rate are called turbulence model and combustion model respectively.

2.3. TURBULENCE MODEL

Models are used to close the unknown quantity Reynolds stresses $\overline{\rho}\widetilde{u_i'' u_j''}$ in momentum equation. In this section, different models are introduced.

Based on the turbulent viscosity hypothesis (Boussinesq expression) [28], the turbulent Reynolds stresses $R_{ij} = \overline{\rho}\widetilde{u_i'' u_j''}$ are generally by analogy with the viscous tensor τ_{ij} for Newtonian fluids (Eq. (2.3)) as:

$$\overline{\rho u_i'' u_j''} = \overline{\rho}\widetilde{u_i'' u_j''} = -\mu_t(\frac{\partial \widetilde{u}_i}{\partial x_j} + \frac{\partial \widetilde{u}_j}{\partial x_i} - \frac{2}{3}\delta_{ij}\frac{\partial \widetilde{u}_i}{\partial x_i}) + \frac{2}{3}\overline{\rho}k \tag{2.22}$$

where μ_t is the turbulent dynamic viscosity, which is unclosed and will be further defined in the following turbulence models. The last term in Eq. (2.22) turbulence kinetic energy k is defined as:

$$k = \frac{1}{2}\sum_{i=1}^{3}\widetilde{u_i'' u_i''} \tag{2.23}$$

In Eq. (2.22), the turbulent dynamic viscosity μ_t is still unknown. Three main approaches have been proposed, classified as zero-equation model (Prandtl mixing length model), one-equation model (Prandtl-Kolmogorov model) and two-equations model ($k-\epsilon$ and $k-\omega$ model). In this thesis, the $k-\epsilon$ approach is used, the turbulent viscosity in this case is estimated as[29]:

$$\mu_t = \overline{\rho}C_\mu\frac{k^2}{\epsilon} \tag{2.24}$$

where ϵ is the turbulence energy dissipation rate. The model constant C_μ is empirically set to a value of 0.09. The problem now is to find closures for k and ϵ.

2.3.1. Standard $k - \epsilon$ Model

Standard $k - \epsilon$ model is a two-equation closure turbulence model based on kinetic energy and dissipation rate transport equations:

$$\frac{\partial}{\partial t}(\overline{\rho}k) + \frac{\partial}{\partial x_i}(\overline{\rho}\widetilde{u}_i k) = \frac{\partial}{\partial x_i}[(\mu + \frac{\mu_t}{\sigma_k})\frac{\partial k}{\partial x_i}] + P_k - \overline{\rho}\epsilon - Y_M \tag{2.25}$$

$$\frac{\partial}{\partial t}(\overline{\rho}\epsilon) + \frac{\partial}{\partial x_i}(\overline{\rho}\widetilde{u}_i \epsilon) = \frac{\partial}{\partial x_i}[(\mu + \frac{\mu_t}{\sigma_\epsilon})\frac{\partial \epsilon}{\partial x_i}] + C_{\epsilon 1}\frac{\epsilon}{k}P_k - C_{\epsilon 2}\overline{\rho}\frac{\epsilon^2}{k} \tag{2.26}$$

The source term P_k is the generation of turbulence kinetic energy due to the mean velocity gradients, which is calculated by:

$$P_k = -\overline{\rho}\widetilde{u_i'' u_j''}\frac{\partial \widetilde{u}_i}{\partial x_j} \tag{2.27}$$

Y_M represents the contribution of the fluctuating dilatation in compressible turbulence to the overall dissipation rate, which is calculated by the equation proposed by Sarkar[30]:

$$Y_M = 2\rho\epsilon M_t^2 \tag{2.28}$$

where M_t is the turbulent Mach number defined by kinetic energy k and speed of sound $a(\equiv \sqrt{\gamma RT})$:

$$M_t = \sqrt{k/a^2} \tag{2.29}$$

The equation contains four constants: $\sigma_k, \sigma_\epsilon, C_{\epsilon 1}, C_{\epsilon 2}$, with the following default values[31]:

$$\sigma_k = 1.00, \ \sigma_\epsilon = 1.30, \ C_{\epsilon 1} = 1.44, \ C_{\epsilon 2} = 1.92. \tag{2.30}$$

σ_k and σ_ϵ are the turbulent Prandtl numbers for k and ϵ, respectively.

2.3.2. RNG $k - \epsilon$ Model

RNG $k - \epsilon$ model is similar with standard $k - \epsilon$ model but it has some improvements. The transport equations are adjusted to the following form:

$$\frac{\partial}{\partial t}(\overline{\rho}k) + \frac{\partial}{\partial x_i}(\overline{\rho}\widetilde{u}_i k) = \frac{\partial}{\partial x_i}(\alpha_k \mu_{eff}\frac{\partial k}{\partial x_i}) + P_k - \overline{\rho}\epsilon - Y_M \tag{2.31}$$

$$\frac{\partial}{\partial t}(\overline{\rho}\epsilon) + \frac{\partial}{\partial x_i}(\overline{\rho}\widetilde{u}_i \epsilon) = \frac{\partial}{\partial x_i}(\alpha_\epsilon \mu_{eff}\frac{\partial \epsilon}{\partial x_i}) + C_{\epsilon 1}\frac{\epsilon}{k}P_k - C_{\epsilon 2}\overline{\rho}\frac{\epsilon^2}{k} - R_\epsilon \tag{2.32}$$

The RNG $k - \epsilon$ model has following improvements:

1. RNG $k - \epsilon$ model adds an additional term in its ϵ equation in order to increase the

accuracy for rapidly strained flows.

2. The effect of swirl on turbulence is considered in order to adapt to swirling flows.

3. The Prandtl number could be adjusted.

4. RNG $k - \epsilon$ model provides an analytically-derived effective viscosity formula for low-Reynolds number fluid.

The added terms α_k and α_ϵ are the inverse effective Prandtl numbers, the values of model constants $C_{\epsilon 1}$ and $C_{\epsilon 2}$ are adjusted to 1.42 and 1.68 respectively.

From Eq. (2.32), it is clear that in low-Reynolds-number flow regions where $k \to 0$ the model has problem due to the uncertainty of term $1/k$. A differential equation for turbulent viscosity needs to be used in order to eliminate the drawback:

$$d(\frac{\rho^2 k}{\sqrt{\epsilon \mu}}) = 1.72 \frac{\hat{v}}{\sqrt{\hat{v}^3 - 1 + C_v}} d\hat{v} \qquad (2.33)$$

where $\hat{v} = \mu_{eff}/\mu$ and C_v is a constant whose value is 100.

The differential relation in Eq. (2.33) expresses the effective viscosity v_{eff} in terms of turbulence kinetic energy k and turbulence dissipation rate ϵ. The modification allows the RNG model to better handle the low Reynolds number and near-wall region. For the high-Reynolds number condition ($\hat{v} \gg 1$), the effective viscosity in RNG model is still calculated through equation (2.24), but the recommended value of constant C_μ is slightly changed to 0.0845.

The largest difference between RNG $k - \epsilon$ model and standard $k - \epsilon$ model is the addition of term R_ϵ, which could be defined by the equation below:

$$R_\epsilon = \frac{C_\mu \rho \eta^3 (1 - \eta/\eta_0)}{1 + \beta \eta^3} \frac{\epsilon^2}{k} \qquad (2.34)$$

where $\eta \equiv \sqrt{S_{ij} S_{ij}} k/\epsilon$ (the definition of S_{ij} is given in equation 2.38), $\eta_0 = 4.38$, $\beta = 0.012$. Besides, ANSYS Fluent also provides an option of modifying the turbulent viscosity in terms of swirl and rotation.

2.3.3. REALIZABLE $k - \epsilon$ MODEL

Compared to standard $k - \epsilon$ model, realizable $k - \epsilon$ model has two main improvements:

1. An alternative formulation of turbulent viscosity, which is also different from RNG $k - \epsilon$ model.

2. A modified dissipation rate equation based on the transport of the mean-square vorticity fluctuation.

The turbulence kinetic energy transportation equation is the same as equation (2.25), the dissipation rate transportation is as following:

$$\frac{\partial}{\partial t}(\overline{\rho}\epsilon) + \frac{\partial}{\partial x_i}(\overline{\rho}\widetilde{u}_i\epsilon) = \frac{\partial}{\partial x_i}[(\mu + \frac{\mu_t}{\sigma_\epsilon})\frac{\partial\epsilon}{\partial x_i}] + \overline{\rho}C_1 S\epsilon - \overline{\rho}C_2\frac{\epsilon^2}{k + \sqrt{\nu\epsilon}} \qquad (2.35)$$

again the eddy viscosity is computed by equation (2.24), but C_μ is no longer a constant[32]:

$$C_\mu = \frac{1}{A_0 + A_s\frac{kU^*}{\epsilon}} \qquad (2.36)$$

where U^* is related to both mean deformation tensor S_{ij} and mean rotation tensor $\widetilde{\omega}_{ij}$ in order to take into account the effect of solid body rotation or reference frame rotation on the turbulence through the equation below:

$$U^* = \sqrt{S_{ij}S_{ij} + \widetilde{\omega}_{ij}\widetilde{\omega}_{ij}} \qquad (2.37)$$

$$S_{ij} \equiv \frac{1}{2}(\frac{\partial\widetilde{u}_i}{\partial x_j} + \frac{\partial\widetilde{u}_j}{\partial x_i}) \qquad (2.38)$$

$$\widetilde{\omega}_{ij} = \omega_{ij} - 2\epsilon_{ijk}\omega_k, \ \omega_{ij} = \overline{\omega_{ij}} - \epsilon_{ijk}\omega_k \qquad (2.39)$$

$$\omega_{ij} \equiv \frac{1}{2}(\frac{\partial\widetilde{u}_i}{\partial x_j} - \frac{\partial\widetilde{u}_j}{\partial x_i}) \qquad (2.40)$$

$\overline{\omega_{ij}}$ denotes the mean rotation rate viewed in a rotating reference frame with the angular velocity ω_k. ϵ_{ijk} is the alternating tensor and its value is equal to 1 when ijk is under cyclic order, -1 under anti-cyclic order and 0 if any two indices are equal.$C_1 = max[0.43, \eta/(\eta+5)]$, C_2=1.9, $A_0 = 4.04$ and $A_S = \sqrt{6}cos\phi$ are model constants, where

$$\eta = k\sqrt{S_{ij}S_{ij}}/\epsilon \qquad (2.41)$$

$$\phi = \frac{1}{3}cos^{-1}(\sqrt{6}\frac{S_{ij}S_{jk}S_{ki}}{\sqrt{S_{ij}S_{ij}}^3}) \qquad (2.42)$$

With the adjustment of C_μ, the effect of rotation rate is included, which makes the results better than the standard $k - \epsilon$ model in almost all the cases tested, including rotating homogeneous shear flows; boundary-free shear flows; channel and flat boundary layer; flows with and without pressure gradients; and backward facing step flows[33].

2.3.4. REYNOLDS STRESS MODEL

Reynolds Stress Model (RSM) is a second order turbulence model which goes beyond the Boussinesq assumption(2.22). Different from the isotropic viscosity hypothesis models,

Reynolds Stress Model takes into account the effect of swirl, rotation and rapid change in strain rate by solving transport equations for the Reynolds stresses[34] are modelled independently, which implies that the normal Reynolds stresses could be various. An additional transportation equation for energy dissipation rate is still needed. Take into account symmetry, $\widetilde{u_i'' u_j''} = \widetilde{u_j'' u_i''}$, for 2-D case, five additional equations need to be solved (four Reynolds Stresses $\widetilde{u'' u''}$, $\widetilde{u'' v''}$, $\widetilde{v'' v''}$, and $\widetilde{w'' w''}$ plus one dissipation transportation), while seven equations are needed for 3-D case (six Reynolds stresses plus one dissipation transportation), which increases the computational time. The Reynolds stress transportation equation is given below:

$$\frac{\partial}{\partial t}(\overline{\rho} \widetilde{u_i'' u_j''}) + \frac{\partial}{\partial x_k}(\overline{\rho} \widetilde{u}_k \widetilde{u_i'' u_j''}) = D_{T,ij} + D_{L,ij} + P_{ij} + \phi_{ij} + \epsilon_{ij} + M_{ij} \tag{2.43}$$

The terms on the right hand side are as follow:

TURBULENT DIFFUSION

$$D_{T,ij} = -\frac{\partial}{\partial x_k}[\overline{\rho u_i'' u_j'' u_k''} + \overline{p'(\delta_{kj} u_i'' + \delta_{ik} u_j'')}] \tag{2.44}$$

MOLECULAR DIFFUSION

$$D_{L,ij} = \frac{\partial}{\partial x_k}(\mu \frac{\partial}{\partial x_k} \widetilde{u_i'' u_j''}) \tag{2.45}$$

SHEAR STRESS GENERATION

$$P_{ij} = -(\overline{\rho \widetilde{u_i'' u_k''}} \frac{\partial \widetilde{u}_j}{\partial x_k} + \overline{\rho \widetilde{u_j'' u_k''}} \frac{\partial \widetilde{u}_i}{\partial x_k}) \tag{2.46}$$

PRESSURE STRAIN

$$\phi_{ij} = \overline{p'(\frac{\partial u_i''}{\partial x_j} + \frac{\partial u_j''}{\partial x_i})} \tag{2.47}$$

DISSIPATION

$$\epsilon_{ij} = -2\mu \overline{\frac{\partial u_i''}{\partial x_k} \frac{\partial u_j''}{\partial x_k}} \tag{2.48}$$

PRODUCTION BY SYSTEM ROTATION

$$M_{ij} = -2\overline{\rho}\Omega_k(\widetilde{u_j'' u_m''}\epsilon_{ikm} + \widetilde{u_i'' u_m''}\epsilon_{jkm}) \tag{2.49}$$

Among these terms, $D_{L,ij}$, P_{ij}, and M_{ij} are closed and do not need modelling. However, other terms, including $D_{T,ij}$, ϕ_{ij}, and ϵ_{ij} still need to be modelled in order to close the transport equations. The following descriptions are the model used in ANSYS Fluent.

1. MODELLING OF TURBULENT DIFFUSIVE TRANSPORTATION

The turbulence diffusive transportation $D_{T,ij}$ can be modelled by Daly and Harlow's generalized gradient-diffusion model[35], but an alternative model proposed by F.S.Lien et al.[36] is chosen by ANSYS Fluent in case of numerical instabilities, which is shown below:

$$D_{T,ij} = \frac{\partial}{\partial x_m}(\frac{\mu_t}{\sigma_k}\frac{\partial \widetilde{u_i'' u_j''}}{\partial x_m}) \tag{2.50}$$

where σ_k is set to be 0.82.

2. MODELLING OF DISSIPATION RATE

The dissipation tensor is commonly believed to be isotropic (which means that the term has the same value in every rotated coordinate system) at high turbulence Reynolds numbers. This can be modelled by the equation below[37]:

$$\epsilon_{ij} = \frac{2}{3}\delta_{ij}(\rho\epsilon + Y_M) \tag{2.51}$$

where ϵ is called scalar dissipation rate. The additional dilatation dissipation term Y_M is the same as in the standard $k - \epsilon$ equations. An additional transport equation for dissipation rate is needed, which is similar to the scalar dissipation transportation in the standard $k - \epsilon$ model:

$$\frac{\partial}{\partial t}(\overline{\rho}\epsilon) + \frac{\partial}{\partial x_i}(\overline{\rho}\widetilde{u}_i\epsilon) = \frac{\partial}{\partial x_i}[(\mu + \frac{\mu_t}{\sigma_\epsilon})\frac{\partial \epsilon}{\partial x_i}] + C_{\epsilon1}\frac{1}{2}P_{ii}\frac{\epsilon}{k} - C_{\epsilon2}\overline{\rho}\frac{\epsilon^2}{k} \tag{2.52}$$

where σ_ϵ=1.0, $C_{\epsilon1}$=1.44, and $C_{\epsilon1}$=1.92 are model constants.

3. MODELLING OF PRESSURE STRAIN

Modelling of pressure strain term ϕ_{ij} is very important in RSM. A lot of models have been proposed, ANSYS Fluent uses the following approach:

$$\phi_{ij} = \phi_{ij,1} + \phi_{ij,2} + \phi_{ij,w} \tag{2.53}$$

The first term on the right hand side $\phi_{ij,1}$ is the slow pressure strain term which was first approximated by Rotta[38].

$$\phi_{ij,1} = -C_1\rho\frac{\epsilon}{k}(\widetilde{u_i'' u_j''} - \frac{2}{3}\delta_{ij}k) \tag{2.54}$$

where $C_1 = 1.8$. The second term $\phi_{ij,2}$ is called the rapid pressure strain.

$$\phi_{ij,2} = -C_2[(P_{ij} + M_{ij} - C_{ij}) - \frac{2}{3}\delta_{ij}(P - C)] \tag{2.55}$$

where $C_{ij} \equiv \partial(\overline{\rho}\widetilde{u}_k\widetilde{u_i''u_j''})/\partial x_k$ is the convection term on the left-hand-side, C_2 is a constant value of 0.60. $P = 1/2P_{kk}$ and $C = 1/2C_{kk}$. The third term $\phi_{ij,w}$ is named as wall-reflection term, which is responsible for the redistribution of normal stresses near the wall. It was first defined by Gibson and Launder[39], and improved by Craft and Launder[40], which avoids the former's inappropriate near-wall enhancement of isotropisation at impingement/reattachment regions[36].

2.4. CLOSURE OF DIFFUSION TERMS

Two species diffusion terms $\overline{V_{k,i}Y_k}$ and $\widetilde{u_i''Y_k''}$ need to be closed, named as molecular diffusion and turbulent diffusion, respectively. The molecular diffusion terms are generally neglected compared to turbulent diffusion, but the two terms can be of comparable magnitude in certain regions in turbulent combustion[41]. In this thesis, both terms are considered. It has been mentioned before that the molecular diffusion can be better predicted by the Hirschfelder and Curtiss approximation (2.8). For RANS simulation, the mean molecular diffusion terms are modelled as following:

$$\overline{V_{k,i}Y_k} = -\overline{\rho D_k\frac{\partial Y_k}{\partial x_i}} \approx -\overline{\rho}\overline{D}_k\frac{\partial \widetilde{Y}_k}{\partial x_i} \tag{2.56}$$

where D_k is calculated in the same way as Eq. (2.9) but using mass fraction and mean mole fraction. The turbulent diffusion terms can be modelled by a classical gradient diffusion assumption in the following way:

$$\overline{\rho}\widetilde{u_i''Y_k''} = -\frac{\mu_t}{Sc_{kt}}\frac{\partial \widetilde{Y}_k}{\partial x_i} \tag{2.57}$$

where the turbulent viscosity μ_t is estimated from the turbulence model as Eq. (2.24), and Sc_{kt} is the turbulent Schmidt number for species k:

$$Sc_{kt} = \frac{\mu_t}{\overline{\rho}D_{k,t}} \tag{2.58}$$

$D_{k,t}$ is the effective mass diffusion due to turbulence. In most flows, a constant Sc_{kt} number 0.7 is appropriate.

Two energy diffusion terms, laminar heat diffusive flux $-\overline{\lambda\partial T/\partial x_i}$ and turbulent heat diffusive flux $\overline{\rho}\widetilde{u_i''h_k''}$ should be modelled. The laminar heat diffusion term is normally

rewritten through a mean thermal diffusivity $\overline{\lambda}$ as:

$$-\overline{\lambda \frac{\partial T}{\partial x_i}} = -\overline{\lambda} \frac{\partial \widetilde{T}}{\partial x_i} \tag{2.59}$$

The turbulent heat diffusion term can be modelled using a similar method as used for turbulent species diffusion:

$$\overline{\rho \widetilde{u_i'' h_s''}} = -\frac{\mu_t}{Pr_{st}} \frac{\partial \widetilde{h}_s}{\partial x_i} \tag{2.60}$$

The turbulent Prandtl number Pr_{st} denotes the ratio of momentum to heat diffusivity:

$$Pr_{st} = \frac{\mu_t}{\overline{\rho} D_{st}} \tag{2.61}$$

where D_{st} is the turbulent heat diffusivity. The default turbulent Prandtl number is 1.

2.5. Combustion Model

A combustion model is used to specify the mean reaction source term in RANS equations, various models have been proposed. The Eddy Dissipation Concept (EDC) model is used in this thesis.

2.5.1. Chemical Reaction

A detailed chemical mechanism generally contains a number of elementary Arrhenius reactions. Consider a N-species chemical reaction contains M elementary reactions, the reaction can be represented by:

$$\sum_{k=1}^{N} v'_{kj} \mathbf{M}_k \rightleftharpoons \sum_{k=1}^{N} v''_{kj} \mathbf{M}_k \quad \text{for} \quad j \in [1, M] \tag{2.62}$$

where $\mathbf{M}_k$ denotes species k, v'_{kj} and v''_{kj} are molar stoichiometric coefficients of species k in reaction j.

The total reaction rate of a species $\dot{\omega}_k$ (with unit of $kg s^{-1} m^{-3}$) is the sum of all rates $\dot{\omega}_{kj}$ in M reactions:

$$\dot{\omega}_k = \sum_{j=1}^{M} \dot{\omega}_{kj} = M_k \sum_{j=1}^{M} (v''_{kj} - v'_{kj}) \mathcal{Q}_j \tag{2.63}$$

where $\mathcal{Q}_j$ is the rate of progress of reaction j. The mass conservation should always hold. Therefore $\sum_{k=1}^{N} \dot{\omega}_k = 0$.

For a non-reversible reaction, the process rate $\mathcal{Q}_j$ is given by:

$$\mathcal{Q}_j = K_{fj} \prod_{k=1}^{N} [X_k]^{\nu'_{kj}} \tag{2.64}$$

where molecular concentration $[X_k] = \rho Y_k / W_k$.

The rate constant K_{fj} is strongly depend on temperature, which is given by Arrhenius law:

$$K_{fj} = A_{fj} T^{\beta_j} exp(-\frac{E_{aj}}{RT}) \tag{2.65}$$

where A_{fj} is called pre-exponential constant, β_j is the temperature exponent, and E_{aj} is the activation energy. In the database of chemical reactions used in this thesis, the quantities are given in the following units: the units of A_{fj} are $1/s$, $cm^3/mol/s$, $cm^6/mol^2/s$ for first, second, and third order reactions, respectively; T is in Kelvin; and E_{aj} is in $cal/mol/K$ with $R = 1.987 cal/mol/K$. The chemical time scale for first order reaction is the reciprocal of K_{fj}.

2.5.2. TURBULENCE-CHEMISTRY INTERACTION

According to Veynante and Vervisch[42], all numerical modelings of the reaction rate term are either based on a purely statistical view or more oriented on a geometrical view of turbulent flames. mixing analysis and chemical and turbulent time scales are widely used in almost all combustion models. The models can be classified into three categories:

1. Geometrical analysis:
   Identifying the flame front as a geometrical surface inside the turbulent flow, which is generally combined with flamelet assumptions under which the flame elements are seen as laminar flame, and the reaction rates in flamelet are evaluated.

2. Turbulent mixing:
   This approach assumes that the turbulent mixing is controlling the rate of the chemical conversion, such as the well know Eddy Break Up (EBU) model, which limits the method to very fast chemical reaction case only.

3. One-point statistics:
   This is a direct method without flamelet assumption or mixing-controlled combustion hypothesis. It uses a kinetic scheme and the joint probability density function of species and enthalpy, which is know as the PDF model.

Turbulent flames can be classified according to whether they are premixed or not. Combustion models have different capability of treating the premixed or nonpremixed combustion case, or both, and with respect to assumptions about the chemistry (finite rate

chemistry or infinitely fast chemistry). Table 2.1 schematically represents the applicability of different models for infinitely fast chemistry and for finite rate chemistry assumption. For more details, please refer to [22, 43]. These models are suitable for either premixed combustion or non-premixed combustion case.

Table 2.1: Classification of turbulent combustion models in terms of chemistry and mixing

	premixed	non-premixed
Infinitely fast chemistry	Eddy Break Up (EBU)[12]	
	Bray Moss Libby (BML) [1]	Conserved Scalar-equillibrium Model[12]
Finite rate chemistry	Probability Density Function (PDF)[12] Eddy Dissipation Concept (EDC)[12] Conditional Source-term Estimation (CSE)[12]	
	Turbulent Flame Speed Correction (G-equation)[12] Flamelet (based on flame surface density)[12]	Conditional Momentum Closure (CMC)[12] Flamelet (based on mixture fraction)[12]
	Linear Eddy Model[2] Laminar Finite Rate Model[12]	

[1] Could be used in RANS
[2] Could be used in LES

2.5.2.1. EDDY DISSIPATION CONCEPT (EDC)

CASCADE MODEL

The laminar finite-rate model calculates the chemical source term $\overline{\dot{\omega}}_k$ through Arrhenius expression, ignoring the effect of fluctuations. The expression is developed for laminar flame, and is not accurate for most turbulent flames. To overcome the drawback of misestimating the turbulent flames by Arrhenius law, the Eddy Break Up (EBU) model proposed by Spalding[44] couples the Arrhenius law and turbulent motions, thus the reaction rate could be ruled more precise. The Eddy Dissipation Concept (EDC) model proposed by Magnussen and Hjertager is directly extended from the EBU model[45]. As is shown in table 2.1, EDC is used for turbulent combustion under the finite rate chemistry assumption, whose chemical time scale is governed by Arrhenius law. EDC follows the hypothesis of EBU model that the reaction zone is viewed as a collection of reactants pockets transported by turbulent eddies[22], in other words, the region where molecular mixing and reaction of reactants occurs only takes up a limited fraction of the total volume of fluid, which is related to the dissipation of turbulence[46], thus the model is named as "eddy dissipation".

According to Ertesvåg et al[47], the model could be seen as an energy cascade model, it transfers mechanical energy from the large-scale eddies to small eddies, the largest ed-
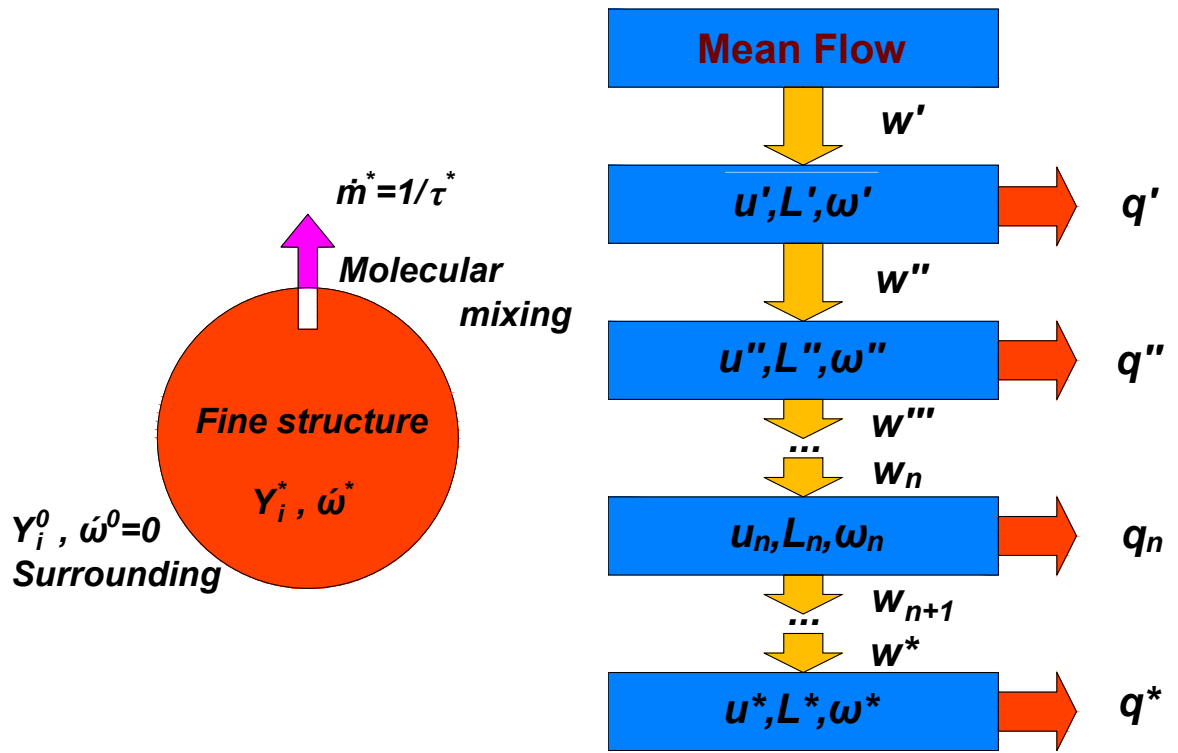
(a) Fine structure

(b) Energy cascade model: transfer of mechanical energy from large to small eddies

Figure 2.1: Basic concept of EDC model

dies hold most part of kinetic energy while the smallest contain the largest viscous stresses and swirl fasted. The mechanical energy is dissipated through viscous friction, which is the largest in small eddies. Fine structure, which is defined as the only reacting region in turbulent combustion flows, is an important concept in EDC model. As is shown in Fig. 2.1 (a), locally molecular mixing of reactants leads to chemical reaction. The scales of smallest eddies (fine structures, characterized by *) are considered to be of the same order of Kolmogorov scales.

w in Fig. 2.1 (b) denotes the transfer of mechanical energy, and the sum of heat generated at each level (q) is the turbulent dissipation rate ϵ. The subscript refers to the number of cascade level. The first cascade level has a turbulent velocity scale of $u' = \sqrt{2k/3}$, a length scale L', and a eddy frequency given by $\omega' = u'/L'$ [46]. Turbulent kinetic energy k and eddy dissipation rate ϵ are characterized by $k-\epsilon$ turbulence model or RSM. It is assumed that the eddy frequency doubles at each two conjoint levels, leading to $w_n = 2w_{n-1} = u_n/L_n$, where n denotes the n-th level.

The feed of mechanical energy to each level and the viscous energy dissipation on this

level are expressed by Ertesvåg and Magnussen[47] using two model constants C_{D1} and C_{D2}:

$$w_n = \frac{3}{2} C_{D1} \omega_n u_n^2 \tag{2.66}$$

$$q_n = C_{D2} \nu \omega_n^2 \tag{2.67}$$

Under a quasi-steady assumption, an energy conservation is satisfied:

$$w_n = q_n + w_{n+1} \tag{2.68}$$

Two important cascade levels, the first largest eddy level and the smallest fine structure eddy level, should be analysed. Consider the smallest level ($n = *$), the mechanical energy can not be transferred to a smaller level, which makes w_{n+1} in Eq. (2.68) equal to 0:

$$w^* = \frac{3}{2} C_{D1} \omega^* u^{*2} = q^* = C_{D2} \nu \omega^{*2} \tag{2.69}$$

For turbulent flows, the viscous dissipation is larger under higher strain rate (eddy frequency). On the first level ($n = '$), the strain rate is the smallest, and could be neglected compared to the magnitude of mechanical energy, the energy conservation (2.68) is thus:

$$w' = \frac{3}{2} C_{D1} \omega' u'^2 = w'' \tag{2.70}$$

As is mentioned, the sum of dissipation rate on each level is assumed to be equal to the dissipation rate of the turbulence,

$$w' = \sum q_n = \epsilon \tag{2.71}$$

From Eq. (2.70) and Eq. (2.71), using the expression of the first level strain rate $\omega' = u'/L'$, one obtains:

$$\epsilon = \frac{3}{2} C_{D1} \frac{u'^3}{L'} \tag{2.72}$$

The product of u' and L' is the turbulent viscosity ν_t, and using $u' = \sqrt{2k/3}$, one finds:

$$\nu_t = \frac{2}{3} C_{D1} \frac{k^2}{\epsilon} \tag{2.73}$$

Within $k - \epsilon$ model and RSM, the definition of $\nu_t (= \mu_t / \overline{\rho})$ is given by Eq. (2.24), thus $C_\mu = 2/3 C_{D1} = 0.09$, $C_{D1} = 0.135$. As is mentioned before, it is defined that $\omega_{n+1} = 2\omega_n$, and the sum of heat generation on each level is thus[48]:

$$\epsilon = (1 + \frac{1}{4} + \frac{1}{16} + ...) q^* = \frac{4}{3} q^* \tag{2.74}$$

Applying the heat generation expression (2.67),

$$\epsilon = \frac{4}{3} C_{D2} \nu \frac{u^{*2}}{L^{*2}} \tag{2.75}$$

Using Eq. (2.69),

$$\epsilon = 2 C_{D1} \frac{u^{*3}}{L^*} \tag{2.76}$$

The two C_{D1} and C_{D2} related turbulent dissipation rate expressions are very important formulas in the EDC model. According to Magnussen[46], $C_{D2} = 0.5$. Together with $C_{D1} = 0.09$, the choice of these two values are believed to be the best to fit for most combustion applications. By combining Eq. (2.75) and Eq. (2.76), one obtains:

$$Re^* = \frac{u^* L^*}{\nu} = \frac{2 C_{D2}}{3 C_{D1}} \approx 2.5 \tag{2.77}$$

For Kolmogorov scale, the Reynolds number is unity, so the fine structure scales of EDC model are of the same order as Kolmogorov scales.

REACTION RATE

According to Magnussen[49], the reaction rate is proportional to product of the transfer of mass between the fine structure and the surrounding fluid $\dot{m}$ (per unit mass of fluid and unit of time), χ, and the difference in mass fraction inside and outside the fine structures (the surroundings is labelled by ^{o} and fine structures are denoted by *):

$$\overline{\dot{\omega}}_i = \dot{m} \chi (Y_i^o - Y_i^*) \tag{2.78}$$

The proportionality constant χ expresses the fraction of the active fine structures. According to Gran and Magnussen[50], the fraction χ is declared to be 1. Let γ^* and τ^* denotes the volume fraction occupied by fine structures and the residence time of reactants inside fine structures, respectively. Gran and Magnussen argued that the mass exchange rate $\dot{m}$ between fine structures and surroundings should be modeled as $\gamma^{*2/3}/\tau^*$[50]. The identification of values of the volume fraction and the residence time scale are of great importance in the EDC model, and is addressed in the next paragraph.

Eq. (2.75) and (2.76) relate fluid motion property turbulence dissipation rate ϵ and material property viscosity ν to the velocity scale u^* and length scale L^* of fine structure. After some derivations, an explicit expression of u^* and L^* can be written:

$$L^* = \frac{2}{3} \left(\frac{3 C_{D2}^3}{C_{D1}^2}\right)^{1/4} \left(\frac{\nu^3}{\epsilon}\right)^{1/4} \tag{2.79}$$

$$u^* = (\frac{C_{D2}}{3C_{D1}^2})^{1/4}(\nu\epsilon)^{1/4} \tag{2.80}$$

The two scales above are used to calculate γ^* and τ^* mentioned before as follows.

Magnussen et al. proposed the expression of fine structures volume fraction γ^* on the basis of consideration of the energy transfer to the dissipative structures[51]:

$$\gamma^* = (\frac{u^*}{u'})^3 = (\frac{3C_{D2}}{4C_{D1}^2})^{3/4}(\frac{\nu\epsilon}{k^2})^{3/4} \tag{2.81}$$

Take into account Eq. (2.72) and Eq.(2.76), the postulate in Eq. (2.81) implies that:

$$\gamma^* \approx \frac{L^*}{L'} \tag{2.82}$$

Here, a factor of 3/4 is left out[47].

The residence time scale τ^* is the reciprocal of the mass transfer between the fine structures and the surroundings, this mass exchange rate can be modelled as[51]:

$$\dot{m}^* = 2\frac{u^*}{L^*} = (\frac{3}{C_{D2}})^{1/2}(\frac{\epsilon}{\nu})^{1/2} \tag{2.83}$$

By considering that the fine structures are localized in constant energy regions, the fine structure volume fraction is changed (ratio by length) which is denoted by γ_λ:

$$\gamma_\lambda = \frac{u^*}{u'} = (\frac{3C_{D2}}{4C_{D1}^2})^{1/4}(\frac{\nu\epsilon}{k^2})^{1/4} \tag{2.84}$$

In this way, the mass exchange pass through the fine structures ($\gamma^{*2/3}$) can be replaced by γ_λ^2/τ^*. Thus the reaction rate formula becomes:

$$\overline{\dot{\omega}}_i = \frac{\overline{\rho}\gamma_\lambda^2}{\tau^*}(Y_i^o - Y_i^*) \tag{2.85}$$

Introduce the mean mass averaged fraction concept which is a reactants concentration that takes into account the mass concentration of both the fine structures and the surroundings:

$$\widetilde{Y}_i = \gamma_\lambda^3 Y_i^* + (1 - \gamma_\lambda^3)Y_i^o \tag{2.86}$$

The mean reaction rate is thus:

$$\overline{\dot{\omega}}_i = \frac{\overline{\rho}\gamma_\lambda^2}{\tau^*(1 - \gamma_\lambda^3)}(\widetilde{Y}_i - Y_i^*) \tag{2.87}$$

The reactions proceed over the residence time scale, each iteration would lead to a

change of mass fraction inside fine structures until no difference between the averaged mass fraction and the mass fraction inside fine structures could be found. The In Situ Adaptive Tabulation (ISAT)[52] algorithm is applied in ANSYS Fluent in order to accelerate the simulations, it is a method that tabulates the accessed composition space region in-situ using tolerance control, which enables a two or three orders of magnitude reduction of computational cost. It should be pointed out that different from the original EDC model, the combustion is assumed to occur in a "Plug Flow Reactor(PFR)" rather than a "Perfectly Stirred Reactor (PSR)".[53] In PSR, the reactants are injected into a constant-volume regime from multiple inlets, the products are perfectly stirred with the reactants and the composition everywhere is uniform[54]. In contrast, PFR, inside which the mass fraction and temperature change constantly along the flow direction, is a constant-pressure reactor that integrates the reaction kinetics in time[55], the time scale is determined by Arrhenius law as explained before. According to De et al.[55], only for light exothermal reaction and very small conversion PSR and PFR show similar performance, the PFR is more straightforward and needs less computational efforts, which is most often used.

The two important quantities τ^* and γ_λ could be expressed according to Eq. (2.83) and (2.84):

$$\tau^* = (\frac{C_{D2}}{3})^{1/2}(\frac{\nu}{\epsilon})^{1/2} = C_\tau(\frac{\nu}{\epsilon})^{1/2} \qquad (2.88)$$

$$\gamma_\lambda = (\frac{3C_{D2}}{4C_{D1}^2})^{1/4}(\frac{\nu\epsilon}{k^2})^{1/4} = C_\gamma(\frac{\nu\epsilon}{k^2})^{1/4} \qquad (2.89)$$

where C_τ and C_γ are called residence time constant and fine structure constant, respectively. As is mentioned, $C_{D1} = 0.09$ and $C_{D2} = 0.5$, C_τ and C_γ are thus 0.4083 and 2.1377, respectively. Combined with the reaction rate expression (2.87), a larger residence time constant leads to a lower reaction rate while a larger fine structure constant results in a higher reaction rate.

The default model constants in standard EDC model proposed by Magnussen[46] are suitable for a range of combustion systems. Unfortunately, the model is found to be inappropriate for MILD combustion. The reason will be further discussed in the following chapter. A simple solution is to modify the EDC constant parameters based on the experimental data. De et al.[55] found that a modification of residence time scale constant from 0.4083 to 3 could significantly improve the simulation result of the DJHC burner. Nevertheless, Aminian et al.[56] found in the case of Adelaide JHC burner, increasing the residence time scale constant to 1.5 rather than 3 could give a better agreement. However, Evans et al.[57] declare that a combination of residence time scale constant of 3 and fine structure constant of 1 is the best choice. Obviously, this method is not effective since the constants are case dependent and could not be determined without empirical evidence. Even for the same facility, the best value of model constants could be varying. In this case, development

of an improved EDC model is imperative.

2.5.2.2. PARENTE'S EXTENDED EDC MODEL

Take De et al.'s solution ($C_\tau = 3$) for DJHC burner as an example, the characteristic Reynolds number of fine structures can be calculated through Eq. (2.77), the new Re_T value is changed to 18.3. By changing the model constants, the large value of Re_T in MILD combustion results in a different region of combustion. MILD combustion thus has a larger characteristic dimension than conventional combustion, either the length scale or velocity scale of fine structure should be changed. Recently, Parente et al.[58] proposed an extension of EDC model containing position dependent values of model constants, depending on a local turbulent Reynolds number and a local Damköhler number.

Eq. (2.75) and Eq. (2.76) are two basic equations which link the model constants together with fine structure properties. In the standard EDC model, the chosen values of C_{D1} and C_{D2} makes sure that the fine structure scales u^* and L^* are of the same order of Kolmogorov scales. The fundamental idea of EDC model is to assume the turbulence plays a prior role to chemistry[22]. In the extended EDC model, Kolmogorov length scale is thus kept for L^* ($= (v^3/\epsilon)^{1/4}$) while u^* is replaced. According to Parente et al., for MILD combustion, it is appropriate to consider that the turbulent flame speed S_T as the characteristic velocity of fine structures. For the low Damköhler and high intensity turbulence burner, this speed could be calculated through the following equation[59]:

$$\frac{S_T}{S_L} \approx \sqrt{\frac{D_{st}}{D_{th}}} \tag{2.90}$$

where D_{st} is the turbulent thermal diffusivity and D_{th} the laminar thermal diffusivity. As is described before, the Prandtl number denotes the ratio of momentum diffusivity and thermal diffusivity, if both the turbulent Prandtl number and the Prandtl number based on molecular transport properties are approximately equal to 1, the turbulent flame speed is thus:

$$S_T \approx S_L \sqrt{\frac{v_T}{v}} \tag{2.91}$$

In order to avoid the drawback that when v_T approaches to 0, S_T is 0 instead of approaching S_L, the equation should be improved as:

$$S_T \approx S_L \sqrt{\frac{v_T}{v} + 1} \approx S_L \sqrt{Re_T + 1} \tag{2.92}$$

where $Re_T = k^2/(v\epsilon)$ is the turbulent Reynolds number.

Replacing u^* by the expression of turbulent flame speed S_T in Eq. (2.75), leads to

$$\epsilon = \frac{4}{3} C_{D2} \nu \frac{S_L^2 (Re_T + 1)}{L^{*2}} \tag{2.93}$$

In this way, the value of model constant C_{D2} is related to fluid motion properties and laminar flame speed.

Similarly, combining Eq. (2.75) and Eq. (2.76), the ratio between C_{D1} and C_{D2} is obtained:

$$\frac{C_{D2}}{C_{D1}} = \frac{3}{2} \frac{u^* L^*}{\nu} \tag{2.94}$$

Inserting the expression of flame speed (Eq.(2.92)), this relation can be rewritten:

$$\frac{C_{D2}}{C_{D1}} = \frac{3}{2} \frac{S_L \sqrt{Re_T + 1}}{\nu} L^* \tag{2.95}$$

Parente et al.[58] used an expression of laminar flame velocity proposed by Damköhler[59]:

$$S_L \propto \sqrt{D_{th} K_{fj}} \tag{2.96}$$

For first order reaction,

$$S_L \propto \sqrt{\nu / \tau_c} \tag{2.97}$$

where τ_c is the chemical time scale governed by Arrhenius law. Eq. (2.95) is thus replaced by:

$$\frac{C_{D2}}{C_{D1}} \propto \frac{3}{2} \frac{L^* \sqrt{Re_T + 1}}{S_L \tau_c} \tag{2.98}$$

In this way, both Eq. (2.93) and Eq.(2.98) contain a term L^* / S_L. Alternatively and most generally, the chemical reaction time scale is defined as the time a laminar flame needs to traverse the laminar flame front, derived from the laminar flame thickness δ_L and laminar flame speed S_L:

$$\tau_c = \frac{\delta_L}{S_L} \tag{2.99}$$

In EDC model, as chemical reactions only happen inside the fine structures, a chemical time scale can be defined as the time needed to traverse the fine structures:

$$\tau_c^* = \frac{L^*}{S_L} \tag{2.100}$$

Applying this equality, the equation 2.93 implies:

$$\epsilon = \frac{4}{3} C_{D2} \nu (Re_T + 1) \frac{1}{\tau_c^{*2}} \tag{2.101}$$

This equality is only useful when τ_c^* is know. Parente et al. used Arrhenius law to calculate τ_c^*, in this way assuming $\tau_c = \tau_c^*$.

Damköhler number is a dimensionless number which relates flow time scale to the chemical reaction time scale: $Da_\eta = \tau_\eta/\tau_c$. For standard EDC model, the Damköhler number is evaluated by Kolmogorov scale for the flow, which is $Da_k = \tau_k/\tau_c$, where $\tau_k = (\nu/\epsilon)^{1/2}$. The Damköhler number of fine structures is characterized by $Da^* = \tau_k/\tau_c^*$. Eq. (2.101) can be written as:

$$\epsilon = \frac{4}{3}C_{D2}\nu(Re_T+1)\frac{Da^{*2}}{\tau_k^2} \tag{2.102}$$

The local value of model constant C_{D2} is thus:

$$C_{D2} = \frac{3}{4}\frac{1}{(Re_T+1)Da^{*2}} \tag{2.103}$$

Compared to standard EDC model, the C_{D2} value is changed from a constant to a local property dependent variable. Using the relationship between C_{D1} and C_{D2} (Equation 2.98), functions of both C_{D1} and C_{D2} are known.

As is described before, the two EDC model constants are related to C_{D1} and C_{D2} through Eq. (2.88) and (2.89). According to Parente et al.,

$$C_\tau = (\frac{C_{D2}}{3})^{1/2} \propto \frac{1}{\sqrt{Re_T+1}Da^*} \tag{2.104}$$

$$C_\gamma = (\frac{3C_{D2}}{4C_{D1}^2})^{1/4} \propto \sqrt{(Re_T+1)Da^*} \tag{2.105}$$

The residence time constant is found to be inversely proportional to Da^* while the fine structure scale is proportional to $\sqrt{Da^*}$. The trends of the two constants are opposite, but the effect on reaction rate are similar according to Eq. (2.87), Eq. (2.88), and Eq. (2.89).

2.5.2.3. A NEW EXTENDED EDC MODEL

Parente's extended EDC model gives quantitative expressions for two model constants C_γ and C_τ, which in the case of Adelaide jet-in-hot-coflow burner perform better than the standard EDC model by taking into account the Re_T and Da^* locally [58]. However, an unknown proportionality constant is present in Eq. (2.97). An improved model which can give certain model constants locally without any attempt is needed. The expression of laminar flame speed $S_L \propto \sqrt{\nu/\tau_c}$ is the reason why no quantitatively relations could be derived. It will be shown that equation of S_L is not needed because it can be eliminated. In order to eliminate the uncertainty brought by the expression of flame speed, only the hypothesis of $\tau_c^* = L^*/S_L$ proposed by Parente is kept, Eq. (2.97) is not used. To be more detailed, in Parente's model, the laminar flame velocity S_L in Eq. (2.95) is replaced by a proportional

expression proposed by Damköhler in order to find a term L^*/S_L. In the current model, S_L is eliminated from the model by some derivations. The process is shown as follows.

By assuming $\tau_c^* = L^*/S_L$, Eq. (2.95) is rewritten:

$$\frac{C_{D2}}{C_{D1}} = \frac{3}{2}\frac{S_L\sqrt{Re_T+1}}{\nu}L^* = \frac{3}{2}\frac{\sqrt{Re_T+1}}{\nu}\frac{L^{*2}}{\tau_c^*} \tag{2.106}$$

The term $L^{*2}/(\nu\tau_c^*)$ could be simplified through the definition of Kolmogorov length scale,

$$\frac{L^{*2}}{\tau_c^*\nu} = \frac{(\nu/\epsilon)^{1/2}}{\tau_c^*} \tag{2.107}$$

The numerator is found to be the expression of Kolmogorov length scale, the term $L^{*2}/(\nu\tau_c^*)$ is thus simply equal to a Kolmogorov scale Damköhler number:

$$\frac{L^{*2}}{\tau_c^*\nu} = \frac{(\nu/\epsilon)^{1/2}}{\tau_c^*} = \frac{\tau_k}{\tau_c^*} = Da^* \tag{2.108}$$

In this way, it is found that the ratio of C_{D2} over C_{D1} is directly equal to a function of local turbulent Reynolds number and Kolmogorov scale Damköhler number rather than a proportional relation (Equation 2.98). The equality Eq. (2.103) can also be kept. Finally, the two model constants, C_γ and C_τ, are derived:

$$C_\tau = (\frac{C_{D2}}{3})^{1/2} = \frac{1}{2}\frac{1}{\sqrt{Re_T+1}Da^*} \tag{2.109}$$

$$C_\gamma = (\frac{3C_{D2}}{4C_{D1}^2})^{1/4} = \sqrt{\frac{3}{2}(Re_T+1)}Da^{*3/4} \tag{2.110}$$

It is important to point out that the new extended EDC model shows that the volume fraction constant C_γ is proportional to $Da^{*3/4}$ rather than $Da^{*1/2}$ given by Parente. The new extended EDC model makes it possible to quantitatively determine the model constants locally without empirical justification. The main differences of two models are listed in Table 2.2. In the case of very slow reaction, the volume fraction model constant C_γ can be clipped to values not smaller than the standard value 2.1377 in order to avoid unreasonable late ignition.

Table 2.2: A comparison between different EDC models

EDC Model	Assumption	Model Constants
Standard	Kolmogorov sacles	Constants
Parente's Extended	1. Kolmogorov length sacle 2. $\tau_c^* = \tau_c$ 3. $u^* = S_T = S_L\sqrt{Re_T + 1}$ 4. $S_L = L^*/\tau_c^*$ for C_τ; $\quad S_L \propto \sqrt{\nu/\tau_c}$ for C_γ	Qualitatively dependent on local properties
New Extended	1. Kolmogorov length sacle 2. $\tau_c^* = \tau_c$ 3. $u^* = S_T = S_L\sqrt{Re_T + 1}$ 4. $S_L = L^*/\tau_c^*$ for both C_τ and C_γ	Quantitatively dependent on local properties

3

SIMULATION OF A JET-IN-HOT-COFLOW BURNER

Jet-in-hot-coflow (JHC) burner is used to investigate flameless combustion by imitating the recirculation flow characteristics appearing in a real complex furnace via a hot diluted coflow. A well-defined stream of high temperature, low oxygen concentration combustion products is injected around the fuel jet as oxidizer in order to obtain MILD combustion conditions. The coaxial combustion products can be seen as the recirculation in a real furnace. The advantage is that the combustion parameters can be studied independently due to their high controllability. A variety of JHC burner experiments has been undertaken, which provide an interesting database for simulation validations. Till now, most JHC burners follow the idea of Dally et al.[60]. The Delft jet-in hot coflow (DJHC) is one of the most well-known and extensive experiments among them. Some of the experiments use two coflows to mimic both the recirculating flue gas and air, but the range of influential parameters considered and burner types is limited compared to the first type.

Table 3.1 makes a summary of the existing experiments in order to give an easy and clear comparison. It can be seen that most experiments use methane as the fuel due to its availability and chemical simplicity. Although the fuel compositions in different research are various, many of the fuel or coflow used are diluted with inert species. According to Dally et al.[61], the dilution is beneficial for experiments. The shift of stoichiometric mixture fraction to the higher scalar dissipation region influences the stability and makes the MILD flame lifted over a wider range of fuel jet velocities. The flame can also be more visible, which can help to be better observed. The Adelaide burner studies also investigated C_2H_4 as fuel[62, 63], the drawback of ethylene is the relatively larger soot emission makes the measurement more difficult. The additional fuel species in these cases could reduce

the soot interference. The various fuel dilutions used in different experiments enable the comparison of kinetic effects.

The coflow composition influence is also important. In the table, only the oxygen concentration and temperature are chosen as coflow properties to be compared, as the generation of coflows are so much different that no overlap could be found. According to Medwell et al.[64], the significant coflow difference makes it impossible to make conclusive comments about the transition to MILD combustion and the general behaviour of flames under different conditions. The Adelaide burner uses a porous secondary burner to generate hot combustion products, CH_4 and H_2 mixture (1:1 by volume fraction) is used as the fuel of the secondary burner. The combustion products are mixed with N_2 and air in order to control the oxygen level in coflow[60] as well as cooling down the coflow. Differently, the cooling of DJHC burner coflow [65] is done by radiative heat transfer and conductive heat transfer through the burner pipe. A grid is also used to cool the coflow, which is generated by a partially premixed secondary burner, Dutch natural gas and air are mixed as the fuel. The LJHC burner has a secondary burner using CH_4 and air mixture as fuel to control the coflow, while the hot coflow of EPDB burner is simply the air warmed by a SKORPION air heater[66]. The vitiated coflow uses H_2/Air mixture as the fuel of the coflowing burner, and the products composition is modified by varying the equivalence ratio[21]. The KTH burner's coflow comes from LPG combustion[67]. As is described, the coflow are from different fuel combustion in different cases. In this chapter, the simulations are based on DJHC database.

So far, a number of simulations based on the JHC experiments shown in Table 3.1 have been done, in which different combustion and turbulence models have been used. Table (3.2) summarises the numerical methods applied by different researchers. Among a wide range of simulation methods, RANS is the most widely used, while LES is also chosen by some researchers. For Adelaide burner RANS simulations, Christo and Dally[41] seems to be the first to use a modified standard k-ϵ model on jet-in hot coflow burners. They compared the modified k-ϵ model with standard k-ϵ model, RNG k-ϵ model and realizable k-ϵ model, and declared the modified k-ϵ model is the best for Adelaide burner. The model changes the model constant $C_{\epsilon 1}$ from its original value 1.44 to 1.6, which is reported to significantly improve the performance in round jets[80]. The modified k-ϵ turbulence model is thus adopted by almost all the following researchers. The only exception is Aminian et al.[81]. They tried to model the turbulence with different models (standard k-ϵ, modified standard k-ϵ, RNG k-ϵ, realizable k-ϵ and RSM), and found that the temperature overprediction has nothing to do with the turbulence model used. The modification k-ϵ model is also applied in the vitiated coflow burner[78], while before Christo and Dally's proposal only standard k-ϵ model is used[21, 76].

Table 3.1: A summary of experiments on different jet-in hot coflow burners

| | | Fuel | | | | Coflow | | | |
D [mm]	Component	Volume Fraction [%]	Temperature [K]	Velocity [m/s]	Re	O_2 Volume Fraction [%]	Temperature [K]	Velocity [m/s]	ref
Adelaide burner									
4.25	CH_4/H_2	0.50:0.50	305	70.5	9482	3,6,9	1300	3.2	[60]
4.25	NG^a/H_2	0.50:0.50	305	32.1-96.3	5000-15000	3,9	1100	2.3	[68]
4.6	CH_4/H_2	0.57:0.43	305	5.8-116.3	10000	3,6,9	1300-1600	2.8	[64]
4.25	C_2H_4		305	17.5	10000	3,9	1000	2.3	[62]
4.25	C_2H_4/H_2	0.50:0.50	305	30.6	10000	3,9	1000	2.3	[62]
4.25	C_2H_4/Air	0.25:0.75	305	27.3	10000	3,9	1000	2.3	[62]
4.25	C_2H_4/N_2	0.25:0.75	305	27.3	10000	3,9	1000	2.3	[62]
4.6	NG/H_2	0.50:0.50	305	30.6-62.5	10000	3,9	1100	2.3	[63]
4.6	C_2H_4/H_2	0.50:0.50	305	30.6-62.5	10000	3,9	1100	2.3	[63]
4.6	LPG^b/H_2	0.50:0.50	305	30.6-62.5	10000	3,9	1100	2.3	[63]
Delft jet-in-hot-coflow (DJHC) burner									
4.5	CH_4/N_2	0.85:0.15	360,470	35.6	3000-9500	8.4,9.5	1460,1540	4.3,4.6	[69]
4.5	$CH_4/N2/C_2H_6$	0.81:0.14:0.37	360,470	35.6	3000-9500	8.4,9.5	1460,1540	4.3,4.6	[69]
4.5	DNG^c		360,470	35.6	3000-9500	8.4,9.5	1460,1540	4.3,4.6	[69]
4.5	DNG		360-470	16.8-47.9	2500-8800	8.4,9.5,11.9	1395,1460,1540	4.6	[65, 70, 71]
4.5	DNG/Air	0.25:0.75	470	35.6	9000	8.3	1540	4.6	[71]
4.5	DNG/H_2	0.95-0.85:0.05-0.15	530	35.6-43	5700	9.5	1460	4.3	[72]

[a] NG denotes natural gas
[b] LPG denotes liquefied petroleum gas
[c] DNG denotes Dutch natural gas

D [mm]	Fuel					Coflow			ref
	Component	Volume Fraction [%]	Temperature [K]	Velocity [m/s]	Re	O_2 Volume Fraction [%]	Temperature [K]	Velocity [m/s]	
Laminar jet-in-hot-coflow (LJHC) burner									
7	CH_4/N_2	0.18:0.82	1080-1150	0.0058	unmentioned	3.6 (diluted with N_2)	1530	0.0155	[73]
7	CH_4/N_2	0.18:0.82	1080-1150	0.0059	unmentioned	3.6 (diluted with Ar)	1680	0.0161	[73]
7	$CH_4/H_2/N_2$	0.09:0.09:0.82	1185	0.0058	unmentioned	3.6 (diluted with N_2)	1530	0.0155	[74]
Electrically preheated diffusion (EPDB) burner (laminar)									
7	CH_4/N_2	0.17:0.83	1150	0.0058	unmentioned	3.3 (10/100 ppm NO)	1530	0.0155	[75]
8	CH_4/N_2	0.49:0.51	298	0.0065	unmentioned	21	298	0.0155	[66, 75]
8	CH_4/N_2	0.20:0.80	780	0.0123	unmentioned	21	780	0.0347	[66, 75]
Vitiated coflow burner									
4.57	H_2/N_2	0.25:0.75	305	107	23600	15 (25% H_2)	1045	3.5	[21]
4.57	$CH_4/N_2/O_2$	0.33:0.15:0.52	320	100	28000	12 (15% H_2O)	1350	5.4	[76]
4.57	$CH_4/N_2/O_2$	0.33:0.15:0.52	320	100	23600	H_2/Air product	1355-1475	5.4	[77]
4.57	$CH_4/N_2/O_2$	0.21:0.60:0.19	320	100	28000	14 ($\phi = 0.38$-0.40)	1355	5.3	[78]
KTH burner									
0.97	LPG		299-1121	25-100	1708-13263	5-23.2	1073-1573	0.98	[67]
Axially-staged combustor									
2.5-6	$H_2/CO/N_2$	0.38:0.48:0.14	293	16-299	unmentioned	16.9	841	4.3	[79]

However, a different trend is found in DJHC burner. Dongre et al. [82] and De et al.[83] evaluated the performance of the same combustion models on Adelaide burner and DJHC burner, respectively, and found that the modified k-ϵ model does not give good agreement for the turbulence. They thus used realizable k-ϵ model in DJHC burner and modified k-ϵ model in Adelaide burner. For the choice of turbulence model in DJHC burner, De et al.[55] compared the realizable k-ϵ model and RNG k-ϵ model with the standard k-ϵ model, and proposed the realizable k-ϵ model is the best among the three. Later, Sarras et al.[84] used the RSM as it is the most elaborate model in RANS simulation and the peak temperature is not affected by the turbulence model according to Aminian et al.[81]. In this thesis, a comparison between different k-ϵ models and Reynolds Stress Model in terms of DJHC burner is done and will be shown later.

For PDF models, the mixing models used are labelled in the bracket behind the type of PDF model chosen. IEM stands for Interaction-by-Exchange-with-the-Mean mixing model, CD represents Coalescence Dispersion mixing model (also called curl model), and EMST is short for Euclidean Minimum Spanning Tree mixing model. Other mixing models' full names will be used.

3.1. DJHC Burner

3.1.1. Configuration of DJHC Burner

As mentioned before, the DJHC burner is a laboratory-scale burner whose concept is similar as the design of Adelaide burner, the injected coflow has low oxygen concentration and it has a sufficiently high temperature which is above the autoignition point of the fuel to make sure MILD combustion occurs. The configuration of the DJHC burner is shown in Figure 3.1. The coflow is generated by an annulus secondary burner which is located around the main fuel jet, the diameter is 82.8 mm. This secondary burner is partially premixed according to Oldenhof[69], which is different from the Adelaide burner and allows for seeding of the flow for LDA (Laser Doppler Anemometry) measurement, while providing a stable combustion. The oxygen concentration and temperature of coflow are adjusted by a varying fuel/air ratio. The fuel pipe is cooled by air. The inner diameter of the central fuel pipe is 4.5 mm, Dutch natural gas (81,3 % CH_4, 14.2 % N_2, 3.7 % C_2H_6, and 0.6 % CO_2) is used as the fuel in most cases. Previously, Medwell declared that the addition of hydrogen in the fuel is necessary to stabilise the flame[63], the new design allows leaving out this extra fuel and thus reduces the complexity of the simulation.

Table 3.2: A summary of simulations on different jet-in hot coflow burners

Model	Reference
Adelaide burner	
RANS: Transport PDF (EMST, Modified Curl, IEM); EDC	Christo and Dally [85],2004
RANS: Conditional Momentum Closure (CMC)	Kim et al.[86],2005
RANS: EDC	Christo and Dally[41],2005
RANS: EDC	Frassoldati et al.[87],2010
RANS: EDC	Mardani et al.[88],2010
LES: Flamelet	Ihme et al.[89],2011
RANS: EDC	Aminian et al.[56],2011
RANS: EDC	Mardani et al.[90],2011
LES: three-stream flamelet/progress variable (FPV)	Ihme et al.[91],2012
RANS: EDC	Aminian et al.[81],2012
RANS:EDC	Mei et al.[92],2012
RANS: well-stirred-reactor (WSR)	Mardani et al.[94],2013
RANS: Multi-environment PDF (MEPDF) (IEM)	Dongre et al.[82],2014
RANS: Multi-environment PDF (MEPDF); Lagrangian PDF (LPDF); Presumed PDF (PPDF); (IEM, CD, EMST) EDC	De and Dongre[83],2015
RANS: EDC	Wang et al.[95],2015
RANS: EDC	Evans et al.[57],2015
RANS: extended EDC	Parente et al.[58],2016
DJHC burner	
RANS: EDC	De et al.[55],2011
RANS: FGM (IEM)	Sarras et al.[96],2012
LES: PDF	Kulkarni et al.[97],2013
RANS: Multi-environment PDF (MEPDF) (IEM)	Dongre et al.[82],2014
RANS: EDC; PDF (IEM)	Sarras et al.[84],2014
LES: Transport PDF (TPDF)	Bhaya et al.[98],2014
RANS: Multi-environment PDF (MEPDF); Lagrangian PDF (LPDF); Presumed PDF (PPDF) (IEM, CD, EMST); EDC	De and Dongre[83],2015
RANS: Conditional Source-term Estimation (CSE); EDC	Labahn et al.[99],2016
LES: Conditional Source-term Estimation (CSE)	Labahn et al.[99],2016
LES: FGM	Abtahizadeh et al.[100],2017
Vitiated coflow burner	
RANS: EDC; Transport PDF (Curl mixing model)	Cabra et al.[21],2002
RANS: PDF (M-Curl, IEM, EMST, 1-D, Well-Mixed)	Cabra et al.[76],2005
RANS: PDF (EMST mixing model)	Gordon et al.[78],2007

(a) Profile of DJHC burner   (b) Injection area
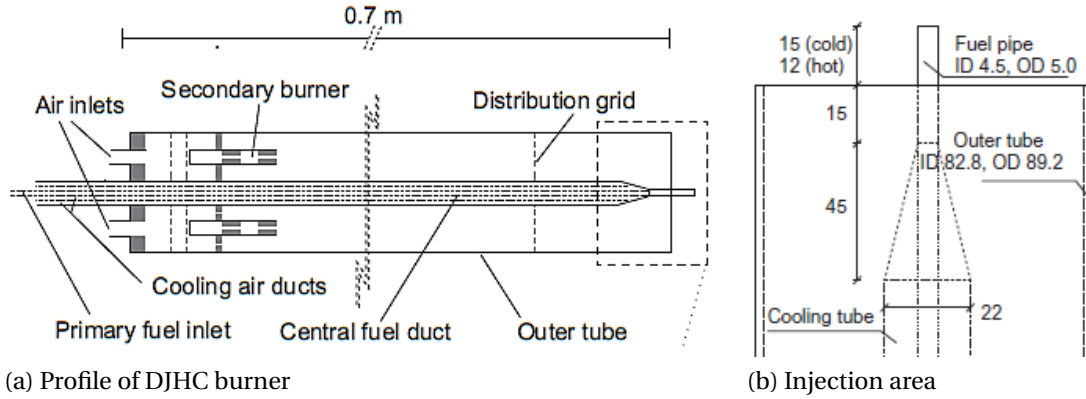
Figure 3.1: Schematic of Delft Jet-in Hot Coflow (DJHC) burner. [mm]

3.1.2. CASE DESCRIPTION

Various experiments have been made, but this thesis only focuses on the Dutch natural gas (DNG) fuel cases. Oldenhof [65, 69] applied four different settings of the secondary burner, which mainly differ in the coflow temperature and oxygen concentration. The flames are classified by coflow type. The coflow properties for different cases are shown in Table 3.3. The maximum mean temperature measured at 3 mm downstream of the jet exit is listed in the table, which is represented by T_{max}. The coflow oxygen concentration listed is mass flux-averaged based. Fuel temperature and jet Reynolds numbers vary between different cases. In this way, the influence of both coflow oxygen concentration and fuel jet Reynolds number could be investigated. The Reynolds number is calculated based on the fuel pipe diameter, the bulk velocity, and the kinematic viscosity of DNG at 300 K for the cold-coflow flames and that at 450 K for the hot-coflow flames.

Table 3.3: Properties of fuel jet and coflow in different cases

Case	Re_{jet} [-]	Fuel [nl/min]	T_{jet} [K]	Air [nl/min]	T_{max} [K]	Y_{O_2} [%]
DJHC-I	4100	16.1	430	224	1540	7.6
	8800	30.0	360	224	1540	7.6
DJHC-V	4100	15.3	380	231	1460	8.8
DJHC-X	4100	14.2	380	239	1395	10.9

3.2. SET-UP OF THE SIMULATION

3.2.1. COMPUTATIONAL DOMAIN AND GRID

Due to the symmetrical characteristic of the burner, a 2D axisymmetric grid can be adopted in RANS. The computational domain starts 3 mm downstream of the jet exit and extends

until 225 mm in the axial direction. In this case, the width of domain is set to be 80 mm in radial direction in order to take into account the entrainment of air. From experimental data, the lift-off height is around 80 mm, in different cases this value may be different[84]. To guarantee the accuracy of the simulation result, the grid around this height should be finer, while the grid around the central fuel jet should be the finest, also the shear layer region should have a finer mesh.

The four different DJHC cases are briefly listed in Table 3.3. The case DJHC-I with Reynolds number of 4100 is used as the reference state. The computational performance of 90×60, 180×125, and 360×250 cells grids in axial and radial directions are tested. The fuel injecting (axial) direction is defined as the positive x axis and the radial direction is the positive y axis in the following simulations. The temperature trends (Figure 3.2) and velocity trends (Figure 3.3) on various downstream heights in terms of different radial distance are shown below. From the figures, the trends with grid refinement are similar. The main differences are around peak temperature area while velocity shows limited difference. It is obvious that 90×60 grid cannot capture the peak temperature, while the difference between 180×125 grid and 360×250 grid is acceptable. However, the peak temperature predicted by 180×125 grid is not smooth enough, which implies that a refinement around this area should be applied. Finally, a 190×145 grid is chosen (26508 cells).

(a) x=15mm   (b) x=30mm   (c) x=60mm
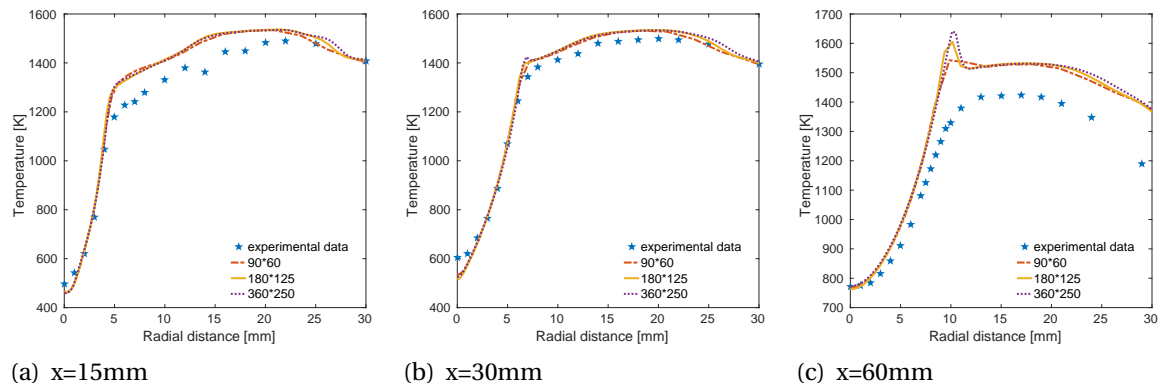
Figure 3.2: Grid effect on temperature

Fig. 3.4 shows the grid used in the end, the x and y axis are marked. From the figure, it is clearly that along the radial direction, fuel jet part has the finest mesh. The enlarged view of the refinement around the lift off height position is shown in the right-bottom corner of the figure, while the finer mesh for the peak temperature prediction is also marked with a dash-line box.

(a) x=15mm   (b) x=30mm   (c) x=60mm
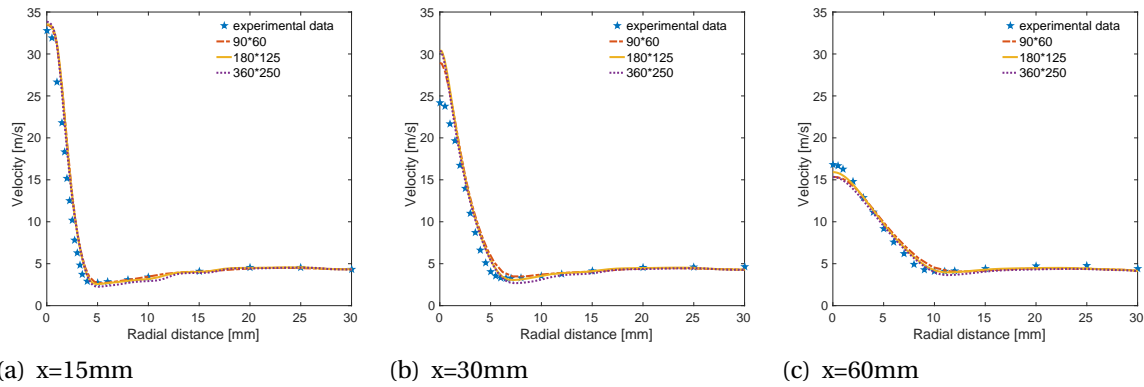
Figure 3.3: Grid effect on velocity
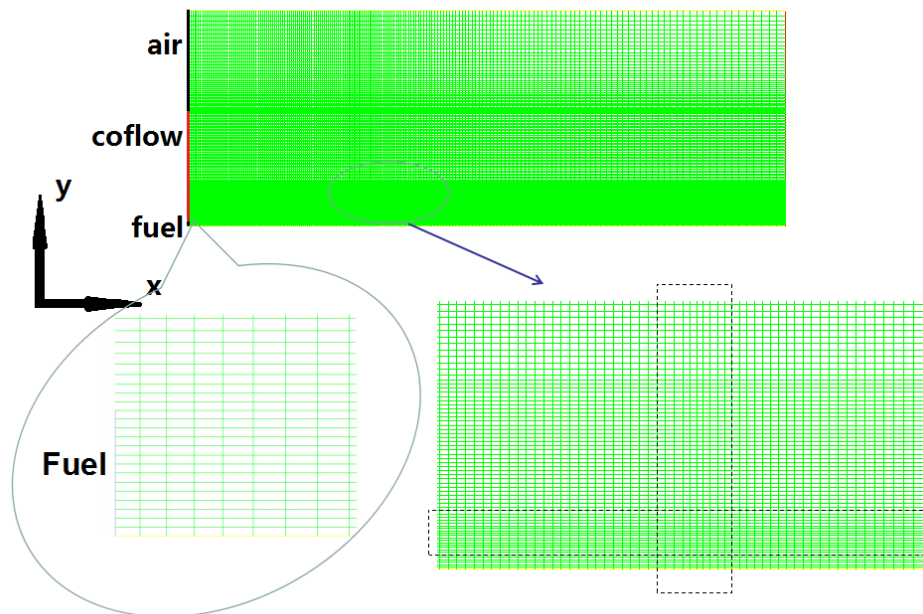
Figure 3.4: Grid used for simulation

3.2.2. BOUNDARY CONDITIONS

The inlet boundary conditions of both fuel jet and coflow are set in agreement with the experimental data measured at 3 mm downstream of injector. The species at the coflow are calculated by the measured temperature and oxygen profile under the hypothesis of equilibrium combustion. In the case of Adelaide burner, the simulation result, jet spreading and decay rates, has been found to be very sensitive to the turbulence level at the inlet[41], especially the fuel inlet turbulence quantities. In this case, the inlet boundary conditions, turbulence kinetic energy k and dissipation rate ϵ, are calculated based on the experimen-

tal data. The turbulence kinetic energy is related to normal Reynolds stresses:

$$k = \frac{1}{2}(\widetilde{u''u''}^2 + \widetilde{v''v''}^2 + \widetilde{w''w''}^2) \tag{3.1}$$

where $\widetilde{u''u''}$ and $\widetilde{v''v''}$ are the axial Reynolds stress and radial Reynolds stress, respectively, while $\widetilde{w''w''}$ is the azimuthal component of Reynolds stress.

Following Sarras et al.[84], the energy dissipation rate is derived from the equation below:

$$\epsilon = \widetilde{u''v''}\frac{\partial \widetilde{U}}{\partial y} \tag{3.2}$$

where $\widetilde{u''v''}$ is the Reynolds shear stress and $\widetilde{U}$ is the mean axial velocity.

The symmetric $y = 0$ is set as axis. Instead of a symmetry boundary condition, the boundary at $y = 80$ mm is considered to be a slip wall[99], where a zero-shear stress condition is imposed[56]. In symmetry boundary condition, all flux quantities across the boundary are zero, which means the normal gradients of all flow variables are zero and also the normal velocity is zero, while flux quantities along the boundary could exist. According to Eq. (2.22), in Reynolds shear stress $\overline{\rho}\widetilde{u''v''}$, the term $\partial\widetilde{u}/\partial y$ is zero, $\partial\widetilde{v}/\partial x$ could be non-zero, the Reynolds shear stress could be thus non-zero. Besides, the zero-shear stress slip wall allows heat flux across the boundary, while in the symmetry case no heat flux across the boundary exists. The zero-shear stress wall boundary is a better choice.

Finally, the outflow outlet boundary condition is adopted. The profile of temperature, velocity, and turbulence kinetic energy applied for the boundary is shown in Fig. 3.5.

(a) Turbulence kinetic energy   (b) Temperature   (c) Velocity
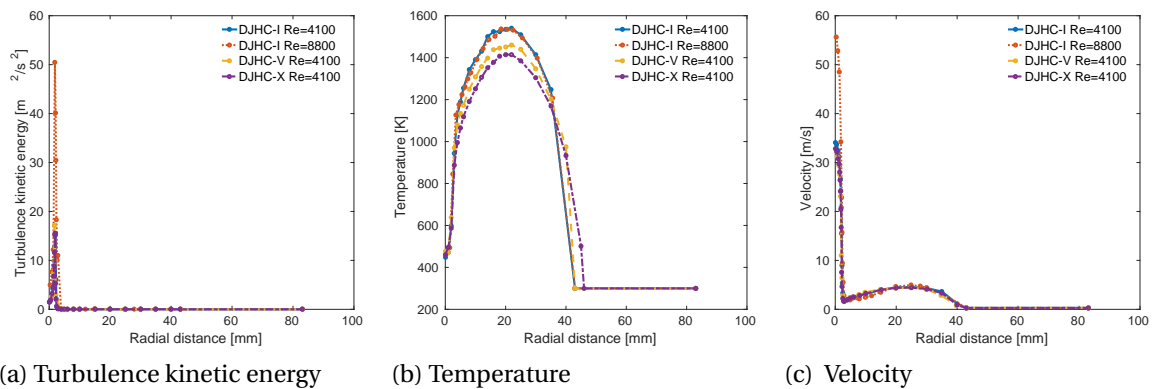
Figure 3.5: Inlet boundary conditions

The inlet velocity of the air is set to 0.3 m/s in order to avoid the unphysical solution while in the experiments the air is static.

3.3. PRELIMINARY TESTING: INFLUENCE OF TURBULENCE MODEL

It is well-known that the standard $k - \epsilon$ model over-predicts the spreading and decay rate of a cylindrical jet due to its isotropic assumption. As is mentioned previously, the widely used modified k-ϵ model constant proposed by Dally et al.[80] (adjust the model constant $C_{\epsilon 1}$ from 1.44 to 1.6) is found to be not suitable for DJHC flame; this is not shown for brevity. De et al.[55] proposed that the realizable k-ϵ fit the DJHC burner best among different k-ϵ models. Sarras et al.[84] used a RSM and also found good agreement. However, the comparison between realizable k-ϵ and RSM has not been mentioned in the existing articles. For this reason, a preliminary testing of different turbulence models' effect is taken in this thesis. The figures (Figure 3.8, Figure 3.7 and Figure 3.6) shown in this section are results of the combination of different turbulence models' result with the standard EDC model. Only the representative figures are shown for brevity.

(a) x=15mm   (b) x=60mm   (c) x=120mm
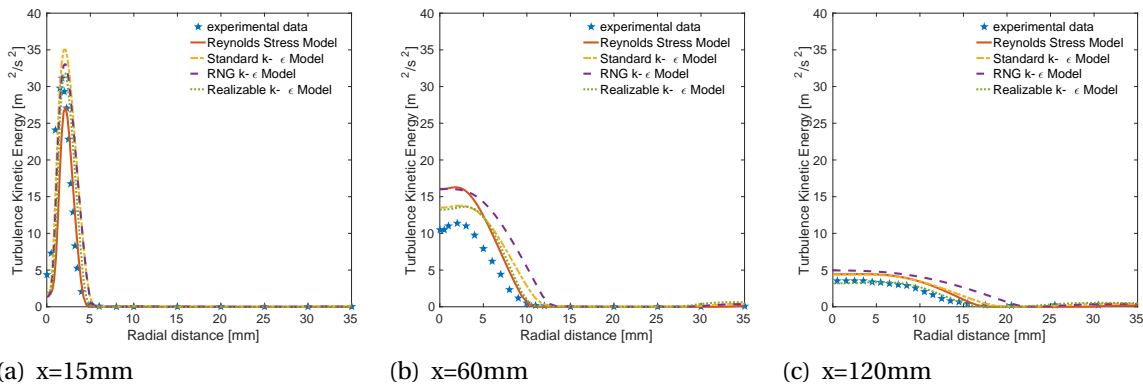
Figure 3.6: Model effect on turbulence kinetic energy

(a) x=15mm   (b) x=60mm   (c) x=120mm
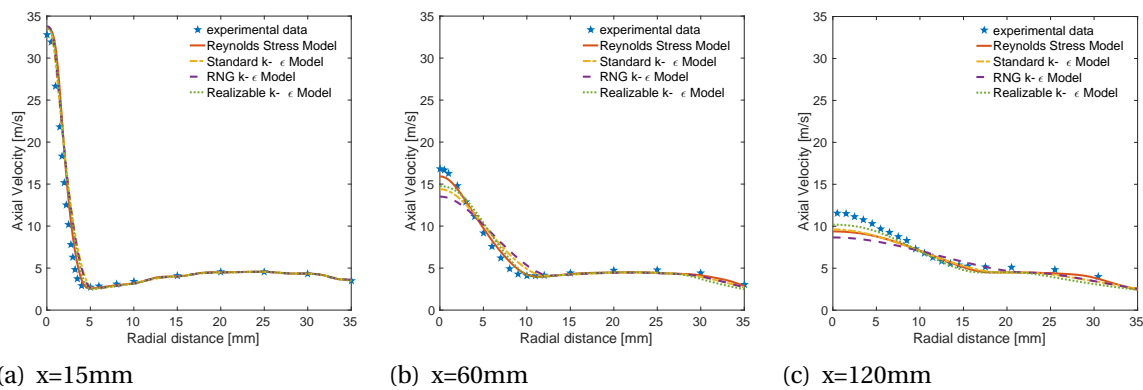
Figure 3.7: Turbulence model effect on velocity

The performance of different turbulence models can be evaluated in three regions: the near centreline fuel spreading region, the near air mixing region and the peak temperature
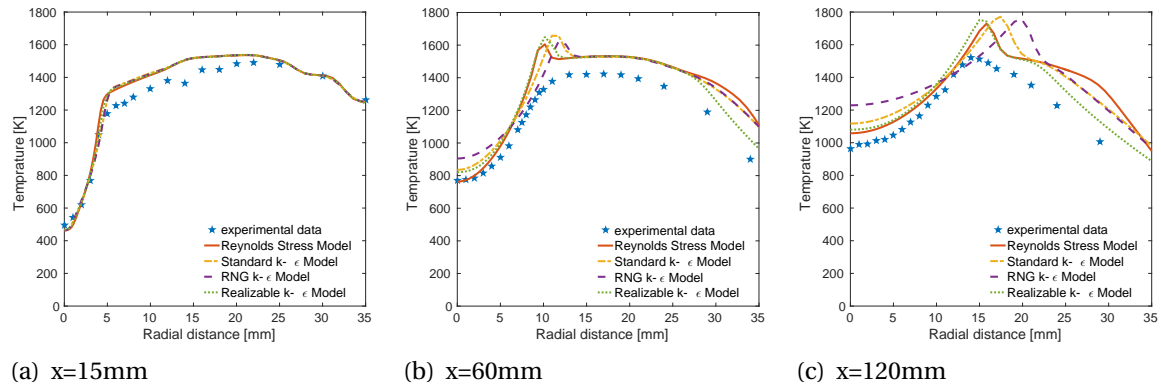
Figure 3.8: Turbulence model effect on temperature

region. Costa-Party and Mydlarski [101] pointed out that the kinetic energy dominates the development of mixing layer in a free shear flow, which would influence the velocity and the combustion process. The turbulence kinetic energy is thus analysed first, followed by the velocity and temperature curves. The detailed analyse is listed below:

1. The near centreline fuel spreading region ($y < 5$ mm):

   For turbulence kinetic energy, all the k-ϵ models show a trend of over-estimation. The RNG k-ϵ model over-predicts most, while the over-prediction of realizable k-ϵ model is the least, especially in the further downstream area. The Reynolds Stress Model under-predicts the peak at 15 mm, and over-predicts further downstream. The velocity predictions show similar trend. The decay of fuel jet velocity predicted by RSM is in good agreement with the experiment until 90 mm, and the realizable k-ϵ model can give a better prediction in further downstream, which is similar with the turbulence kinetic energy prediction. Again, the RNG k-ϵ model gives the worst result. For temperature prediction, all the turbulence models tested can give good agreement in the near centreline spreading region until 30 mm, the over-prediction of RNG k-ϵ model is significant afterwards. Different from the turbulence kinetic energy and velocity predictions, the advantage brought by realizable k-ϵ model in downstream area compared to RSM is not found.

2. The near air mixing region ($y > 25$ mm):

   In this region, the RSM shows best in prediction of the turbulence kinetic energy. The over-prediction of the realizable k-ϵ model is the largest. This is also found in the velocity prediction, RSM shows the best agreement with the experimental result while the prediction of realizable k-ϵ has the largest error. The performance of other models are in between.

3. The peak temperature region ($10 < y < 20$ mm):

   The peak temperature occurs due to the mixing of fuel and oxidizer, where the mean stoichiometric condition is found and ignition takes place. It is obvious that in this region, the realizable k-ϵ model and RSM give comparable good agreement in terms of turbulent kinetic energy, while other turbulence models overestimate the value a lot. Similar trend is found in velocity prediction. For the temperature curve, the peak temperature is found to not change with different turbulence models used, which is corresponding to Aminian et al.'s statement[81], only RSM can slightly lower the peak temperature. However, the position of peak along the radial direction is indeed influenced by the turbulence model used, which is influenced by the turbulence kinetic energy predicted. The RSM and the realizable k-ϵ model have significant advantage in this sense.

To conclude, the performance of realizable k-ϵ model and RSM are significantly better than other turbulence models. Both of them can predict a good peak temperature position compared to other turbulence models. In the near centreline spreading region, the RSM performs better in upstream area while the realizable k-ϵ model shows a better agreement in the downstream. However, the RSM is definitely better in terms of the mixing between the air and coflow. Finally, RSM is chosen as the turbulence model used in the following simulations.

The preliminary testing results are in agreement with the previous research. From figures, the better model in terms of kinetic energy in shear layer gives a better velocity prediction in the corresponding regime. This supports the statement of Costa-Party and Mydlarski [101] mentioned before. They also declared that different from a channel flow, the turbulence kinetic energy is largest in the core of the jet rather than at the boundaries in a jet, and the jet kinetic energy should be decaying, which is also observed in the simulation.

The modified standard k-ϵ model has been demonstrated by researchers to be not appropriate for DJHC burners as mentioned. RNG $k - \epsilon$ model is also not a good choice according to the previous work[41, 55, 87, 102] though the model is supposed to improve the prediction of round jet by applying an additional term in the dissipation rate equation together with a consideration of the swirl effect and varying Prandtl number. It seems the RNG $k - \epsilon$ model constrains the decay of fuel jet and over-predicts the turbulence kinetic energy a lot compared to other models.The velocity field predicted is thus the worst which leads to a unsatisfactory temperature profile. The better agreement given by realizable $k - \epsilon$ model and RSM are understandable. The realizable $k - \epsilon$ model improves the simulation by taking into account the rotation rate effect on turbulent viscosity, while the RSM better describes the turbulence anisotropic by solving additional transportation equations for the Reynolds stresses. The Reynolds stresses input at the boundary also elevates the accuracy

of RSM prediction.

3.4. Application of the Extended EDC model: Results and Discussion

From Fig. 3.6, 3.7, 3.8 shown before, the standard EDC model shows a trend of over-predicting the temperature and this cannot be eliminated by the choice of different turbulence models. This is also found by previous researchers. Christo and Dally[41] declare this is due to the localized extinction and re-ignition which could not be simulated by the EDC model. Aminian et al. conclude that EDC model itself tends to slightly over-estimate the temperature in the case of highly diluted and preheated combustion[56]. This may arise from the different conditions from those for which the EDC model is derived. As is mentioned in Chapter 2, EDC assumes fast chemical reaction, the flow-governed reactants would start to react as soon as they are mixed with each other, which requires $Da \gg 1$. However, the Damköhler number of MILD combustion is found to be near unity in the reaction region[103], which means the influence of turbulence and chemistry are comparable. From the temperature prediction of standard EDC model shown before (Figure 3.8), in DJHC burner, the over-prediction of temperature is more likely to appear in the mixing layer. Schütz et al.[104] demonstrate that MILD combustion is strongly dominated by turbulent mixing, chemical reactions are strongly delayed because of non-equilibrium effects, even for high preheating temperatures. They analyse the velocity field under MILD combustion and find the incompletely mixed oxidizer and fuel strongly reduce the velocity magnitude. In the beginning, the enhancement of entrainment is said to " destroy the normal chemical reaction mechanism"[105, 106].

It is demonstrated that MILD combustion is homogeneously distributed by analysing the OH fields [61, 107]. The distributed characteristic leads to a reduction of both temperature and species gradients, which would supply lower driving force of mass transport[81]. De et al.[55] point out the influence of turbulence scale on EDC model performance, they believe standard EDC is only valid under larger turbulence scale (large Damköhler number). Besides, they notice that in DJHC burner cases, the standard EDC model performs poor where the turbulent Reynolds number Re_T is lower than 65. Evans et al.[57] tried to analyse the influence of EDC fine structure constant expression through the partial derivative of the reaction rate, and demonstrate that C_γ is a monotonically decreasing function of the ratio $k^2/(v\epsilon)$, which is proportional to the turbulent Reynolds number $Re_T (= v\epsilon/k^2)$.

From these articles, it is clear that the performance of EDC model is highly influenced by the Damköhler number and turbulent Reynolds number. The extended EDC model in the following sections therefore aims to quantitatively define the model constants with re-

gard to local flow properties, in order to obtain better performance.

3.4.1. VALIDATION OF THE EXTENDED EDC MODEL

In this section, the performance of the extended EDC model is evaluated by investigation of the DJHC-I flame, at a Reynolds number of 4100. This case can be chosen as the reference state according to the four cases described in Table 3.3. The most widely used method, global model constant adjustment (the residence time scale constant is modified from 0.4083 to 3), will also be shown in order to make a comparison. To be clear, the new extended EDC model is called "local modified model constants method".

3.4.1.1. PREDICTION OF TEMPERATURE

One of the large differences between MILD combustion and conventional combustion is the distributed reaction zone, which leads to a homogeneous temperature field. The prediction of temperature is thus essential and becomes an important issue to evaluate the model performance. As is mentioned before, original EDC model fails to capture the temperature peak correctly, the aim of the extended EDC model is to possibly eliminate the over-prediction of temperature. The difference temperature estimation of standard EDC model, the new extended EDC model and global modified EDC model are shown in Fig. 3.9.

It can be seen that using the extended EDC model, the over-predicted temperature peak is reduced significantly compared to both the standard EDC model and the globally modified residence time constant method. In the standard EDC model, the accuracy of temperature prediction seems to be worse in the further downstream area, the extended EDC model is observed to give better temperature profile in high diluted regime, and performs better than the global modified method. To be more detailed, take 120 mm as an example, the peak temperature predicted by original EDC model and local modified constant method are 1749K and 1584K, respectively, while the experimental result is 1521K. As a contrast, the new local modified method gives a prediction of 1526 K, which is much closer to the experiment. It should be pointed out that in all the three methods, the peak temperature appears farther from the central fuel jet compared to the experiment. The improvement of temperature reduction given by extended EDC model is significant. Besides, the prediction given by the extended model also shows better agreement in the area between the central fuel jet and the mixing layer, while the coflow temperature at the air side shows limited difference compared to other two models. It is noticed that the extent of coflow temperature over-prediction is larger than that of central part (from centreline to the peak), the reason needs to be identified.

The coflow temperature changing tendency along the stream direction in experiment and simulation show interesting difference. Generally, the coflow temperature is consid-
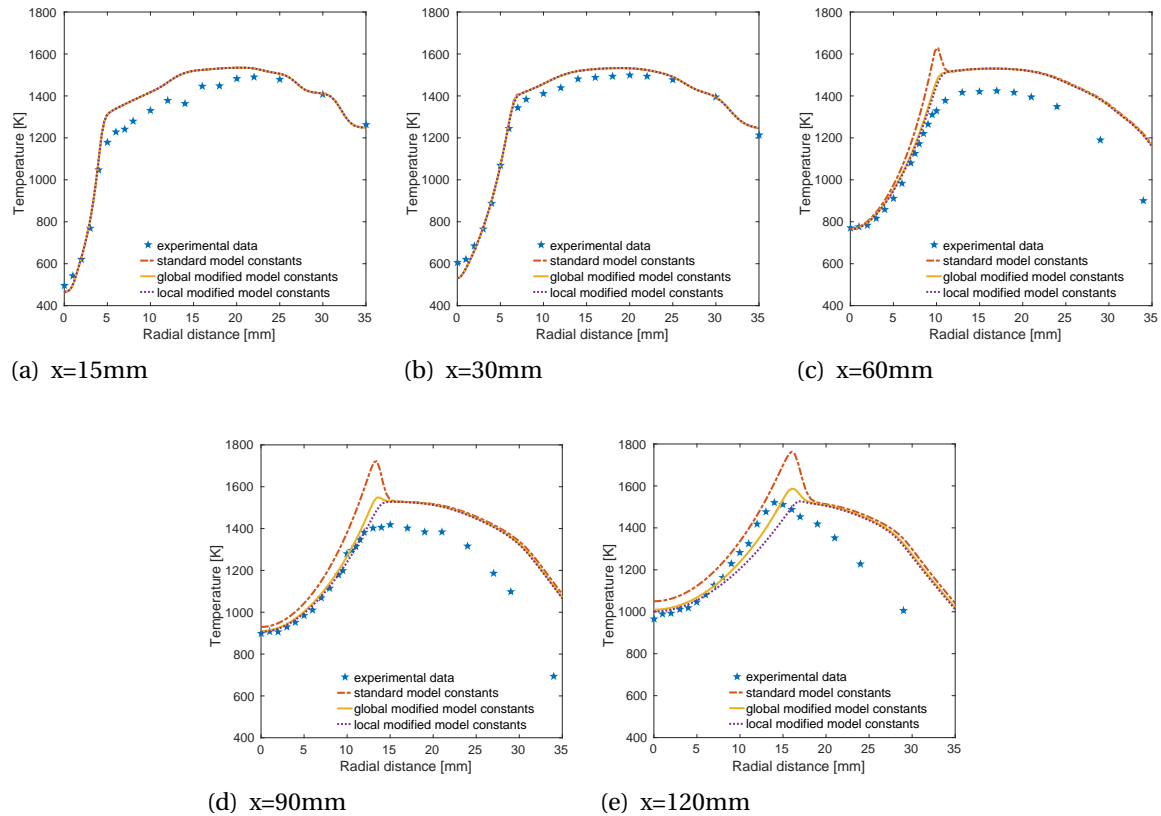
Figure 3.9: Prediction of temperature

ered to be influenced more by the air entrainment, as combustion does not exist in this area, no temperature rise should be observed in this area, and the heat loss may cause slightly temperature reduction, similar trend is found in simulation, the coflow prediction is relatively stable. The coflow temperature does not change significantly until 60 mm downstream, while a slight decrease in the regime away from central area is observed further downstream, this is caused by the air entrainment, the mixing effect is larger in the downstream area, which will be described later. However, the experimental coflow temperature shows an oscillation. Starting from the inlet temperature, the temperature of the coflow decreases until 15mm downstream, then goes up from 15 mm to 30 mm, and drops again from 30 mm to 60 mm, followed by a further temperature reduction caused by the entrained ambient air. Similarly, the entrainment of hot coflow leads to a continuous temperature rise of the fuel jet, which is found in both experiment and simulation. The unexpected temperature oscillation of the coflow needs further investigation.

The improvement of the new extended EDC model compared to Parente's extended EDC model is shown by Fig. 3.10.

As is mentioned in subsubsection 2.5.2.2, Parente's extended EDC model is a qualitative model which needs to be elaborated for different equipments. Each of the model constants

(a) x=60mm   (b) x=90mm   (c) x=120mm
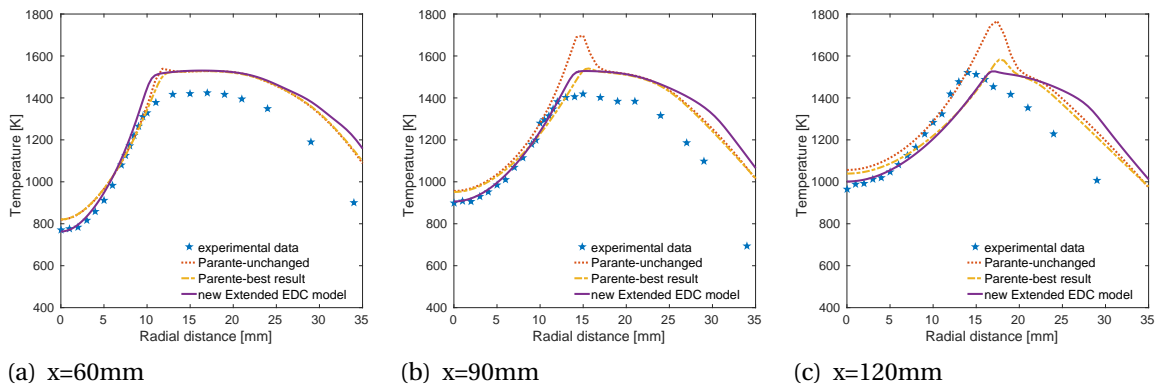
Figure 3.10: A comparison between Parente's extended EDC model and the new extended EDC model

is proportional to an expression, the constants for the equations need to be found. In Fig. 3.10, the original unchanged model constants and final modified constant based on Parente's extended EDC model are both shown to be compared with the new extended EDC model.

It is clear that the temperature prediction in the near centreline fuel spreading region given by the new extended EDC model is better. The peak temperature value is reduced significantly. Also taking into account that calibration is not needed, the improvement is obvious in terms of computational cost.

3.4.1.2. PREDICTION OF FLOW

As is mentioned before, turbulence kinetic energy expresses the formation of the turbulent mixing layer and influences the combustion process. The predictions by different models are shown below. Only the downstream highly diluted area ($x > 60$ mm) results, which are the most relevant, are shown in Fig. 3.11 for brevity. The axial velocity is also depicted (Fig. 3.12).

(a) x=60mm   (b) x=90mm   (c) x=120mm
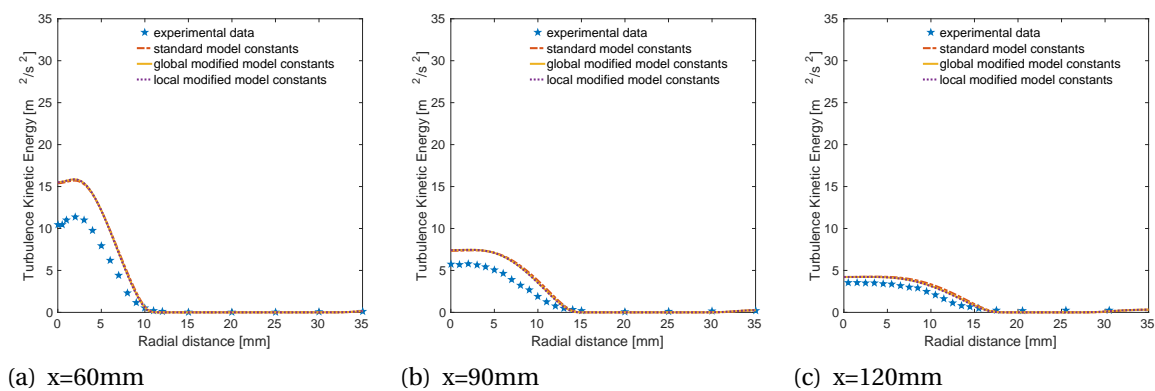
Figure 3.11: Prediction of turbulence kinetic energy

(a) x=60mm   (b) x=90mm   (c) x=120mm
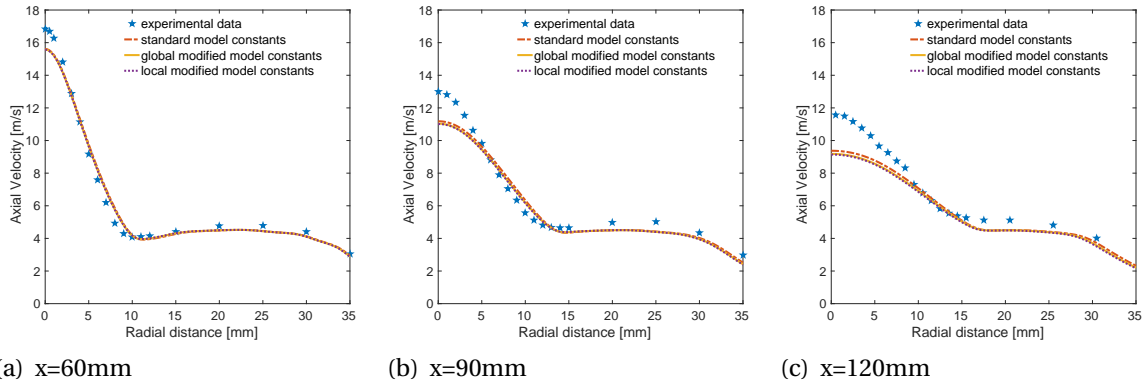
Figure 3.12: Prediction of axial velocity

From figures, it is confirmed that the fluid motion is not influenced much by different EDC models, this corresponds to the fact that the flow and turbulence model equations are influenced by the chemistry via the mean density only. With regard to turbulence kinetic energy, the predictions show limited difference. Only the original EDC model shows a slightly larger mixing at the height of 120mm compared to the other two models. The global modification method and the extended EDC model have almost same outcome. Similar trends could also be found from other flow properties, including velocity and Reynolds Stresses. Only the axial velocity is shown here for brevity. The predictions of all models show agreement with the mean velocity and turbulence kinetic energy measured, especially the upstream area (until 90 mm). The decay of fuel jet velocity is slightly overestimated. This implies that the extended EDC model influences the temperature prediction mainly directly via the chemical source term.

3.4.1.3. EFFECT OF THE EXTENDED EDC MODEL

The extended EDC model involves changing the model constants locally through local turbulent Reynolds number and Damköhler number. The two flow properties Da^* and Re_T are shown in Fig. 3.13 and 3.14. $Da^* = \tau_k/\tau_c^*$ as described in Chapter 2, $Re_T = \nu\epsilon/k^2$ is calculated. The horizontal direction is the stream direction, and the lower boundary is the centreline of the fuel jet.

According to Fig. 3.13, the Damköhler number is lower than 8 in almost all location, the only exception is found in the coflow stream close to the inlet, because the changing is assumed to be in-equilibrium This confirms that in MILD combustion the Damköhler number is much lower than in conventional combustion. Combined with the temperature distribution shown in Figure 3.15, for the peak temperature area where most chemical reaction takes place, the Damköhler number is found to be even lower.

The turbulent Reynolds number is found to be higher in the fuel jet regime. This is understandable because the fuel jet has a larger velocity. De et al.[55] showed that for DJHC
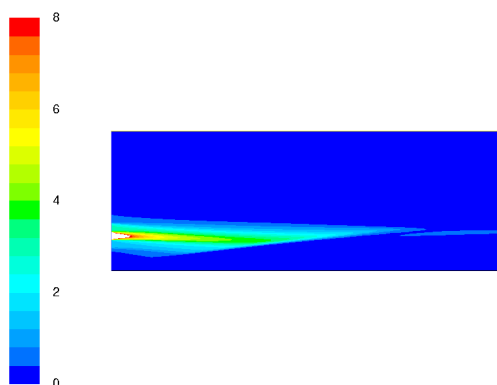
Figure 3.13: Characteristic Da^* distribution
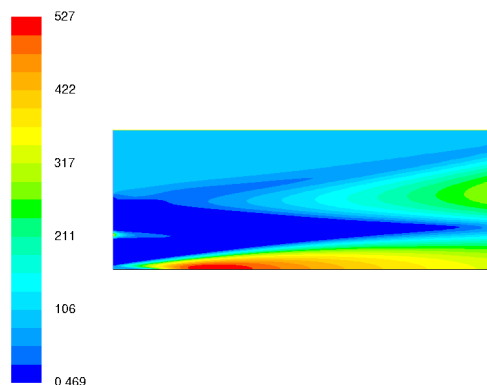
Figure 3.14: Characteristic Re_T distribution
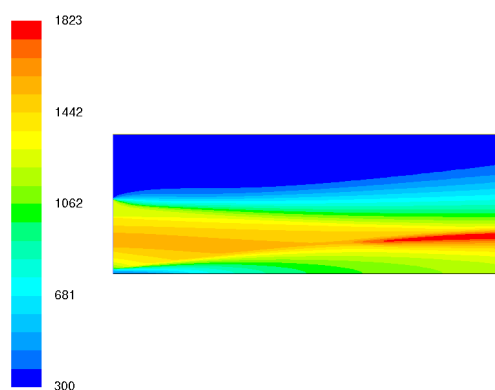
Figure 3.15: Temperature (K) field

burner, when Re_T is lower than a critical value 65, the standard EDC model needs to be improved. As the extended EDC model is related to the local turbulent Reynolds number, the problem caused by low Re_T could be avoided. A significant reduction of peak temperature compared to the standard EDC model could be obtained through the new extended EDC model, whereas the local Re_T is lower than 65.

As is described before, the model constants are related to local turbulent Reynolds number and Damköhler number, which influences the predicted temperature. The flow property based local modified model constants are shown in the following figure.

It can be seen that the model constants C_γ and C_τ are modified locally. The model has strong effect in the mixing layer, this is also the area where near unity Da number and Re_T number lower than 65 are found. The fine structure volume constant C_γ becomes smaller, and the residence time constant C_τ increases. The homogeneous reaction zone is better captured with the new model constants, and a more homogeneous temperature field could be obtained. The model constants seem to be highly correlated to the dilution level.

(a) Modified C_γ (b) Modified C_τ
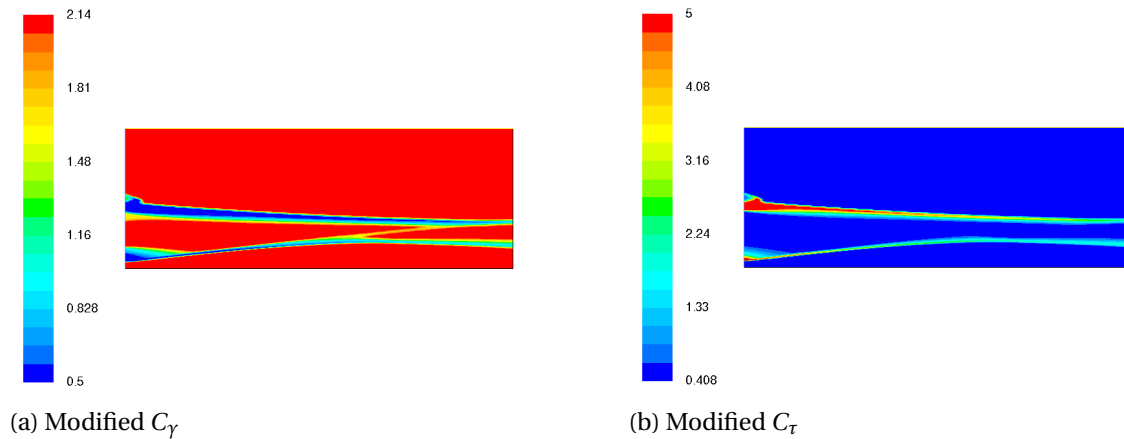
Figure 3.16: Modified model constants

3.4.1.4. PREDICTION OF LIFTOFF HEIGHT

The liftoff properties of flames have been investigated a lot in both experiments and modellings. The liftoff mechanisms of both premixed and non-premixed flames have been elucidated for the so-called "vitiated coflow" burner (as is listed in 3.1), while other JHC studies mainly focused on the issue of what influences liftoff heights in MILD combustion. Various definitions of liftoff height were proposed by different researchers. Cabra et al. simply defined the liftoff height as the lowest height where visible chemiluminescence could be observed[76], while Oldenhof et al.[69] used the possibility of detected flame pockets to define the liftoff height. Differently, Gordon et al.[78] take the distance to where the steepest axial OH gradient occurs as the liftoff height. Besides, the liftoff height can also be determined based on concentrations of C_2H_2 and C_2H_4[76]. Generally, the OH mass fraction can be used as a typical marker of the liftoff heights as the OH peak is present in the stabilized region of autoigniting flames while it is not discernible in the pre-ignition regime[77]. Similarly, Medwell et al.[62] proposed that liftoff height corresponds to a transition of weak to strong OH levels. In simulations, the liftoff distance could be seen as the earliest (along the axial direction) strongest OH concentrations position found in a flame[21]. In the DJHC burner, only the first half of the flame is MILD flame, while the upper part of the flame regime is more like conventional combustion. In this case, the liftoff height should be considered as the earliest strongest OH level in the MILD regime. More precisely, the regime is up to approximately 120 mm downstream. Experimentally, Oldenhof et al.[71] examined the OH distribution in a regime from 40 mm downstream of the jet exit to 114 mm downstream. In this thesis, a simulation of OH species in the same area is considered.

The figure below (Figure 3.17) compares the simulation result with the experiment. The inflow boundaries are set based on the experiment. The left half of the figure is the simulation result, which is OH mass fraction, and the right half shows the experimental result

of OH-PLIF (Planar Laser Induced Fluorescence), which is rescaled to values in the range of 0 to 255 as the OH data is not quantitative. For ease of interpretation, the figures are depicting the same spatial domain symmetrically.
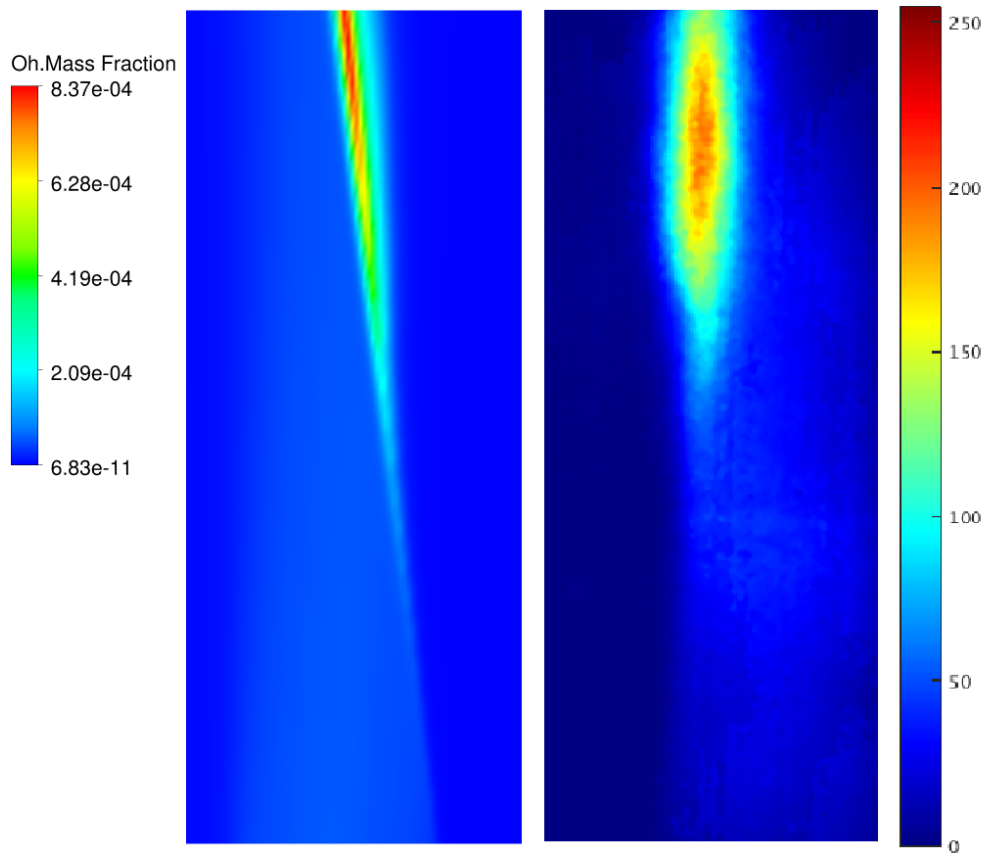
Figure 3.17: Experimental and predicted OH distribution of DJHC-I Re_{jet} = 4100 flame

From the figures, it is clear that the so called "early ignition" is avoided. The simulated OH concentration starts to rise almost at the same height in model and in experiment, which is about 90 mm away from the fuel exit. By defining the liftoff height in terms of visibility of flame, for DJHC-I Reynolds number 4100 case, the flame structures develop from 80 mm[69] and already appear frequently at 90 mm height[65]. This could also be seen in the OH concentration based definition of liftoff height. The relatively strong OH concentration (labelled by green colour, which is about 3/4 of the largest OH concentration) can be observed in both experiment and simulation at the same height. The spreading of flame front seems to be modelled properly, the peak OH concentration positions along the radial direction on the highest boundary of the domain are also similar. The outer part (along the radius direction) has a larger OH concentration compared to the inner area, this is also captured by the simulation.

In conclusion, the OH field seems well-predicted by the extended EDC model. The early ignition is avoided, which is corresponding to the observation of temperature prediction.

Gordon et al.[78]proposed that using OH concentration to define liftoff height could lead to about four jet diameters difference compared to that of visibility observation, in DJHC-I case, this difference is less than two jet nozzle diameters (10 mm), which supports Gordons' proposal.

3.4.2. INFLUENCING FACTORS

In this section, several factors influencing DJHC burner MILD combustion are considered, including fuel jet velocity, coflow temperature, coflow oxygen level, and other possible effecting factors. The influence will be evaluated by looking at the effect on temperature, liftoff height, and flame volume. All simulations are done with new extended EDC model.

3.4.2.1. INFLUENCE ON FLAME VOLUME

Mei et al.[92] proposed a new computational method of evaluating the flame volume. The carbon monoxide (CO species) is chosen to be the marker of flame volume as it is the last intermediate product[108]. They declared that the 0.01 contour of the near-zero ratio (the local CO molar fraction X_{CO} divided by the maximum value over the whole computation domain X_{COmax}) is appropriate to mark the boundary of reaction zone:

$$R_{CO} = \frac{X_{CO}}{X_{COmax}} = 0.01 \tag{3.3}$$

The maximum length (L) and width (W) of the zone enclosed by the near-zero ratio boundary are defined as the flame length and flame width, respectively. The flame volume could thus be calculated as:

$$V = \frac{\pi}{6}LW^2 \tag{3.4}$$

The four cases in Table 3.3 are simulated, the results are shown below. According to Yang et al.[67], chemical flame length and flame volume are related to the coflow oxygen concentration and the temperature of fuel jet and coflow. In DJHC flames, the temperature and oxygen concentration of coflow are always changing in opposite direction, from case I to case V, the coflow temperature keeps decreasing while the oxygen concentration remains rising. Consider the two different DJHC-I cases, the coflow fuel jet velocity and temperature are different while the coflow condition remains the same.

According to Mei et al.[92], an increment of jet velocity leads to a decrease of flame thickness while the flame length remains almost unchanged. From 4100 Reynolds number case to 8800 Reynolds number case, the jet velocity increases, from Fig. 3.18, the flame length remains, which corresponds to Mei et al.'s theory, but the width of the flame is increasing instead of decreasing. This is due to the fuel temperature changes from 430 K to 360 K, the enlargement of flame volume conforms to the previous finding[67]. It seems that
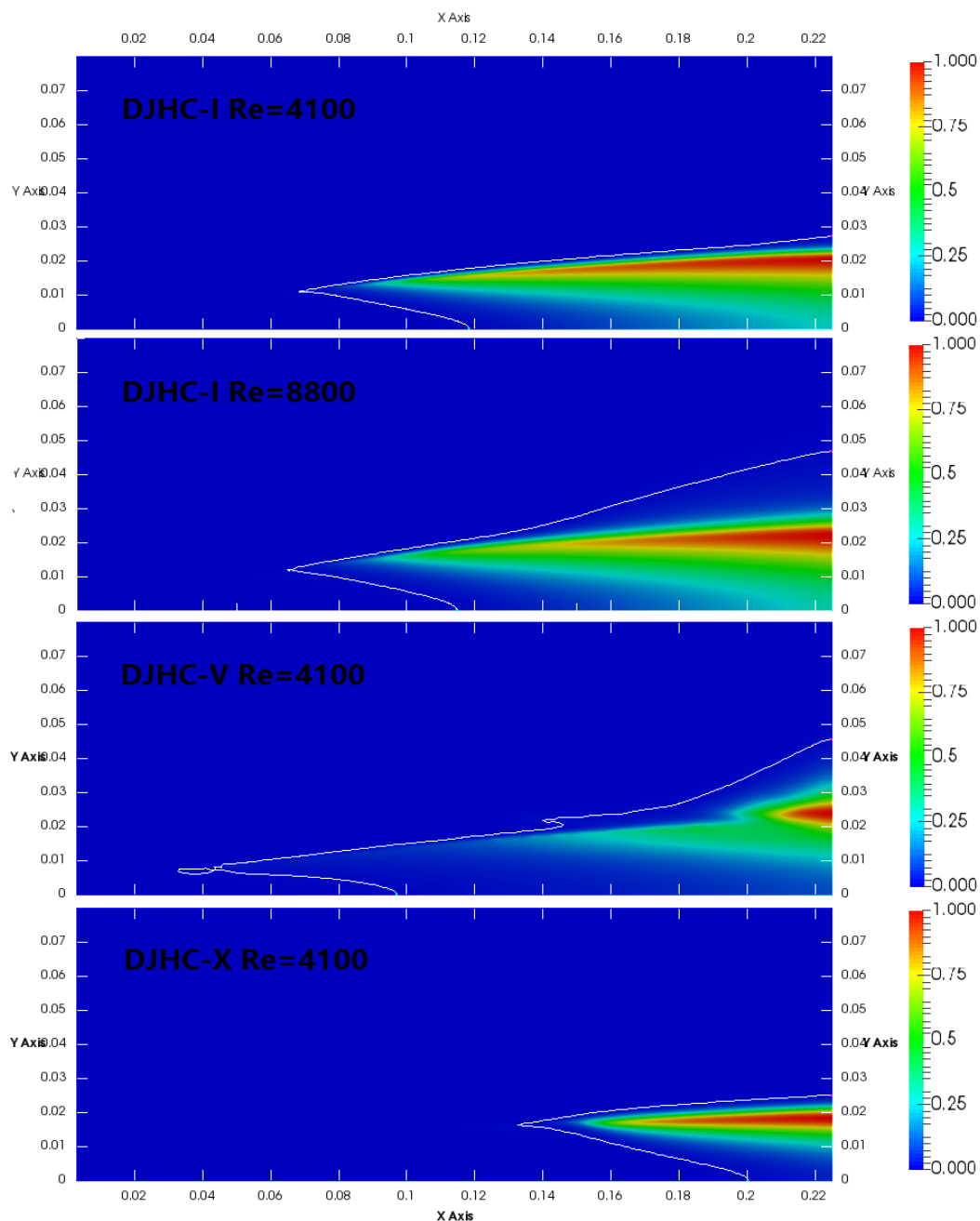
Figure 3.18: Prediction of flame volume (CO ratio with contour 0.01 in white)

the influence of fuel temperature is larger than jet velocity.

The influence of coflow conditions could be concluded from case V and X, since the jet properties in these two cases are kept the same. The coflow temperature and oxygen concentration are bidirectionally coupled, from simulation results (Figure 3.18) both the flame length and flame width reduce as the coflow temperature decreases, while the oxygen concentration increases. The flame volume changing trend is the same with flame length in this case.

The influence of fuel condition and coflow condition can be evaluated by case I Re=4500 and case V. The fuel jet temperature reduces by 13.16%, while the mean coflow temperature decreases 5.16%. The change of fuel jet contributes to the increment of flame length and width while the change of coflow shows different effect. From the figure, it is clear that both the flame length and the flame width increase. The flame width increases 66.7%, and the flame length increase 22.2%. This illustrates that the effect of fuel jet temperature is more significant compared to the coflow temperature.

3.4.2.2. INFLUENCE ON LIFTOFF HEIGHT

The fuel jet velocity is found to be important for flame stabilization. According to Medwell et al.[62], the liftoff height is very sensitive to fuel jet velocity. The OH prediction of the DJHC-I Re=8800 case is shown in Fig. 3.19. The computational domain is the same as in previous simulations. The liftoff distance is compared to what is found in Fig. 3.17 in order to find the influence of jet velocity on liftoff height, as the significant difference between these two cases is the jet Reynolds number. The defined liftoff height position based on the simulation in Fig. 3.17 has an OH concentration magnitude of around 4×10^{-4}, which is in green colour. The same order of magnitude is found to be labelled by blueish colour in Re=8800 case. The simulated liftoff height is around 70 mm, which is 20 mm lower than that of Re=4100 case. Again, the predicted liftoff height is found to be corresponding to the green colour shown in experimental result, which corresponds to the region of rapid change from low to high OH^* concentration. The liftoff height is found to be decreasing as the jet velocity increases, which agrees with the results given by Oldenhof et al.[65] and De et al.[55]. This is understandable as a higher jet velocity could enhance the hot oxidiser entrainment, thus the reaction occurs earlier. The influence of coflow temperature and oxygen concentration level on liftoff distance is demonstrated to be inverse. Gupta et al.[14] noticed a decrease of flame standoff distance as the temperature of oxidizer is increased, while Lille et al.[15] pointed out that the reduced oxygen concentration increases the liftoff distance as the dilution level is increased. As in the experiments of DJHC burner, a reduced coflow temperature is always couple with an increased oxygen level, the effects of the two issues cannot be fully specified, only the couple effect can be studied.

Considering the DJHC-X case, the liftoff height is found to be exceeding 150 mm in experiment, which is outside the measured domain of OH[65]. Fig. 3.20 shows the predicted OH concentration of DJHC-X flame, the whole computational domain is shown rather than just analysing the experimental region.

From Fig. 3.20, the order of magnitude 4×10^{-4} is found until 145 mm, the liftoff height is thus defined as 145 mm, this result is very close to the experiment by Oldenhof et al.[65], only slightly early ignition is found. The change of liftoff height shows that a decrease of coflow temperature would bring an increase of liftoff height in this case. To be more de-
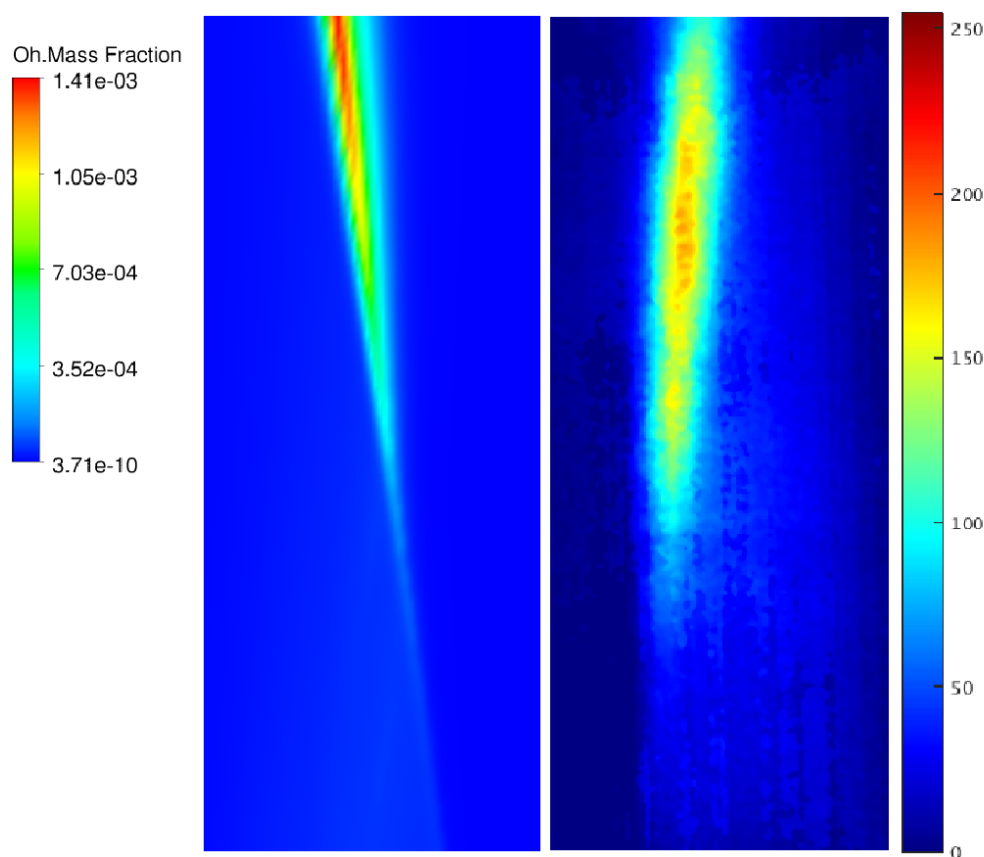
Figure 3.19: Experimental and predicted OH distribution of DJHC-I $Re_{jet} = 8800$ flame
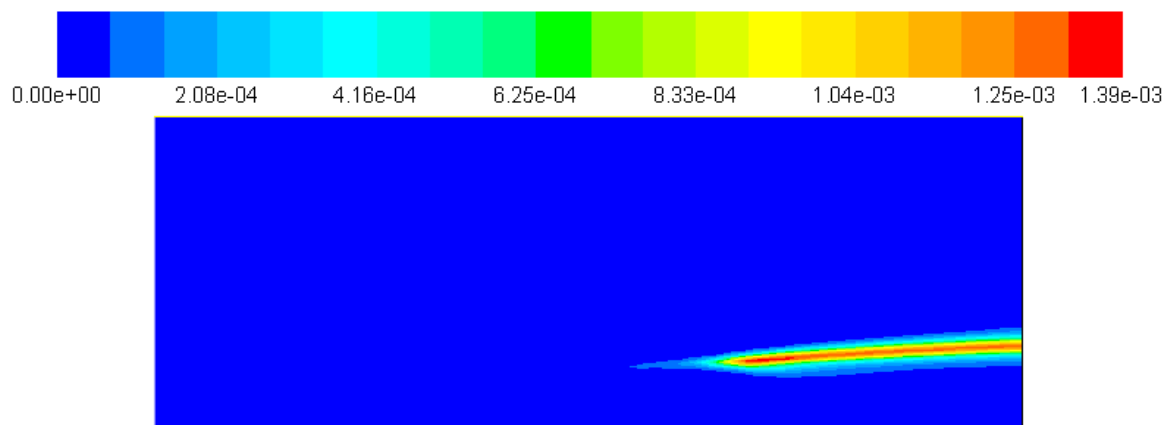
Figure 3.20: Predicted OH distribution of DJHC-X $Re_{jet} = 4100$ flame

tailed, the change of mean coflow temperature is 18.4% while the oxygen concentration varies 43%, which means the influence of coflow temperature is larger than that of coflow oxygen concentration. However, the largest OH concentration is slightly larger than DJHC-I Re=4100 case, which illustrates that the effect of the changing coflow is to lower the OH concentration in the near jet nozzle regime, while the OH concentration in further down-

stream area is increased.

A more comprehensive experimental study of the synthetic effects of jet Reynolds number, coflow temperature, and coflow oxygen concentration on liftoff height has been made by Medwell and Dally[64], but is not available in DJHC burner.

3.4.2.3. INFLUENCE ON PEAK TEMPERATURE

The figure of peak temperature change for different cases is shown in Fig. 3.21. In the Adelaide burner, the decreasing oxygen level is found to bring a maximum peak temperature reduction of 400 K[60], but the coflow temperature is maintained at 1300 K, which makes it not possible to experimentally analyse both temperature and oxygen effect. Later, Medwell and Dally[64] analysed the combined effect of both coflow temperature and oxygen on liftoff height, but no downstream temperature data is available. A comparison between DJHC-V and DJHC-X case could illustrate the issue.
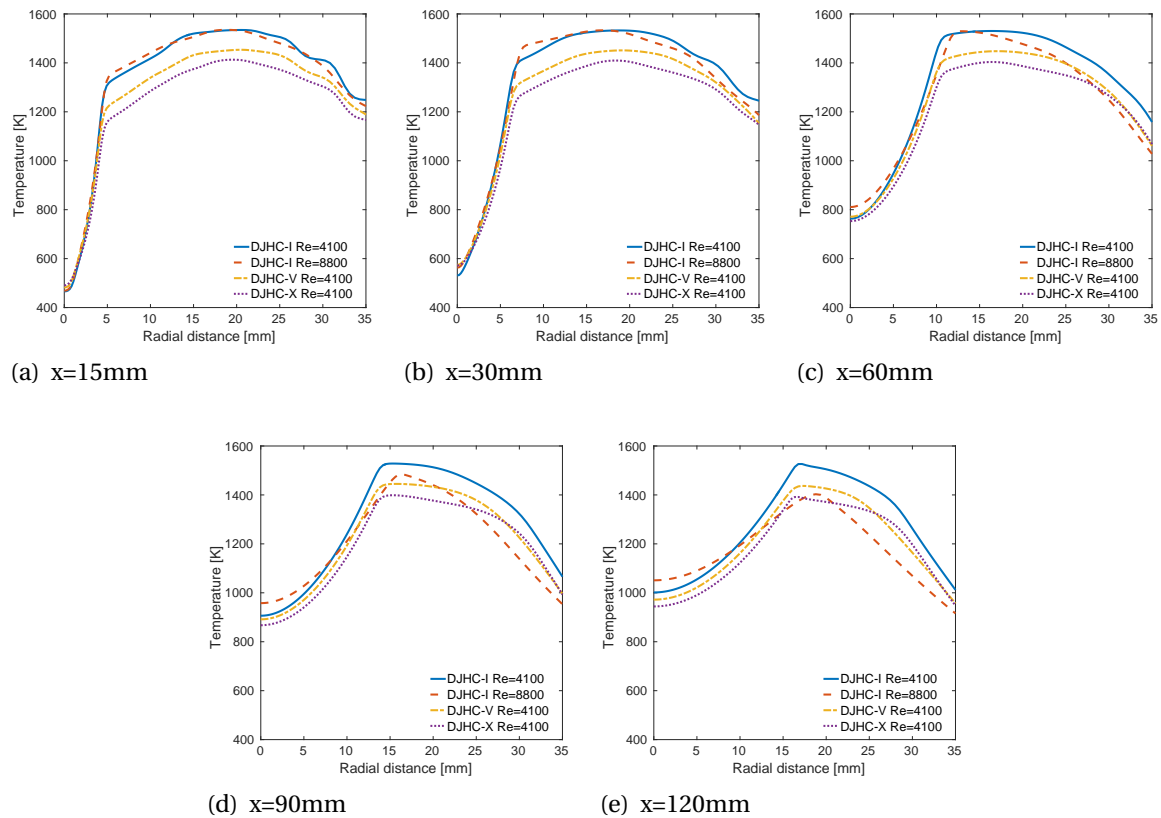
Figure 3.21: Temperature prediction of different cases

Theoretically, an increase of O_2 concentration in the coflow would enhance the reaction, while the decrease of coflow temperature may have an opposite effect. The figures (3.21) clearly show a trend of reduced peak temperature from case I to case X. From case V to case X, as the percentage of O_2 concentration changing is almost 2.5 times that of coflow

temperature, the effect of temperature is found to be more significant than that of oxygen. Same trend can be found from case I Re=4100 flame to case V, the temperature reduction is even more significant, this may due to the jet temperature difference. DJHC-I Re=4100 case has a higher jet temperature. Besides, the comparison of two different DJHC-I cases illustrate that a higher fuel jet velocity could slightly increase the peak temperature in lower height but reduce the peak temperature a lot in the higher height region, this may due to the spreading of the jet. In the lower region, a stronger entrainment causes a more intensive reaction, while for the higher position the entrainment is weaker.

3.4.2.4. Other Influencing Factors

Influence of Radiation

The influence of radiation is very limited in the DJHC flames according to the simulation. Because the flame is optically thin, an emission only radiation model used by Labahn and Devaud[99] can be applied. It only takes into account the radiation by two species, H_2O and CO_2. The local radiation heat loss is defined as:

$$Q(T, Y_k) = 4\sigma \sum_{i=1}^{n} p_k \times a_{p,k}(T^4 - T_b^4) \tag{3.5}$$

where σ denoted the Stefan-Boltzmann constant, p_k represents the partial pressure of species k, $a_{p,k}$ is the Planck mean absorption coefficient of species k, which are temperature dependent[109]. The predicted temperature profiles are shown in Fig. 3.22. Only the downstream figures are shown for brevity.
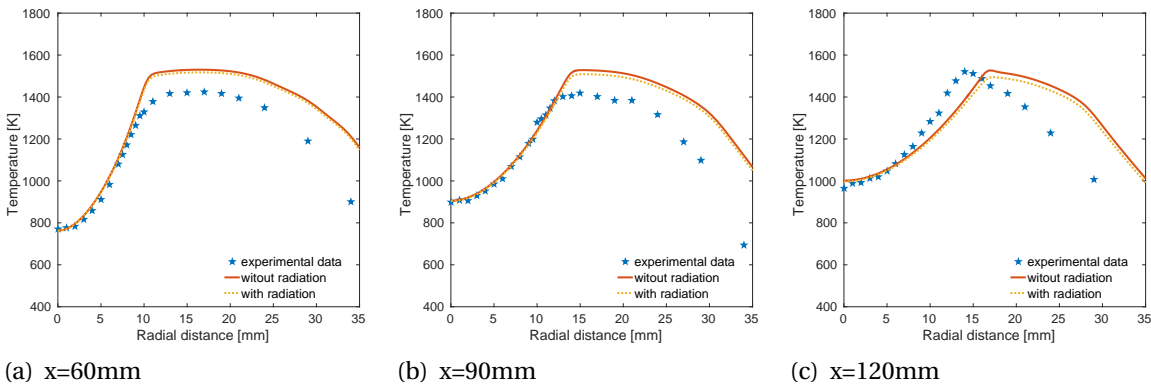
Figure 3.22: Radiation effect on DJHC-I Re=4100 flame

From Fig. 3.22, no significant difference can be found. The largest temperature difference is only around 50 K, which is negligible compared to the local static temperature magnitude. The largest temperature difference exists in the peak temperature area at 120 mm height, which is corresponding to the radiation theory that the larger the temperature is, the higher the radiation effects.Therefore in DJHC case, the effect of radiation can

be neglected. The previously mentioned coflow temperature fluctuation found in DJHC-I
Re=4100 case can not be explained by radiative heat loss.

INFLUENCE OF CHEMICAL MECHANISM

In the previous simulation, the chemical mechanism DRM 19 is used, which is a reduced
version of GRI-Mech 1.2 that is developed by University of California at Berkeley[110], in-
cluding 19 species and 84 reactions. A more detailed mechanism, GRI-Mech 3.0[111] which
includes 53 species and 325 reactions could also be used. The main improvements are ki-
netic rates and thermodynamic properties are updated by newer literature results. The
NO formation and reburn chemistry are also considered. It is said that the GRI-Mech 3.0
mechanisms is able to predict the NO_x emission to a satisfactory level[95]. In this section,
the predictions of the two mechanisms are compared.

As analysed before, the EDC model mainly influences the temperature field rather than
the flow field, only the temperature prediction is shown in Fig. 3.23. The analysed case is
the DJHC-I Re=4100 case.

(a) x=15mm   (b) x=30mm   (c) x=60mm

(d) x=90mm   (e) x=120mm
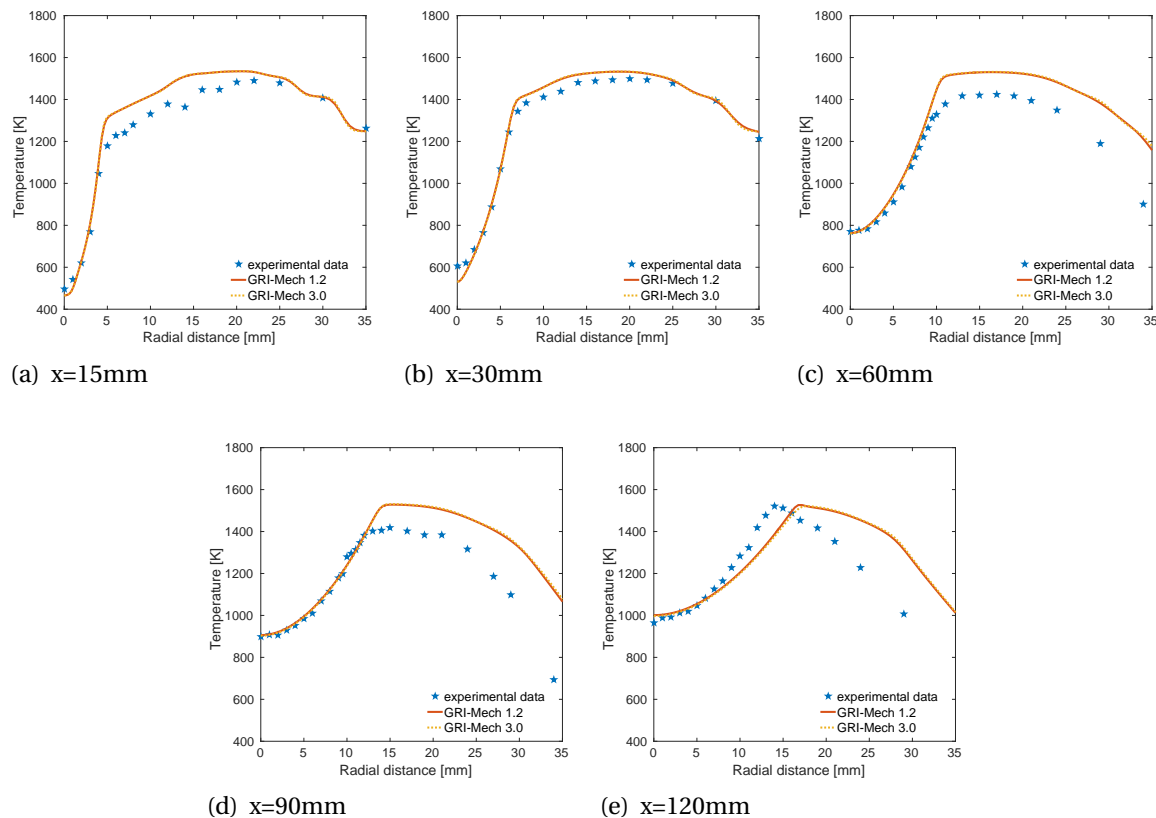
Figure 3.23: Prediction of temperature using two different chemical mechanisms

From figures (3.23), the temperature predictions of two mechanisms show limited dif-
ference. However, the computational time is not comparable, the more detailed mecha-

nism GRI-Mech 3.0 spend almost 6 times longer time compared to DRM 19 based on GRI-Mech 1.2. The advantage in this case is the possibility of analysing NO_x emission instead of using post processing, but for DJHC case the NO_x pollutant is very limited. In this sense, the choose of DRM 19 is acceptable.

INFLUENCE OF LAMINAR DIFFUSION

As described before, in species transportation, two diffusion terms, named by laminar diffusion (Equation 2.56) and turbulent diffusion (Equation 2.57) are considered. In high Reynolds number flows, the laminar diffusion (also called molecular diffusion) is much smaller than the turbulent diffusion term, thus the laminar diffusion coefficient can be approximated as constant over the whole computational region with the same value for all species are equal in fluent. The molecular diffusion term $\overline{D}_k$ then follows from the equation shown below:

$$\overline{D}_k = \frac{\lambda}{Le_k \rho C_p} \tag{3.6}$$

where Le_k is the turbulent Lewis number ($Le_k = Sc_{kt}/Pr_{st}$). The value of Le_k is set to 1. The determination of turbulent diffusion term given by Eq. (2.57) is related to Sc_{kt}, which is simplified to a constant value of 0.7 in fluent.

However, Christo et al.[41] found that in the JHC experiment on MILD combustion, the two terms, laminar and turbulent diffusion, can be comparable. A more detailed model for laminar diffusion term is needed. Certainly, this would increase the computational time of the simulation. Nevertheless, Parente et al.[112] draw a different conclusion on an industrial MILD combustion burner. After applying Chapman–Enskog formula in Fluent, they found that the role of differential diffusion is not important in the numerical simulation of a jet issuing in a hot diluted coflow. Mardani et al.[88] used the ratio between laminar diffusion and turbulent diffusion to reflect the importance of the two terms, the ratio is represented by Dtr. The expression of Dtr is as follows:

$$Dtr = \frac{\overline{\rho}\,\overline{D}_k}{\mu_t Sc_{kt}^{-1}} \tag{3.7}$$

$\overline{D}_k$ and Sc_{kt} are the same for all species in the simple model shown in Equation 3.6. Fig. 3.24 shows a radial profile of Dtr.

From Fig. 3.24, it is clear that in most region, the magnitude of turbulent diffusion is much larger than that of laminar diffusion. However, in the mixing layer, the laminar diffusion could be comparable to the turbulent diffusion, which is corresponding to Christos' and Mardanis' results. It should be pointed out that in the near fuel jet region, the Dtr value in the fuel and coflow mixing layer is larger than that of air and coflow mixing layer, while the two regions have comparable values downstream and the Dtr value in air and coflow
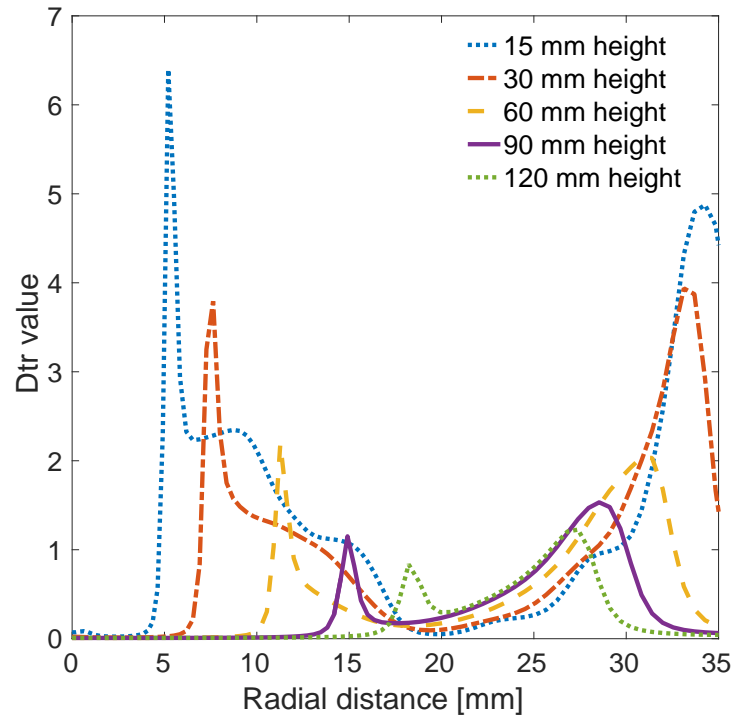
Figure 3.24: Radial profile of Dtr value on different heights

mixing layer becomes larger further downstream but the values in the two region are still on same magnitude. This may illustrate that laminar diffusion plays a more important role in the upstream fuel entrainment and downstream air entrainment process. Another feature is that the peak of Dtr value becomes lower as the distance from fuel jet nozzle increases. According to Mardani et al.[88], the difference of peak temperature brought by differential diffusion model with $Le_k \neq 1$ can be as large as 9% in upstream area, but this difference is sensitive to the jet Reynolds number and could be ignorable in some cases according to Parente et al.[112]. The influence of differential diffusion still needs to be investigated in DJHC case.

4

SIMULATION OF A LABORATORY-SCALE FURNACE

The extended EDC model has been validated in the previous chapter with the database of the DJHC burner, which is used to mimic the recirculation effects that happen in a real furnace. The performance of the extended EDC model in a real furnace needs to be further evaluated. A various experiments and simulations were undertaken, a brief summary of the existing laboratory-scale MILD combustion furnace experiments are listed in Table A.1. Besides, industrial furnaces are also been experimentally studied, including IFRF (International Flame Research Foundation)[113], KTH[16], FGR (flue gas recirculation)[114], and Krishnamurthy[115]. The layouts of these furnaces are not shown, because in this work only the laboratory-scale furnace is numerically investigated. For most of these furnaces, the inlet and exhaust are on same side, while some of the experiment put them on same side. This can force the incoming reactants to mix with exiting products and radicals prior to ignition and establish a low velocity region downstream. The two features enable stabilization with lower inlet temperature[116].

The furnace studied in this work is a reverse flow style burner. Other benefits of this burner including no cooling tube inside the burner, which avoids the influence on flow field, the air inlets are set between the fuel inlet and the exhaust, the dilution of fuel by air can help to reach lower fuel to air ratio which promotes the formation of stable MILD combustion region. Besides, the temperature is determined by Coherent anti-Stokes-Raman spectroscopy (CARS) system, which is more precise compared to the widely used thermal couple in other furnace experiments.

4.1. Configuration of the Laboratory-scale Furnace

The furnace used in this thesis is an ongoing project being experimentally investigated by Xu Huang. The purpose of our simulation is to give guideline predictions for the experiment. The layout of the furnace is shown in Fig. 4.1. The furnace is made up of two parts, a burner and a combustion chamber. Fig. 4.1 (a) is the main view of the furnace, Fig. 4.1 (b) shows the middle cross-section of the furnace, and Fig. 4.1 (c) shows the bottom of the combustion chamber and the arrangement of the fuel and air jet nozzles. As is labelled, the height of chamber is 630 mm while both the width and length are 320 mm. The burner is located in the middle of the chamber bottom, and has a diameter of 92 mm. The fuel jet nozzle is surrounded by four air jet nozzles, located at a circle of 42 mm in diameter. The jet outlet is 30 mm higher than the chamber's inner bottom, while the diameters of fuel nozzle and air nozzles are 4.5 mm and 8.6 mm, respectively. The exhaust leaves from the bottom of the furnace chamber through a slit near the outer wall and is labelled by light yellow in Fig. 4.1 (c). The width of the outlet is 10 mm.

4.2. Set Up of the Simulation

4.2.1. Computational Domain and Grid

Simulations were done only in the combustion chamber. An impression of the grid used is shown in Fig. 4.2, the number of cells is over 800,000, only half of the combustion chamber is simulated because the furnace is symmetrical and the steady state RANS is used. The computational cost is thus reduced.

4.2.2. Models

The turbulence model is chosen to be realizable $k-\epsilon$ model. The advantage of realizable $k-\epsilon$ turbulence model has been mentioned in section 2.3.3. According to Fluent manual[53], realizable k-ϵ model is recommended for axisymmetric jet flows. The study on DJHC burner in Chapter 3 also shows that realizable $k-\epsilon$ model has similar accuracy compared to RSM. The RSM is not used here because k-ϵ is computationally more efficient. For chemical kinetics, a simplified chemistry model developed by Peeters[117] is used in order to reduce the computational cost. The accuracy of the simplified model is compared with the Mech-1.2, no significant thermal difference is seen. This is not shown in the thesis for brevity. For turbulence and chemistry interaction, the new extended EDC model is used. For radiation the weighted-sum-of-gray-gases model (WSGGM) is applied to compute the absorption and emission coefficients of the fluid, the discrete ordinates (DO) model is used to calculate the radiative flux, which solves the radiative transfer equation for a number of discrete solid angles that are related to different vector directions.

320 mm

630 mm

Outlet

Exhaust

Air Inlet

Fuel Inlets

(a) front view   (b) section view   (c) top view
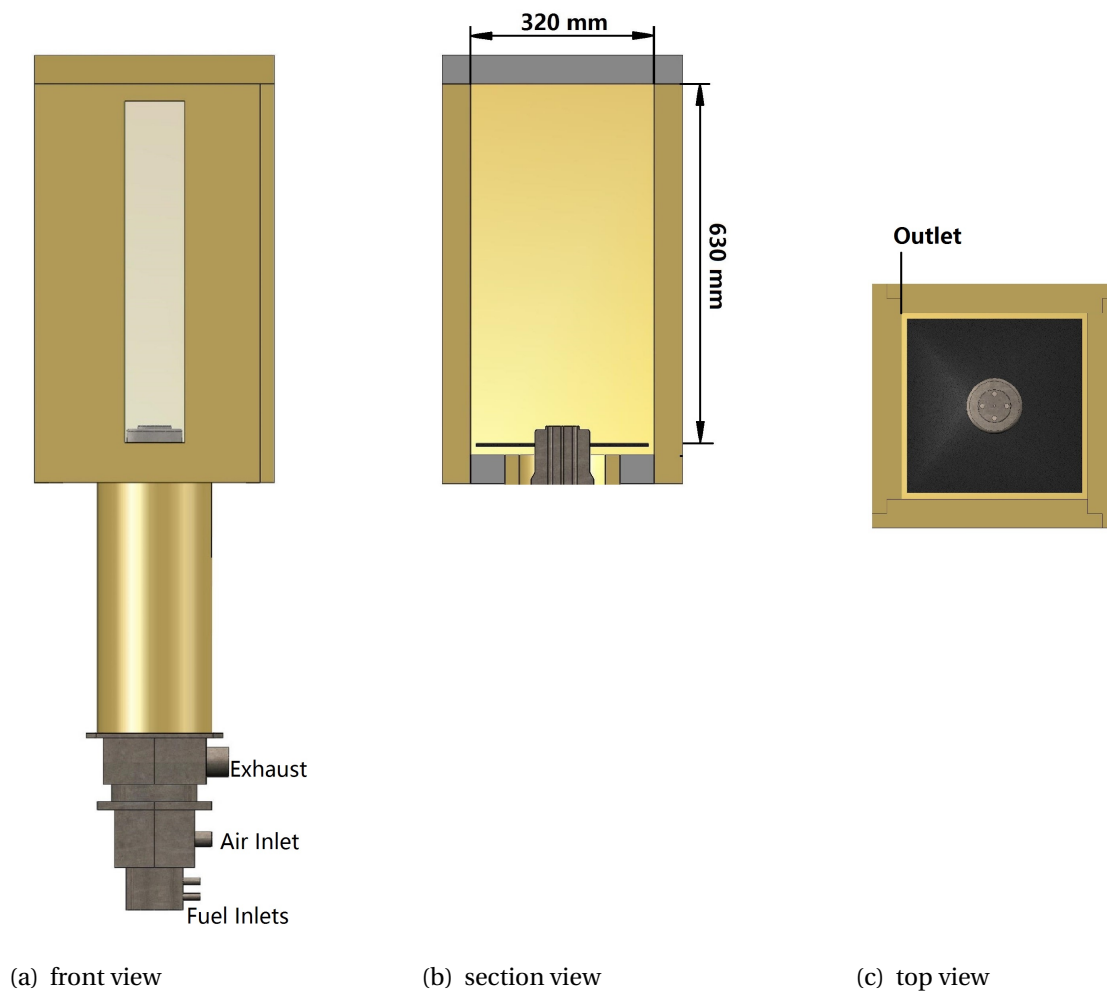
Figure 4.1: Configuration of the laboratory-scale furnace

4.2.3. BOUNDARY CONDITIONS

The inlet (mass flow-in) and outlet (outflow) types are set the same as DJHC burner simulation. Because no experimental data is available, turbulent intensity and hydraulic diameter boundary condition type is chosen instead of the turbulent kinetic energy and eddy dissipation rate type used before. The wall boundary type is no slip wall, which has a temperature of 1200 K.

4.3. RESULT AND DISCUSSION

The following simulations were made for parameter study, application of the extended EDC model and the analysis of NO_x species.
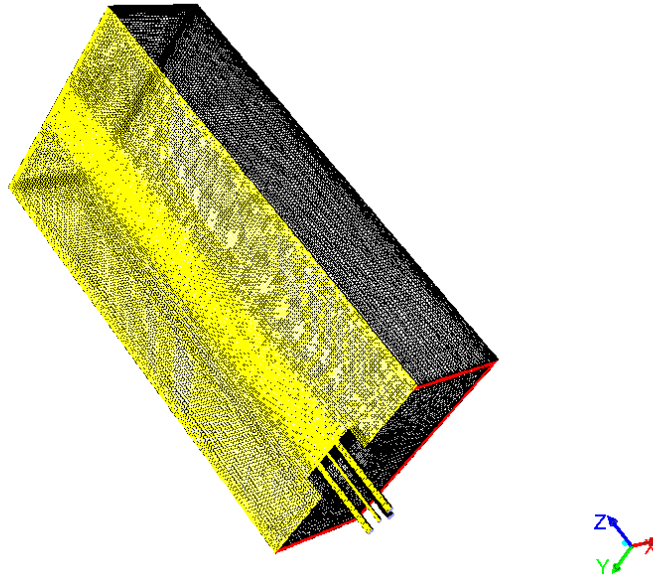
Figure 4.2: Numerical grid of the Laboratory-scale Furnace

4.3.1. PARAMETER STUDY

The standard EDC model is used for the combustion reaction rate term in order to give a reference for the prediction of the extended EDC model.

INFLUENCE OF EDC MODEL CONSTANTS

In the single burner furnace simulation, the original EDC model shows a trend of predicting late ignition. This is different from what was found in the DJHC burner. In the following part it is investigated whether this result is sensitive to the value of EDC model constants. According to Rehm et al.[118], the volume fraction factor C_γ strongly influences the simulation while the residence time scale C_τ has almost no effect on the reaction in furnace. A wide range of C_γ values are tested in this section. The representative figures of temperature and heat release rate indicator on the symmetry plane are shown in Fig. 4.3. The air inlet temperature used here is 873 K.

According to Gordon et al.[77], formaldehyde (CH_2O) is an important precursor species which plays a role in controlling the initiation of reaction, while OH is a key flame-front species which is always corresponding to high temperature. A combined consideration of CH_2O and OH can imply the reaction zone position. Gordon et al. found there are three main stages in the autoignition process: the build-up of precursor pool, the initiation of reaction and the formation of a steady flame. During the autoignition process, the concentration of CH_2O increases significantly while the OH remains on a low level; in the second stage, both CH_2O and OH get to the maximum level, the temperature increases very fast; in the last stage, the CH_2O concentration starts to decrease while the OH peak maintains. In a premixed flame, the overlap of OH and CH_2O only exist in a small region, while the

Temperature field   Formylradical field

(a) $C_\gamma = 2.1377$ (original value)

(b) $C_\gamma = 3.0$

(c) $C_\gamma = 3.7$

(d) $C_\gamma = 4.0$
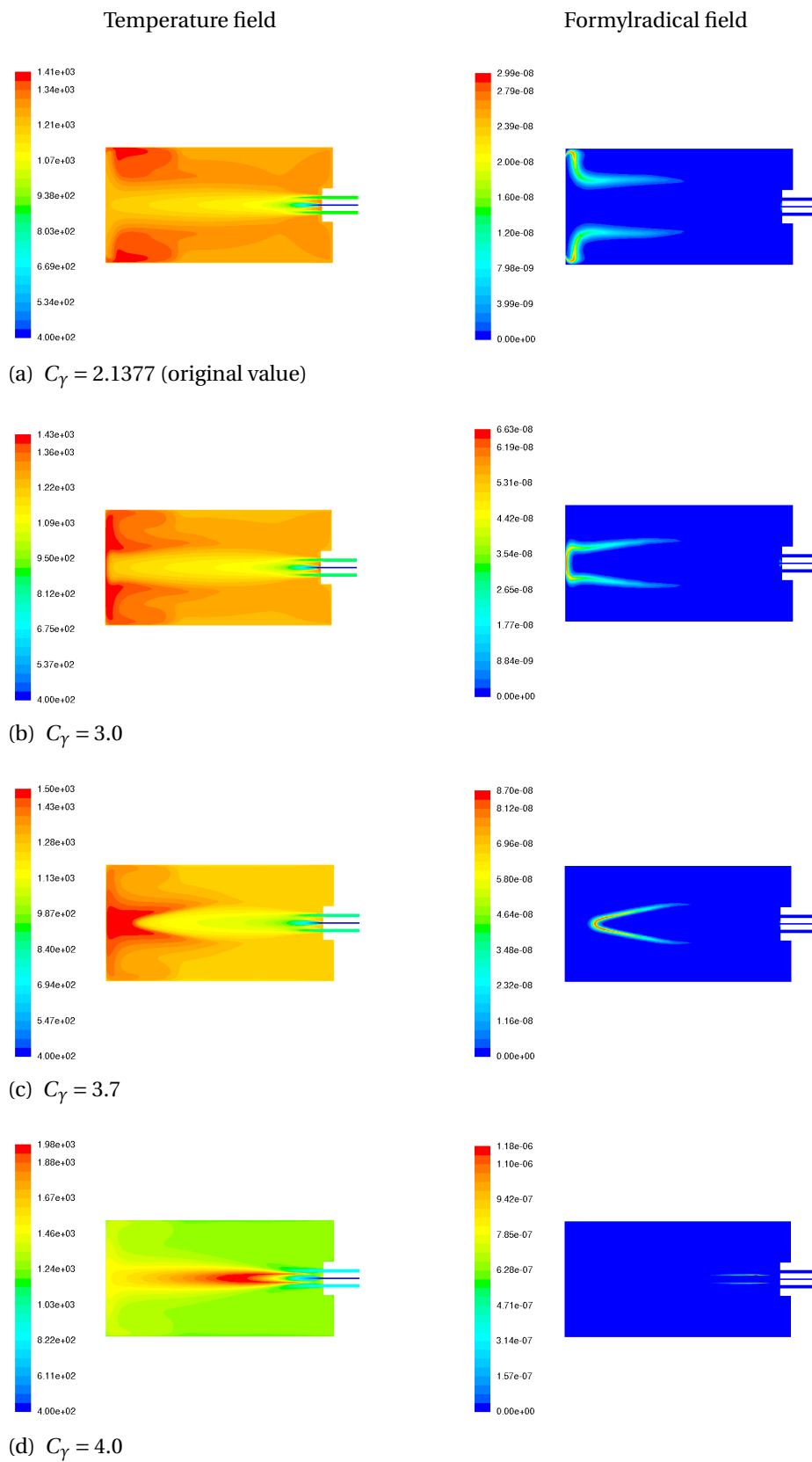
Figure 4.3: Influence of C_γ value on temperature and heat release rate characterised by formylradical

two species overlap across a large region in the case of non-premixed flame. In this sense, Medwell et al.[68] proposed to use the product of OH and CH_2O as an indicator of the heat release rate, which is named as formylradical. The right-hand-side column of figures in Fig. 4.3 are the contour fields of formylradical which stands for the reaction zone.

From the figures (4.3), it is clear that the original EDC model constant C_γ used predicts a late ignition, which is not in agreement with experiment. As explained before, the volume fraction constant C_γ should be increased, while the residence time constant is kept as limited influence on furnace combustion prediction is found[118]. From the formylradical field, it can be seen clearly that the reaction zone is broken because the confinement of the furnace boundary. The recirculation causes the peak temperature appears in two separate zones attach to the side walls, rather than a single flame in the middle. As the volume fraction constant C_γ increases, the two separate flames show a trend of concentrating in the middle, the ignition delay also shows a trend of weakening, while the peak temperature value does not change significantly. However, when the C_γ value is higher than 3.75, the peak temperature becomes very high, and the flame is local and attaches to the burner. This is in disagreement with the MILD combustion characteristic. Finally, a C_γ number of 3.7 is chosen as the best value. The temperature peak is 1500 K, the flame concentrates in the middle top of the furnace. From the formylradical contour, the raction zone is connected, the ignition delay seems to be avoided.
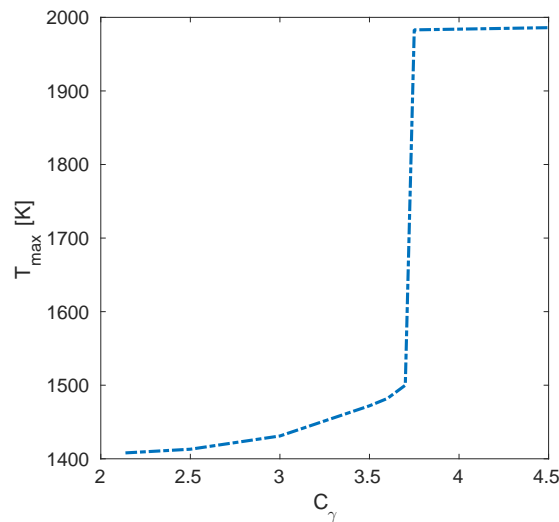
Figure 4.4: The influence of C_γ on maximum temperature

The sensitivity of the peak temperature to the value of C_γ is shown in Fig. 4.4. It can be seen that there is a critical C_γ value 3.75. Below this value, the maximum temperature in the furnace increases gradually in the range of 1400 to 1500 K. After the critical volume fraction constant C_γ, the maximum temperature jumps to as high as 2009 K, which too high that against the temperature requirement of MILD combustion. The temperature increase

is extremely intensive around the critical value 3.75, the slope is almost vertical as shown in Fig. 4.4. This may due to the restriction of EDC model.

INFLUENCE OF AIR INLET TEMPERATURE

As is mentioned in the previous chapter, among the influencing factors are the properties of both fuel jet and air jets, including both temperature and jet velocity. In this laboratory-scale furnace, the wall temperature is around 1200 K according to the thermocouple measurement in literature. While changing temperature, the mass flow of both fuel jet and air jets are kept the same. For this furnace, the air jets are preheated by the combustion products, but its temperature is unclear, which should be tested. Generally, a high air preheated temperature results in high speed at a given mass flow rate, which is in favour of entraining flue gas to dilute the reactants. Therefore it is beneficial to reach MILD combustion. On the other hand, a higher air temperature means less preheating time for fuel which can result in early ignition. In this sense, the temperature should be higher than around 800 K. Therefore cases with the air inlet temperature of 973 K and 1073 K are tested with the standard EDC model constants. In order to understand whether the change of air temperature can influence the ignition height, the standard EDC model constant $C_\gamma = 2.1377$ is used. The related simulation results are shown in Fig. 4.5.

(a) T_{air}=973 K

(b) T_{air}=1073 K
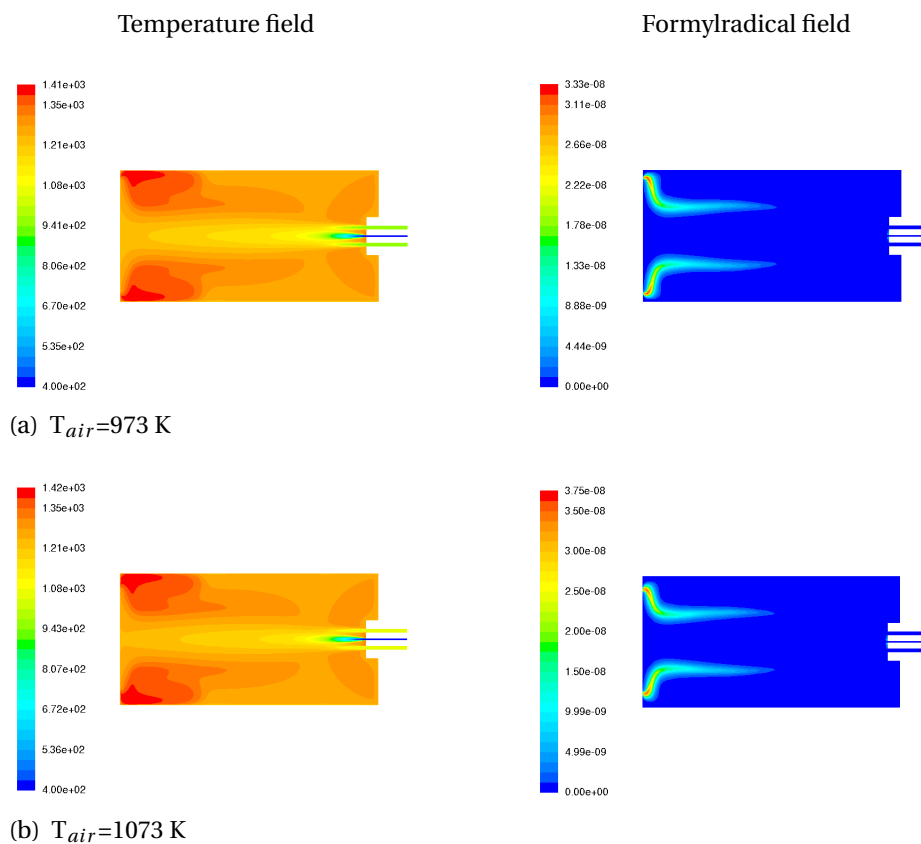
Figure 4.5: Influence of air inlet temperature on temperature and reaction rate

Also compared to Fig. 4.3 (a), the influence of air inlet temperature can be evaluated. The maximum temperature in the furnace does not change a lot, only changes from 1408 K to 1418 K as the inlet temperature increases. This is different from the DJHC burner case, where the coflow temperature is found to have a large effect on the peak temperature. In the burner, the coflow is directly mixed with the fuel and proceeds reaction, but in the burner the air is mixed with the combustion products and fuel together, the reaction occurs in the recirculation zone. The effect of dilution may be the reason to lower the oxidizer temperature effect. The late ignition can not be alleviated by changing the air jet temperature. The formylradical fields show slightly difference, as the air temperature increases, the flame seems to be more concentrated to the middle top, but the position where the reaction starts can not be lowered to the fuel jet nozzle.

A more precise evaluation can be done by the temperature curve. As is shown in Fig. 4.2, the fuel jet direction is the positive z axis, the temperatures on different heights z are shown in Fig. 4.6.

From the figure, the temperature difference brought by different air inlet temperature in the middle (along y direction) seems to be larger than the temperature difference in the near-wall area. The peak temperature becomes closer to the centreline ($y = 0, x = 0$) of the furnace as the air temperature rises, which agrees with the conclusion drawn from formylradical contours. The peak temperature difference increases as z increases, the largest peak temperature increment is around 10 K every 100 K change of air temperature, which can be ignored. The increment in the centreline region every 1000 K change of coflow temperature is around 30 K near the fuel jet nozzle and becomes smaller in downstream.

A temperature higher than 1200 K is not expected in this furnace, which is different from the high temperature level of DJHC burner, and thus bring the different oxidizer temperature influence. To conclude, the air jet temperature in this case does not play an important role in the prediction.

4.3.2. APPLICATION OF THE EXTENDED EDC MODEL

The new extended EDC model has been proved to perform well in the burner case. The performance of the model in the real furnace is to be investigated. In this section, the predictions are gained by using the new extended EDC model. The boundary conditions are set as before, the inlet air temperature used is 873 K.

PREDICTION OF TEMPERATURE AND FORMYLRADICAL

The temperature and formylradical contour fields are shown in Fig. 4.7.

From Fig. 4.7 (a), the temperature contour is very similar to that of the EDC model with the global modification $C_\gamma = 3.7$ prediction. The peak temperature value increases slightly. Meanwhile, a small peak is found around the fuel jet nozzle outlet. However, the

(a) z=200 mm

(b) z=400 mm

(c) z=600 mm

(d) z=620 mm
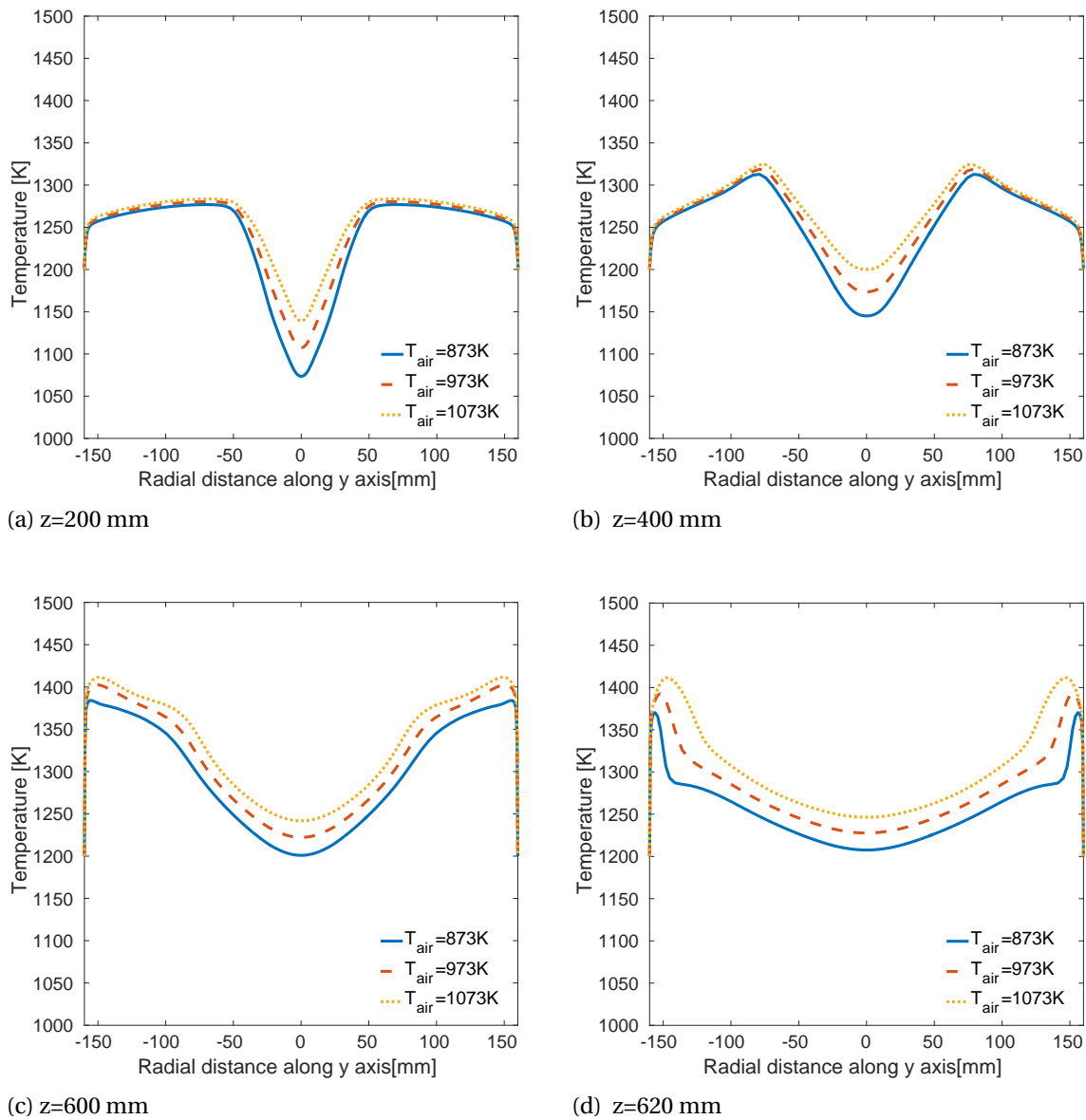
Figure 4.6: Temperature predictions on horizontal cross-section in the middle plane for different air jet temperature using standard EDC model constants

formylradical distribution shows great difference. The peak value drops significantly, and the zone with high values on the symmetry plane breaks into two parts.

The temperature prediction can be analysed in detail in Fig. 4.8. It can be seen that the two methods show similar results in the flame zone. Comparing the temperature prediction on same height by different model, the peak temperature predicted by the local modified model constants is relatively lower compared to that of the global $C_\gamma = 3.7$ model until 400 mm height along the z direction. Meanwhile, for same heights, the peak position predicted by the local constants model becomes farther to the centreline z axis compared to the global $C_\gamma = 3.7$ method. Between $z = 400$ mm and $z = 600$ mm height, the different

(a) temperature
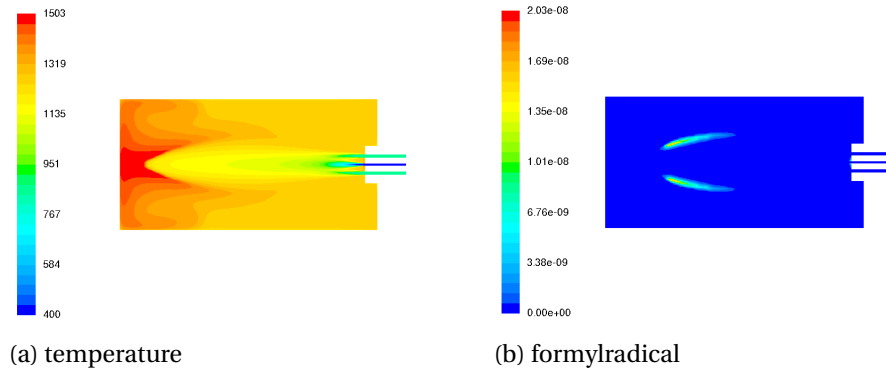
(b) formylradical

Figure 4.7: Contour plot of temperature and formylradical based on the new extended EDC model

peak distance from the centreline brought by the two models become more significant. In this range of height, the lower temperature zone in the middle of the symmetry plane (near z axis) predicted by the new extended EDC model becomes wider compared to the global modification model while the peak temperature value in this height range does not change.

(a) local modification (new extended EDC model)

(b) EDC model with global modification ($C_\gamma = 3.7$)
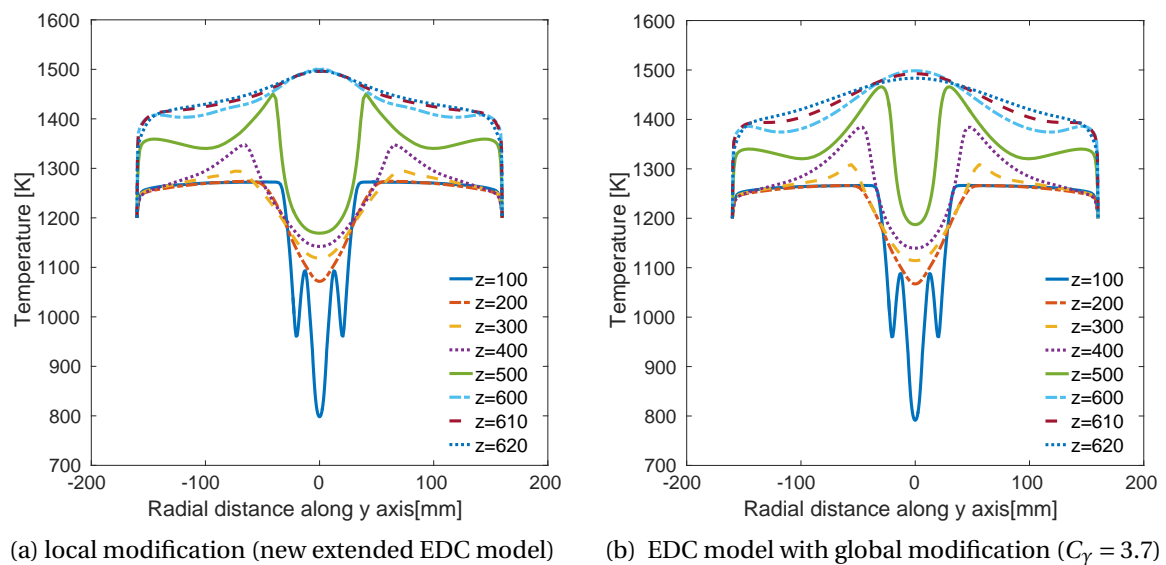
Figure 4.8: Comparison of the temperature predictions along horizontal cross-section (y axis) in the furnace middle plane given by different methods

CONSISTENCY CHECK OF THE CHOICE OF SYMMETRY PLANE

In order to justify the choice of the analysed symmetry plane, the temperature prediction of the xoz plane is compared with the yoz plane. From the symmetry of furnace and burner, one would expect identical results. Fig. 4.9 (a) shows the temperature contour of the xoz symmetry plane. Fig. 4.9 (b) is a comparison of temperature prediction between the two

different plane chosen, the new selected plane is labelled by circle. For the yoz plane results, only the temperature prediction of negative y direction is shown in order to avoid the superposition of different set of data.

(a) temperature field of the xoz symmetry plane

(b) comparison of the radial temperature prediction on different symmetry planes
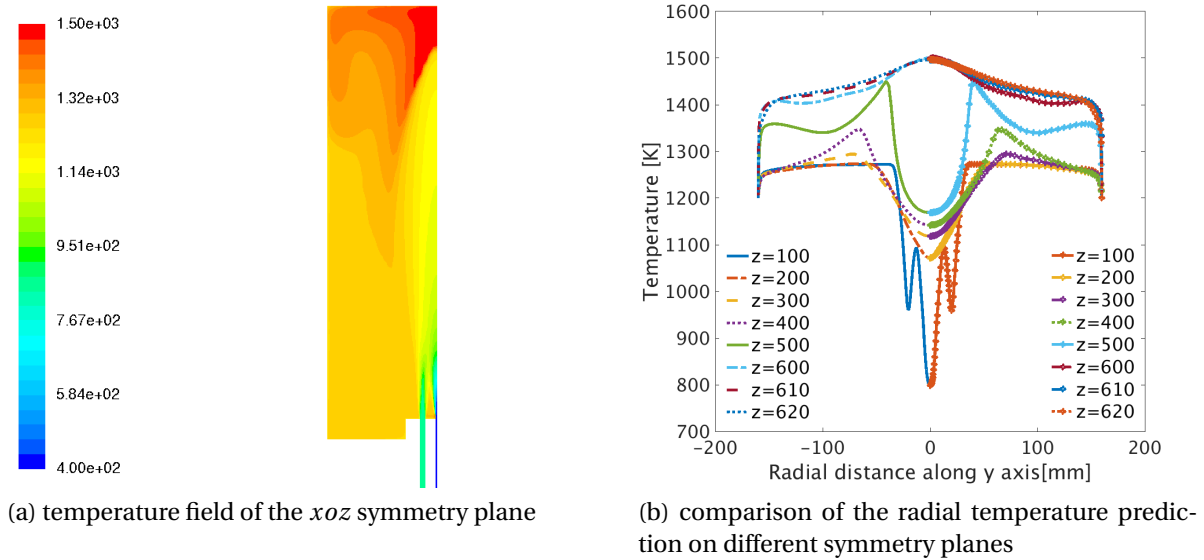
Figure 4.9: Comparison of the temperature predictions of different symmetry plane

From Fig. 4.9, the two set of data are exactly symmetric. This illustrates that the simulation is converged. The analysis of only the yoz plane is reasonable.

PREDICTION OF VELOCITY

The velocity prediction is shown in Fig.4.10.

(a) contour field   (b) vector field
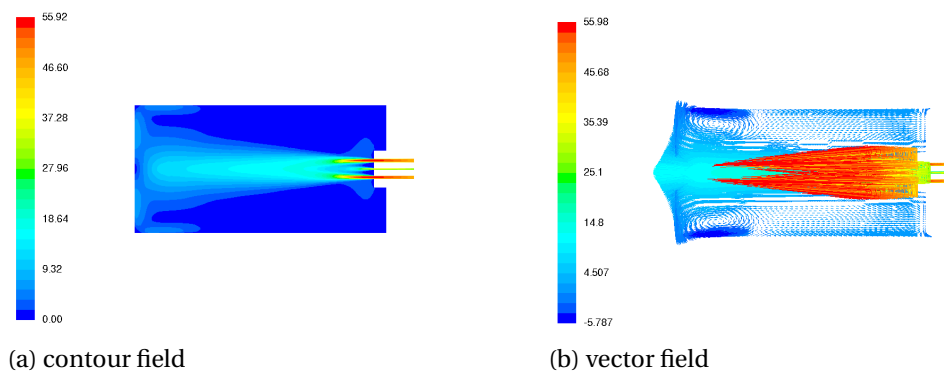
Figure 4.10: Prediction of velocity using the new extended EDC model

The jet decay can be easily seen from Fig. 4.10 (a). The velocity vectors are shown in Fig. 4.10 (b). The vectors are coloured by the velocity along z axis, the negative z velocity is coloured by deep blue. In this way, the flow field is reflected clearly. It is clear that in

the top corner the recirculation zone is formed. The maximum recirculated velocity (along negative z direction) can be approximately 5.8 m/s. Overall, the fuel jet and air jets mix with each other and form a high speed jet in the middle first, the high speed jet is impeded by the top wall of the furnace and larger vortex is formed in the corner, the recirculation is thus caused. The combustion products leave the furnace through the outlet on the bottom in the region close to the wall afterwards. The difference between the standard EDC model and extended EDC model does not significantly influence the velocity prediction, which is not shown in the thesis for brevity.

EFFECT OF THE EXTENDED EDC MODEL

As is mentioned in section 4.3.1, only the volume fraction constant C_γ is important for the furnace case. The locally changed C_γ is shown in Fig. 4.11. From the figure, it can be seen
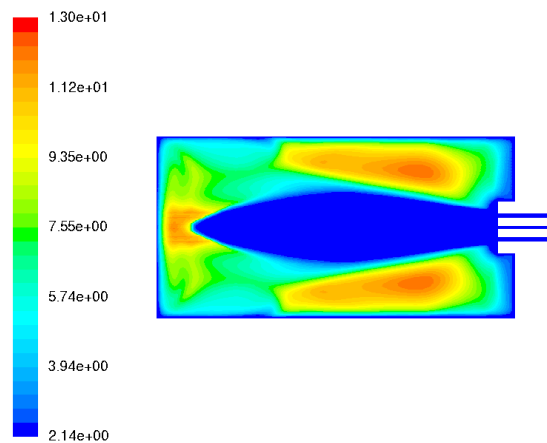
Figure 4.11: Modified C_γ: local values in the new extended EDC model

the C_γ value is higher than the standard value 2.1377 in most of the cross-section. The C_γ value in the high temperature zone can be higher than 10, while in the recirculation effect region the C_γ value is in the range of 5 to 8. A high C_γ region can be also found in the bottom corner, but no reaction is found in this zone. This is due to the low reactants concentration in this area. In a word, the C_γ value is changed significantly and thus influences the temperature prediction.

4.3.3. NO$_x$ ANALYSIS

NO$_x$ consists of nitric oxide (NO), nitrogen dioxide (NO$_2$) and nitrous oxide (N$_2$O), among all NO$_x$ species in global. Nitric oxide is the most prominent throughout the furnace volume. The formation of NO$_x$ can be divided into five processes: thermal NO$_x$ formation, prompt NO$_x$ formation, fuel NO$_x$ formation, intermediate N$_2$O, and NO$_x$ reduction by reburning. Until now, a lot of investigations have shown that the low NO$_x$ emission in MILD

combustion is due to the reduction of N_2O intermediate. They draw the conclusion that the prompt NO_x formation dominates in forming NO under MILD combustion[75, 105, 119, 120]. However, according to Wang et al.[95], the role of reburning can differ greatly when the operating conditions are changed. Some other researchers also found N_2O intermediate can be important[16, 121]. In this thesis, all the processes are considered. The following figure plots the NO results (by volume fraction):
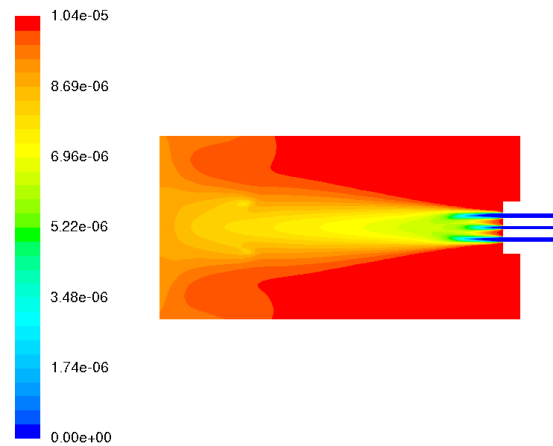
Figure 4.12: Contour plot of NO volume fraction

From Fig. 4.12, the magnitude of NO concentration is ppmv (parts per million volume), which is corresponding to the definition of MILD combustion given by Milani[19]. The largest concentration is around 10 ppmv. The higher temperature area has a relatively lower NO concentration, indicating that thermal NO_x formation is not the dominant process.

5

CONCLUSIONS AND RECOMMENDATIONS

5.1. CONCLUSIONS

In this thesis, the performance of an extended EDC model is evaluated through the commercial CFD package ANSYS Fluent (version 14.5). Two sets of combustion equipment, the DJHC burner and a MILD combustion furnace, were tested. According to the simulation results, the new EDC model is able to give better prediction compared to other EDC models.

5.1.1. THE JET-IN-HOT-COFLOW BURNER

For the DJHC burner case, the simulation results are compared with the experimental data. The conclusions are as follows:

1. Different turbulence models are compared. The modified standard k-ϵ model is commonly used for Adelaide burner is found to be not suitable for the DJHC burner. The RSM turbulence model is proved to be the best to fit the DJHC burner by taking into account three representative regions. The species mixing, the flow field and the temperature are considered to come to this conclusion.

2. The new extended EDC model is validated in terms of temperature, flow field and liftoff height. The new extend EDC model is shown to better predict the peak temperature while the accuracy of turbulence prediction is not influenced. Different EDC models are compared. The new quantitative model is found to better than the model proposed earlier by Parente et al.[58] in terms of both the computational cost and the temperature prediction.

3. The influencing factors are investigated considering different DJHC flames. The results are shown in Table 5.1.

Table 5.1: Influencing factors of DJHC flame

	flame width	flame length	liftoff height	peak temperature
$V_{jet}\uparrow$	$\downarrow$	$\rightarrow$	$\downarrow$	depends
$T_{jet}\downarrow$	$\uparrow$	$\uparrow$	$-$	$\uparrow$
$T_{coflow}\downarrow$	$\downarrow$	$\downarrow$	$\uparrow$	$\downarrow$
$O_{2coflow}\%\uparrow$	$\downarrow$	$\downarrow$	$\downarrow$	$\uparrow$

It should be pointed out that the influence of jet temperature on flame volume is larger than both that of jet velocity and coflow temperature. For liftoff height, the influence of coflow temperature is larger than the coflow oxygen concentration level. In DJHC burner experiment, an increased oxygen concentration of coflow is always related to a decreased coflow temperature. Due to this limitation, the specific influence of coflow oxygen concentration and temperature on flame width cannot be identified from the current study and would need more investigations.

5.2. THE MILD FURNACE

The laboratory-scale MILD furnace is still being investigated experimentally, the extended EDC model has been used to give theoretical insight. The influence of uncertain air inlet temperature is found to be limited due to dilution effect. A global model constant C_γ study shows that 3.7 is the best choice for this laboratory-scale MILD furnace. The extended EDC model shows similar results as the global EDC model constant method in terms of temperature. However, the formylradical field shows difference. The heat release zone in the symmetry plane is split into two parts in the case of new extended EDC model. The plot of local changed C_γ shows that for the high temperature zone, the C_γ value is in the range of 8 to 12, which is higher compared to the DJHC burner. A plot of velocity vectors clearly shows a strong recirculation on the top corner of the furnace. The NO_x analyse shows the NO pollutant is on the level of ppmv, which is extremely low compared to conventional combustion.

5.3. RECOMMENDATIONS

In this thesis, we obtained a better understand of the chemistry and turbulence interaction in MILD combustion. The following recommendations are suggested for further research, which are based on both model and experiment consideration:

MODEL IMPROVEMENT

- The calculation of chemical time scale in the current model is based on one-step chemical reaction assumption. A more precise calculation taking into account the detailed chemical mechanism is believed to be able to increase the accuracy of the prediction. The method used by Schütz et al.[104] in their Partially Stirred Reactor Model can be a possible procedure to provide a better chemical time scale for the extended EDC model.

- The analysis of laminar diffusion in DJHC burner shows that the magnitude of turbulent diffusion and laminar diffusion can be comparable in the mixing layer. Therefore, an application of a detailed molecular diffusion model replacing the $Le_k = 1$ model can improve the simulation.

BOUNDARY CONDITIONS TREATMENT

- RSM is very sensitive to the turbulence property of the inlet. The turbulence dissipation rate has been modelled according to the experimental turbulence Reynolds stresses data, but an improved model of turbulence dissipation rate at the inlet can certainly help to better predict the turbulence.

EXPERIMENTS

- The over-prediction of coflow temperature in DJHC burner seems to be common in different numerical studies. The composition of coflow is calculated based on equilibrium hypothesis and the measured temperature and oxygen level of coflow. The inaccuracy of measured oxygen concentration can be the possible cause of inaccuracy of coflow temperature prediction. Additional measurements would be useful.

- In the DJHC experiment, the coflow temperature and oxygen concentration are changing together in opposite direction. This makes it impossible to understand the effect of the two factors separately on flame width. Experiments that allow the modification of two issues separately can be done.

OTHER MORE PROMISING MODELS

- The limitation of EDC model is strongly felt during the study. A more complicated combustion model such as FGM and PDF is needed to obtain more accurate predictions.

- An unsteady simulation(LES) can give a better prediction of mixing and temperature fluctuations. In this way the flame structure can be better understood. This has already been achieved for the DJHC burner using LES in combination with CSE by

Labahn and Devaud[99]. It would be of interest to use LES and CSE also for the furnace simulation.

A

EXISTING LABORATORY-SCALE MILD FURNACE EXPERIMENTS

The table below shows the burner configuration of existing laboratory-scale MILD combustion furnaces. The fuel inlet is labelled by shadows, the air inlet is labelled by triangles while the premixed burner inlet is marked by both triangles and shadows. For some furnaces, the outlet and inlet are on same side, the outlet in this case is labelled by points.

Table A.1: Burner Configuration of Existing Laboratory-scale MILD Furnace Experiments

▨ fuel inlet	▽ air inlet	▨ premixed inlet	⋮ exhaust

Burner configuration	Size of chamber	Reverse exhaust	Ref.
Wünning			
	250×250×485	No	[10]
	250×250×485	No	[10]

Burner configuration	Size of chamber	Reverse exhaust	Ref.
Stagnation Point Reverse Flow (SPRF)			
	$\phi 70 \times 300$	Yes	[116]
DLR			
	$\phi 100 \times 200$	No	[104]
Adelaide			
	$250 \times 250 \times 485$	Yes	[122]
	$250 \times 250 \times 485$	Yes	[123]
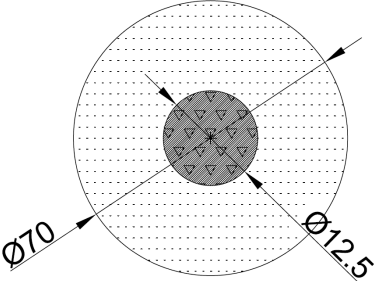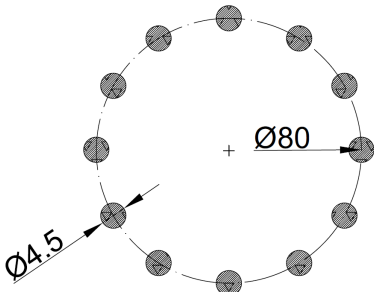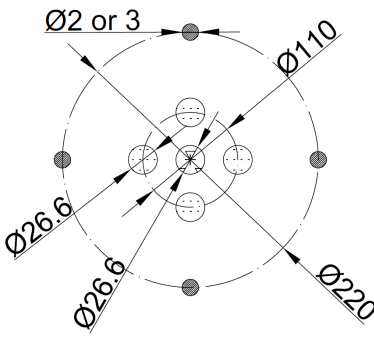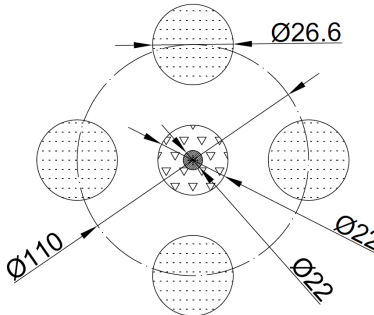
Burner configuration	Size of chamber	Reverse exhaust	Ref.
Lisbon			
	$\phi100\times340$	No	[124]
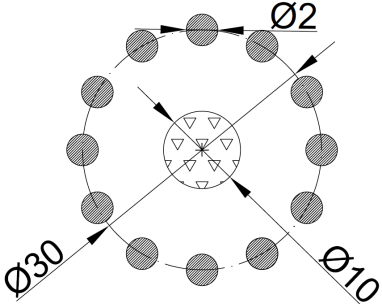
BIBLIOGRAPHY

[1] Z. Jiang, *Reflections on energy issues in China,* Journal of Shanghai Jiaotong University (Science) **13**, 257 (2008).

[2] BP Energy Outlook, *Outlook to 2035,* BP (http://bp.com/energyoutlook) (2014).

[3] BP Energy Outlook, *BP Energy Outlook - 2016 edition,* BP (http://bp.com/energyoutlook) (2016).

[4] D. Helm, *The future of fossil fuels—is it the end?* Oxford Review of Economic Policy **32**, 191 (2016).

[5] OPEC Press Releases, *OPEC bulletin April 2016,* BP (http://www.opec.org/opec_web/static_files_project/media/downloads/publications/OB042016.pdf) (2016).

[6] International Energy Agency, *Energy and Climate Change,* OECD/IEA (https://www.iea.org/publications/freepublications/publication/WEO2015SpecialReportonEnergyandClimateChange.pdf) (2015).

[7] Intergovernmental Panel on Climate Change, *Climate Change 2014–Impacts, Adaptation and Vulnerability: Regional Aspects* (Cambridge University Press, 2014).

[8] S. Solomon, D. Qin, M. Manning, Z. Chen, M. Marquis, K. Averyt, M. Tignor, and H. Miller, *Contribution of working group I to the fourth assessment report of the intergovernmental panel on climate change, 2007,* Climate Change 2007: Working Group II: Impacts, Adaptation and Vulnerability (2007).

[9] United Nations Framework Convention on Climate Change (UNFCCC), *the paris agreement,* in *21st Conference of the Parties, Paris: United Nations* (2015).

[10] J. Wünning and J. Wünning, *Flameless oxidation to reduce thermal no-formation,* Progress in energy and combustion science **23**, 81 (1997).

[11] M. Katsuki and T. Hasegawa, *The science and technology of combustion in highly preheated air,* in *Symposium (International) on combustion,* Vol. 27 (Elsevier, 1998) pp. 3135–3146.

[12] T. Hasegawa and R. Tanaka, *High Temperature Air Combustion. Revolution in Combustion Technology.(Part I New Findings on High Temperature Air Combutions.)*, JSME International Journal Series B **41**, 1079 (1998).

[13] N. Shimo, *Fundamental research of oil combustion with highly preheated air,* in *Proceedings of the 2nd International Seminar on High Temperature Combustion in Industrial Furnaces* (2000).

[14] A. Gupta, S. Bolz, and T. Hasegawa, *Effect of air preheat temperature and oxygen concentration on flame structure and emission,* Journal of energy resources technology **121**, 209 (1999).

[15] S. Lille, W. Blasiak, and M. Jewartowski, *Experimental study of the fuel jet combustion in high temperature and low oxygen content exhaust gases,* Energy **30**, 373 (2005).

[16] W. Yang and W. Blasiak, *Flame entrainments induced by a turbulent reacting jet using high-temperature and oxygen-deficient oxidizers,* Energy & fuels **19**, 1473 (2005).

[17] A. Cavaliere and M. de Joannon, *Mild combustion,* Progress in Energy and Combustion science **30**, 329 (2004).

[18] S. Kumar, P. Paul, and H. Mukunda, *Studies on a new high-intensity low-emission burner,* Proceedings of the combustion institute **29**, 1131 (2002).

[19] A. Milani and J. Wünning, *What is flameless combustion?* IFRF Online Combustion Handbook (http://www.handbook.ifrf.net/handbook/cf.html?id=171) (2002).

[20] J. Wünning, *Flameless oxidation,* in *6th HiTACG Symposium, Essen, Germany* (2005).

[21] R. Cabra, T. Myhrvold, J. Chen, R. Dibble, A. Karpetis, and R. Barlow, *Simultaneous laser Raman-Rayleigh-LIF measurements and numerical modeling results of a lifted turbulent H_2/N_2 jet flame in a vitiated coflow,* Proceedings of the Combustion Institute **29**, 1881 (2002).

[22] T. Poinsot and D. Veynante, *Theoretical and numerical combustion* (RT Edwards, Inc., 2005).

[23] K. K. Kuo, *Principles of combustion* (John Wiley & Sons, Inc., 1986).

[24] G. Williams, *Combustion theory* (Citeseer, 1985).

[25] D. A. Anderson, J. C. Tannehill, and R. H. Pletcher, *Computational fluid mechanics and heat transfer* (Hemisphere Publishing, New York, NY, 1984).

[26] H. S. Harned, J. O. Hirschfelder, C. F. Curtis, and R. B. Bird, *Molecular Theory of Gases and Liquids* (JSTOR, 1955).

[27] A. Favre, *Statistical equations of turbulent gases,* Problems of hydrodynamics and continuum mechanics , 231 (1969).

[28] H. Tennekes and J. L. Lumley, *A first course in turbulence* (MIT press, 1972).

[29] W. P. Jones and B. E. Launder, *The prediction of laminarization with a two-equation model of turbulence,* International journal of heat and mass transfer **15**, 301 (1972).

[30] S. Sarkar, G. Erlebacher, M. Hussaini, and H. Kreiss, *The analysis and modelling of dilatational terms in compressible turbulence,* Journal of Fluid Mechanics **227**, 473 (1991).

[31] B. E. Launder and D. Spalding, *The numerical computation of turbulent flows,* Computer methods in applied mechanics and engineering **3**, 269 (1974).

[32] T.-H. Shih, J. Zhu, and J. L. Lumley, *A new Reynolds stress algebraic equation model,* Computer methods in applied mechanics and engineering **125**, 287 (1995).

[33] T.-H. Shih, J. Zhu, and J. L. Lumley, *A realizable Reynolds stress algebraic equation model,* in *Symposium on Turbulence Shear Flows; 9th; 10-18 Aug. 1993; Kyoto; Japan* (1993).

[34] B. E. Launder, G. J. Reece, and W. Rodi, *Progress in the development of a Reynolds-stress turbulence closure,* Journal of fluid mechanics **68**, 537 (1975).

[35] B. J. Daly and F. H. Harlow, *Transport equations in turbulence,* Physics of Fluids (1958-1988) **13**, 2634 (1970).

[36] F.-S. Lien and M. Leschziner, *Assessment of turbulence-transport models including non-linear RNG eddy-viscosity formulation and second-moment closure for flow over a backward-facing step,* Computers & Fluids **23**, 983 (1994).

[37] S. Sarkar and B. Lakshmanan, *Application of a Reynolds stress turbulence model to the compressible shear layer,* AIAA journal **29**, 743 (1991).

[38] J. Rotta, *Statistische Theorie nichthomogener Turbulenz,* Zeitschrift für Physik **129**, 547 (1951).

[39] M. M. Gibson and B. E. Launder, *Ground effects on pressure fluctuations in the atmospheric boundary layer,* Journal of Fluid Mechanics **86**, 491 (1978).

[40] T. J. Craft and B. E. Launder, *New wall-reflection model applied to the turbulent impinging jet,* AIAA journal **30**, 2970 (1992).

[41] F. Christo and B. B. Dally, *Modeling turbulent reacting jets issuing into a hot and diluted coflow,* Combustion and flame **142**, 117 (2005).

[42] D. Veynante and L. Vervisch, *Turbulent combustion modeling,* Progress in energy and combustion science **28**, 193 (2002).

[43] N. Peters, *Turbulent combustion* (Cambridge university press, 2000).

[44] D. Spalding, *Mixing and chemical reaction in steady confined turbulent flames,* in *Symposium (International) on Combustion,* Vol. 13 (Elsevier, 1971) pp. 649–657.

[45] B. F. Magnussen and B. H. Hjertager, *On mathematical modeling of turbulent combustion with special emphasis on soot formation and combustion,* in *Symposium (International) on Combustion,* Vol. 16 (Elsevier, 1977) pp. 719–729.

[46] B. F. Magnussen and B. Hjertager, *On the structure of turbulence and a generalized eddy dissipation concept for chemical reaction in turbulent flow,* in *19th AIAA Aerospace Meeting, St. Louis, USA,* Vol. 198 (1981).

[47] I. S. Ertesvåg and B. F. Magnussen, *The eddy dissipation turbulence energy cascade model,* Combustion science and technology **159**, 213 (2000).

[48] R. Ryden, L.-E. Eriksson, and S. Olovsson, *Large eddy simulation of bluff body stabilised turbulent premixed flames,* in *ASME 1993 International Gas Turbine and Aeroengine Congress and Exposition* (American Society of Mechanical Engineers, 1993) p. V03AT15A008.

[49] B. F. Magnussen, *Modeling of NO_x and soot formation by the Eddy Dissipation Concept,* Int. Flame Research Foundation (1989).

[50] I. R. Gran and B. F. Magnussen, *A numerical study of a bluff-body stabilized diffusion flame. Part 2. Influence of combustion modeling and finite-rate chemistry,* Combustion Science and Technology **119**, 191 (1996).

[51] B. Magnussen, B. H. Hjertager, J. Olsen, and D. Bhaduri, *Effects of turbulent structure and local concentrations on soot formation and combustion in C_2H_2 diffusion flames,* in *Symposium (International) on Combustion,* Vol. 17 (Elsevier, 1979) pp. 1383–1393.

[52] S. B. Pope, *Computationally efficient implementation of combustion chemistry using in situ adaptive tabulation,* Combust. Theory Modelling **1**, 41 (1997).

[53] Fluent Manual, *Ansys fluent theory guide 15.0,* Inc, Canonsburg, PA (2013).

[54] K. Annamalai and I. K. Puri, *Combustion science and engineering* (CRC press, 2006).

[55] A. De, E. Oldenhof, P. Sathiah, and D. Roekaerts, *Numerical simulation of Delft-jet-in-hot-coflow (DJHC) flames using the eddy dissipation concept model for turbulence–chemistry interaction,* Flow, Turbulence and Combustion **87**, 537 (2011).

[56] J. Aminian, C. Galletti, S. Shahhosseini, and L. Tognotti, *Key modeling issues in prediction of minor species in diluted-preheated combustion conditions,* Applied Thermal Engineering **31**, 3287 (2011).

[57] M. Evans, P. Medwell, and Z. Tian, *Modeling lifted jet flames in a heated coflow using an optimized eddy dissipation concept model,* Combustion Science and Technology **187**, 1093 (2015).

[58] A. Parente, M. R. Malik, F. Contino, A. Cuoci, and B. B. Dally, *Extension of the eddy dissipation concept for turbulence/chemistry interactions to mild combustion,* Fuel **163**, 98 (2016).

[59] K. K. Kuo and R. Acharya, *Fundamentals of turbulent and multi-phase combustion* (John Wiley & Sons, Inc., 2012).

[60] B. B. Dally, A. Karpetis, and R. Barlow, *Structure of turbulent non-premixed jet flames in a diluted hot coflow,* Proceedings of the Combustion Institute **29**, 1147 (2002).

[61] B. B. Dally, E. Riesmeier, and N. Peters, *Effect of fuel mixture on moderate and intense low oxygen dilution combustion,* Combustion and flame **137**, 418 (2004).

[62] P. R. Medwell, P. A. Kalt, and B. B. Dally, *Imaging of diluted turbulent ethylene flames stabilized on a jet in hot coflow (JHC) burner,* Combustion and Flame **152**, 100 (2008).

[63] P. R. Medwell and B. B. Dally, *Effect of fuel composition on jet flames in a heated and diluted oxidant stream,* Combustion and Flame **159**, 3138 (2012).

[64] P. R. Medwell and B. B. Dally, *Experimental observation of lifted flames in a heated and diluted coflow,* Energy & Fuels **26**, 5519 (2012).

[65] E. Oldenhof, M. Tummers, E. Van Veen, and D. Roekaerts, *Role of entrainment in the stabilisation of jet-in-hot-coflow flames,* Combustion and Flame **158**, 1553 (2011).

[66] E. Abtahizadeh, A. Sepman, F. Hernández-Pérez, J. van Oijen, A. Mokhov, P. de Goey, and H. Levinsky, *Numerical and experimental investigations on the influence of preheating and dilution on transition of laminar coflow diffusion flames to Mild combustion regime,* Combustion and Flame **160**, 2359 (2013).

[67] W. Yang and W. Blasiak, *Chemical flame length and volume in liquified propane gas combustion using high-temperature and low-oxygen-concentration oxidizer,* Energy & fuels **18**, 1329 (2004).

[68] P. R. Medwell, P. A. Kalt, and B. B. Dally, *Simultaneous imaging of OH, formaldehyde, and temperature of turbulent nonpremixed jet flames in a heated and diluted coflow,* Combustion and Flame **148**, 48 (2007).

[69] E. Oldenhof, M. Tummers, E. Van Veen, and D. Roekaerts, *Ignition kernel formation and lift-off behaviour of jet-in-hot-coflow flames,* Combustion and Flame **157**, 1167 (2010).

[70] E. Oldenhof, M. J. Tummers, E. H. Van Veen, and D. J. Roekaerts, *Transient response of the delft jet-in-hot coflow flames,* Combustion and flame **159**, 697 (2012).

[71] E. Oldenhof, M. J. Tummers, E. H. van Veen, and D. J. Roekaerts, *Conditional flow field statistics of jet-in-hot-coflow flames,* Combustion and Flame **160**, 1428 (2013).

[72] L. A. Mendez, M. Tummers, E. van Veen, and D. Roekaerts, *Effect of hydrogen addition on the structure of natural-gas jet-in-hot-coflow flames,* Proceedings of the Combustion Institute **35**, 3557 (2015).

[73] A. Sepman, A. Mokhov, and H. Levinsky, *Spatial structure and NO formation of a laminar methane–nitrogen jet in hot coflow under MILD conditions: A spontaneous Raman and LIF study,* Fuel **103**, 705 (2013).

[74] A. Sepman, E. Abtahizadeh, A. Mokhov, J. van Oijen, H. Levinsky, and P. de Goey, *Experimental and numerical studies of the effects of hydrogen addition on the structure of a laminar methane–nitrogen jet in hot coflow under MILD conditions,* international journal of hydrogen energy **38**, 13802 (2013).

[75] A. Sepman, S. Abtahizadeh, A. Mokhov, J. van Oijen, H. Levinsky, and L. de Goey, *Numerical and experimental studies of the NO formation in laminar coflow diffusion flames on their transition to MILD combustion regime,* Combustion and Flame **160**, 1364 (2013).

[76] R. Cabra, J.-Y. Chen, R. Dibble, A. Karpetis, and R. Barlow, *Lifted methane–air jet flames in a vitiated coflow,* Combustion and Flame **143**, 491 (2005).

[77] R. L. Gordon, A. R. Masri, and E. Mastorakos, *Simultaneous Rayleigh temperature, OH-and CH 2 O-LIF imaging of methane jets in a vitiated coflow,* Combustion and Flame **155**, 181 (2008).

[78] R. L. Gordon, A. R. Masri, S. B. Pope, and G. M. Goldin, *Transport budgets in turbulent lifted flames of methane autoigniting in a vitiated co-flow,* Combustion and Flame **151**, 495 (2007).

[79] M. Huang, W. Shao, Y. Xiong, Y. Liu, Z. Zhang, F. Lei, and Y. Xiao, *Effect of fuel injection velocity on mild combustion of syngas in axially-staged combustor,* Applied Thermal Engineering **66**, 485 (2014).

[80] B. Dally, D. Fletcher, and A. Masri, *Flow and mixing fields of turbulent bluff-body jets and flames,* Combustion Theory and Modelling **2**, 193 (1998).

[81] J. Aminian, C. Galletti, S. Shahhosseini, and L. Tognotti, *Numerical investigation of a mild combustion burner: analysis of mixing field, chemical kinetics and turbulence-chemistry interaction,* Flow, turbulence and combustion **88**, 597 (2012).

[82] A. Dongre, A. De, and R. Yadav, *Numerical investigation of MILD combustion using multi-environment Eulerian probability density function modeling,* International Journal of Spray and Combustion Dynamics **6**, 357 (2014).

[83] A. De and A. Dongre, *Assessment of Turbulence-Chemistry Interaction Models in MILD Combustion Regime,* Flow, Turbulence and Combustion **94**, 439 (2015).

[84] G. Sarras, Y. Mahmoudi, L. A. Mendez, E. van Veen, M. Tummers, and D. Roekaerts, *Modeling of Turbulent Natural Gas and Biogas Flames of the Delft Jet-in-Hot-Coflow Burner: Effects of Coflow Temperature, Fuel Temperature and Fuel Composition on the Flame Lift-Off Height,* Flow, Turbulence and Combustion **93**, 607 (2014).

[85] F. Christo and B. Dally, *Application of transport PDF approach for modelling MILD combustion,* in *15th Australasian Fluid Mechanics Conference* (2004).

[86] S. H. Kim, K. Y. Huh, and B. Dally, *Conditional moment closure modeling of turbulent nonpremixed combustion in diluted hot coflow,* Proceedings of the Combustion Institute **30**, 751 (2005).

[87] A. Frassoldati, P. Sharma, A. Cuoci, T. Faravelli, and E. Ranzi, *Kinetic and fluid dynamics modeling of methane/hydrogen jet flames in diluted coflow,* Applied Thermal Engineering **30**, 376 (2010).

[88] A. Mardani, S. Tabejamaat, and M. Ghamari, *Numerical study of influence of molecular diffusion in the Mild combustion regime,* Combustion Theory and Modelling **14**, 747 (2010).

[89] M. Ihme and Y. C. See, *LES flamelet modeling of a three-stream MILD combustor: Analysis of flame sensitivity to scalar inflow conditions,* Proceedings of the Combustion Institute **33**, 1309 (2011).

[90] A. Mardani, S. Tabejamaat, and M. B. Mohammadi, *Numerical study of the effect of turbulence on rate of reactions in the MILD combustion regime,* Combustion Theory and Modelling **15**, 753 (2011).

[91] M. Ihme, J. Zhang, G. He, and B. Dally, *Large-eddy simulation of a jet-in-hot-coflow burner operating in the oxygen-diluted combustion regime,* Flow, turbulence and combustion **89**, 449 (2012).

[92] Z. Mei, J. Mi, F. Wang, and C. Zheng, *Dimensions of CH_4-jet flame in hot O_2/CO_2 coflow,* Energy & Fuels **26**, 3257 (2012).

[93] J. Van Oijen, *Direct numerical simulation of autoigniting mixing layers in MILD combustion,* Proceedings of the Combustion Institute **34**, 1163 (2013).

[94] A. Mardani, S. Tabejamaat, and S. Hassanpour, *Numerical study of CO and CO_2 formation in CH_4/H_2 blended flame under MILD condition,* Combustion and flame **160**, 1636 (2013).

[95] F. Wang, P. Li, J. Zhang, Z. Mei, J. Mi, and J. Wang, *Routes of formation and destruction of nitrogen oxides in CH_4/H_2 jet flames in a hot coflow,* International Journal of Hydrogen Energy **40**, 6228 (2015).

[96] G. Sarras, M. Stoellinger, and D. Roekaerts, *Transported PDF simulations of the Delft-jet-in-hot-coflow burner based on 3D FGM tabulated chemistry,* Book of Extended Abstracts, Turbulence, Heat and Mass Transfer **7** (2012).

[97] R. M. Kulkarni and W. Polifke, *LES of Delft-Jet-In-Hot-Coflow (DJHC) with tabulated chemistry and stochastic fields combustion model,* Fuel processing technology **107**, 138 (2013).

[98] R. Bhaya, A. De, and R. Yadav, *Large Eddy Simulation of Mild Combustion Using PDF-Based Turbulence–Chemistry Interaction Models,* Combustion Science and Technology **186**, 1138 (2014).

[99] J. Labahn and C. Devaud, *Large eddy simulations (LES) including conditional source-term estimation (CSE) applied to two Delft-Jet-in-Hot-Coflow (DJHC) flames,* Combustion and Flame **164**, 68 (2016).

[100] E. Abtahizadeh, P. de Goey, and J. van Oijen, *LES of Delft Jet-in-Hot Coflow burner to investigate the effect of preferential diffusion on autoignition of CH_4/H_2 flames,* Fuel **191**, 36 (2017).

[101] E. Costa-Patry and L. Mydlarski, *Mixing of two thermal fields emitted from line sources in turbulent channel flow,* Journal of Fluid Mechanics **609**, 349 (2008).

[102] S. R. Shabanian, P. R. Medwell, M. Rahimi, A. Frassoldati, and A. Cuoci, *Kinetic and fluid dynamic modeling of ethylene jet flames in diluted and heated oxidant stream combustion conditions,* Applied Thermal Engineering **52**, 538 (2013).

[103] C. Galletti, A. Parente, and L. Tognotti, *Numerical and experimental investigation of a mild combustion burner,* Combustion and flame **151**, 649 (2007).

[104] H. Schütz, R. Lückerath, T. Kretschmer, B. Noll, and M. Aigner, *Analysis of the Pollutant Formation in the FLOX® Combustion,* Journal of Engineering for Gas Turbines and Power **130**, 011503 (2008).

[105] M. Mancini, R. Weber, and U. Bollettini, *Predicting NO_x emissions of a burner operated in flameless oxidation mode,* Proceedings of the Combustion Institute **29**, 1155 (2002).

[106] J. P. Kim, U. Schnell, and G. Scheffknecht, *Comparison of different global reaction mechanisms for mild combustion of natural gas,* Combustion Science and Technology **180**, 565 (2008).

[107] C. Duwig, B. Li, Z. Li, and M. Aldén, *High resolution imaging of flameless and distributed turbulent combustion,* Combustion and Flame **159**, 306 (2012).

[108] H. N. Najm, P. H. Paul, C. J. Mueller, and P. S. Wyckoff, *On the adequacy of certain experimental observables as measurements of flame burning rate,* Combustion and flame **113**, 312 (1998).

[109] W. L. Grosshandler, *RADCAL: A Narrow Band Model for Radiation,* NIST technical note 1402 (1994).

[110] A. Kazakov and M. Frenklach, *Reduced reaction sets based on GRI-Mech 1.2,* University of California at Berkeley, Berkeley, CA, (http://www.me.berkeley.edu/drm) (1994).

[111] G. P. Smith, D. M. Golden, M. Frenklach, N. W. Moriarty, B. Eiteneer, M. Goldenberg, C. T. Bowman, R. K. Hanson, S. Song, W. C. Gardiner Jr, *et al.*, *GRI-Mech 3.0,* University

of California at Berkeley, Berkeley, CA,(http://www.me.berkeley.edu/gri_mech)
51, 55 (1999).

[112] A. Parente, C. Galletti, and L. Tognotti, *Effect of the combustion model and kinetic mechanism on the MILD combustion in an industrial burner fed with hydrogen enriched fuels,* International journal of hydrogen energy **33**, 7553 (2008).

[113] R. Weber, J. P. Smart, and W. vd Kamp, *On the (mild) combustion of gaseous, liquid, and solid fuels in high temperature preheated air,* Proceedings of the Combustion Institute **30**, 2623 (2005).

[114] H. K. Kim, Y. Kim, S. M. Lee, and K. Y. Ahn, *No reduction in 0.03–0.2 mw oxy-fuel combustor using flue gas recirculation technology,* Proceedings of the Combustion Institute **31**, 3377 (2007).

[115] N. Krishnamurthy, P. Paul, and W. Blasiak, *Studies on low-intensity oxy-fuel burner,* Proceedings of the Combustion Institute **32**, 3139 (2009).

[116] Y. Neumeier, Y. Weksler, B. Zinn, J. Seitzman, J. Jagoda, and J. Kenny, *Ultra low emissions combustor with non-premixed reactants injection,* Paper No. AIAA **3775**, 2005 (2005).

[117] T. W. J. Peeters, *Numerical modeling of turbulent natural-gas diffusion flames,* Ph.D. thesis, TU Delft, Delft University of Technology (1995).

[118] M. Rehm, P. Seifert, and B. Meyer, *Theoretical and numerical investigation on the EDC-model for turbulence–chemistry interaction at gasification conditions,* Computers & Chemical Engineering **33**, 402 (2009).

[119] M. Ayoub, C. Rottier, S. Carpentier, C. Villermaux, A. Boukhalfa, and D. Honoré, *An experimental study of mild flameless combustion of methane/hydrogen mixtures,* international journal of hydrogen energy **37**, 6912 (2012).

[120] X. Gao, F. Duan, S. C. Lim, and M. S. Yip, *NO_x formation in hydrogen-methane turbulent diffusion flame under the moderate or intense low-oxygen dilution conditions,* Energy **59**, 559 (2013).

[121] P. Li, B. B. Dally, J. Mi, and F. Wang, *MILD oxy-combustion of gaseous fuels in a laboratory-scale furnace,* Combustion and Flame **160**, 933 (2013).

[122] G. Szegö, B. Dally, and G. Nathan, *Scaling of NO_x emissions from a laboratory-scale mild combustion furnace,* Combustion and Flame **154**, 281 (2008).

[123] J. Mi, P. Li, B. B. Dally, and R. A. Craig, *Importance of initial momentum rate and air-fuel premixing on moderate or intense low oxygen dilution (mild) combustion in a recuperative furnace,* Energy & Fuels **23**, 5349 (2009).

[124] A. Veríssimo, A. Rocha, and M. Costa, *Operational, combustion, and emission characteristics of a small-scale combustor,* Energy & Fuels **25**, 2469 (2011).